UNIVERSITY OF CALIFORNIA,
IRVINE

Interannual to Centennial-Scale Changes in Southeast Asian Hydroclimate during the Common Era

DISSERTATION

submitted in partial satisfaction of the requirements
for the degree of

DOCTOR OF PHILOSOPHY

in Earth System Science

by

Jessica Ka Main Wang

Dissertation Committee:
Dr. Kathleen Johnson, Chair
Dr. James Randerson
Dr. Jin-Yi Yu

2020

TABLE OF CONTENTS

LIST OF FIGURES

LIST OF TABLES

ACKNOWLEDGMENTS

My work was supported by the National Science Foundation Graduate Research Fellowship Program (DGE-1321846). Chapter 2 is a reproduction of an article as it appears in Earth and Planetary Science Letters 2019. Wang, J.K., K.R. Johnson, A. Borsato, D.J. Amaya, M.L. Griffiths, S. Frisia, G.M. Henderson A. Mason, 2019, Elsevier, 2019. The dissertation author is the primary investigator and author of this paper.

To say that I went out of my comfort zone during my tenure as a graduate student would be a complete understatement. My advisor, Dr. Kathleen Johnson, provided me the opportunities to grow not only as a researcher and scientist, but as a person. My experiences in Laos and Vietnam were absolutely incredible and I will never forget running through the forest in Vietnam covered in bug spray and duct tape to escape the leeches. I thank Kathleen for taking me on as a student, even though I did not know what a stalagmite was during prospective visit day, and for continuing to support me through all of my endeavors and research interests. I also thank my committee members, Dr. Jim Randerson and Dr. Jin-Yi Yu for providing me valuable insights, comments, and support that made all of this work possible. A special thank you to Jin-Yi who met with me weekly to review new results and provide new opportunities for me to learn more.

Thank you to my collaborators and colleagues that helped make the Laos record happen including, Michael Griffiths, Andrea Borsato, Gideon Henderson, Silvia Frisia, and Andrew Mason. It was a rollercoaster of emotions and adventures, but I am appreciative of the kindness, patience, and knowledge I received in helping me complete this work. I am grateful for the Lao and Vietnam government officials and departments for their assistance with our fieldwork and Dachung Zhang for all his help with the Kiel instrument. Thank you to past and present members of the Johnson lab: Hongying Yang, Christopher Wood, Kevin Wright, and Elizabeth Patterson. I will always be thankful for our paleo-coffee hours and our shared frustration with the lab instruments. Thank you to Lindsey Lewis for the laughs and jokes in the dirty lab.

Thank you to my 2014 cohort for all of the support during our first year and beyond. From all the coffee hours, lunches outside, to our intramural volleyball team, Anomalous SpikESS, I feel so grateful to have experienced graduate school with you all. A special thank you to Meg Fowler, Zack Labe, Emily Kane, Mindy Nicewonger, and Daniel Ruiz for supporting me through all these years. I would like to also thank Paige Austin and Sarah Aarons who were my first friends when I moved to Irvine and continued to be my close companions. I thank Scot Parker for taking me on a SCUBA student and letting me conquer my fears and anxieties while sending me encouraging daily memes for daily laughs. Thank you to Tina Geller who made the last few years of my PhD so incredibly fun and our underwater adventures that much more exciting. Additionally, I am grateful for the pedagogical fellowship program and Dr. Daniel Mann, who taught me so much. Thank you to Dr. Julie Ferguson and Dr. Elizabeth Crook for allowing me to serve as one of your teaching assistants and to develop my love for teaching.

I owe a great deal of thanks to my mentors during my undergraduate career that helped pave my path to graduate school: Dr. Mitch Lyle, Dr. Jennifer McKay, Dr. Steven Quiring, and Dr. Trent Ford. I am forever grateful for the opportunities to do research with such brilliant scientists, present at multiple conferences, publish papers, and to explore so many avenues of research. I

thank Angela Khong for being my partner-in-research who constantly encouraged me and supported me throughout my undergraduate and graduate careers.

I would like to give my sincere thanks to my family and friends who constantly gave me the support, love, and encouragement to complete my PhD. Thank you to my parents, Eddie and Sandy, who always pushed me to follow my dreams and to never give up, while providing a never-ending supply of food when I visited home. Thank you to my older brother, Anthony, for always being supportive and making me laugh. Thank you to Amanda Lyles, Mariel Fisher, Alicia Young, and Kate Durkin for their constant support even from many miles away. I am incredibly grateful for Morgan Gorris who gave me unparalleled support over the years. Lastly, I would like to thank my wonderful fiancé, Dillon Amaya, who encouraged and supported me from day 1 at Texas A&M. Thank you for convincing me to contact professors about doing research back in our sophomore year and for instilling “WHIENBOK” and confidence in me every day. Your dedication and passion for everything around you continuously inspires me. I am beyond grateful for your patience, kindness, love, and least importantly, your MATLAB scripts.

VITA

Jessica Ka Main Wang

EDUCATION

Doctor of Philosophy in Earth System Science 2020
University of California, Irvine

Master of Science in Earth System Science 2016
University of California, Irvine

Bachelor of Science in Meteorology 2014
Texas A&M University

HONORS AND AWARDS

NSF Graduate Research Fellowship Program (NSF GRFP)	2016-2020
Pedagogical Fellowship Award, UC Irvine	2019
NSF Graduate Research Internship Program (NSF GRIP) (*declined*)	2017-2018
UCI Associated Graduate Students (AGS) Travel Grant	2017
Goldschmidt Student Travel Grant	2017
UCI Data Science Initiative Fellowship	2015

PUBLICATIONS

Wang, J.K., K.R. Johnson, A. Borsato, D.J. Amaya, M.L. Griffiths, S. Frisia, G.M. Henderson A. Mason, 2019, Hydroclimatic Variability in Southeast Asia over the Last Two Millennia, *Earth and Planetary Science Letters*, **525**, 115737. doi: 10.1016/j.epsl.2019.115737

Quiring, S., T. Ford, **J.K. Wang,** A. Khong, E. Harris, T. Lindgren, D. Goldberg, and Z. Li, 2016: The North American Soil Moisture Database: Development and Applications. *Bulletin of the American Meteorological Society*, doi: 10.1175/BAMS-D-13-00263.1

Wang, J.K., T.W. Ford, and S.M. Quiring, 2015: Distinguishing between Unorganized and Organized Convection When Examining Land–Atmosphere Relationships. *Journal of Applied Meteorology and Climatology*, **54**, 2229-2243. doi: 10.1175/JAMC-D-15-0086.1

Khong, A., **J.K. Wang,** S.M. Quiring, and T.W. Ford 2015: Soil moisture variability in Iowa. *International Journal of Climatology*, **35**, 2837–2848. doi:10.1002/joc.4176

PRESENTATIONS

Wang, J.K., K. R. Johnson, M. Griffiths, D. Amaya, A. Borsato, G. M. Henderson, Silvia Frisia, Andrew Mason (2018) Hydroclimatic variability in Southeast Asian over the last two millennia. American Geophysical Union Annual Meeting *[Oral]*

Wang, J.K., K. R. Johnson, M. Griffiths, A. Borsato, G. M. Henderson, (2017) Reconstruction of Southeast Asian Hydroclimate over the last two millennia. Summer School on Speleothem Science, Burgos, Spain, *[Poster]*

Wang, J.K., K. R. Johnson, M. Griffiths, G. M. Henderson, (2017) Variations in Indo-China Hydroclimate over the Last Two Millennia. [Oral]. Goldschmidt 2017, Paris, France, *[Oral]*

Wang, J.K. (2017) Caves and Climate: Crawling back into the past. Association of Graduate Students Symposium, Irvine, CA, *[Oral]*

Wang, J.K., K. R. Johnson, M. Griffiths, G. Henderson (2016) Late Holocene Southeast Asian Monsoon variability inferred from speleothems. 10th Annual Graduate Climate Conference, Seattle, Washington, *[Poster]*

Wang, J.K. and K. Johnson (2015) Reconstructing Southeast Asian Monsoon variability using speleothems UCI Data Science Initiative Summer Research Symposium, *[Invited Oral and Poster]*.

Wang, J.K., S. M. Quiring, and T.W. Ford (2013) Does rain fall preferentially over dry soils (or wet soils)? AGU Fall Meeting 2013, San Francisco, California, *[Poster]*.

Wang, J.K. A. Khong, S. M. Quiring, and T. W. Ford (2013) Spatial Variability of In Situ Soil Moisture in Iowa. 93rd American Meteorological Society Annual Meeting, Austin, Texas, *[Poster]*.

RESEARCH EXPERIENCE

Graduate Student Researcher 2014-2020
Department of Earth System Science, *The University of California, Irvine*

Undergraduate Research Technician 2011-2014
Departments of Geography and Oceanography, *Texas A&M University*

NSF Research Experience for Undergraduates (REU) Fellow 2013
College of Earth, Ocean, and Atmosphere Sciences, *Oregon State University*

TEACHING EXPERIENCE

Teaching Associate, University of California, Irvine 2018
ESS: Introduction to Earth System Science, Class size: 74

Graduate Teaching Assistant, University of California, Irvine 2015-2016, 2019
ESS 17: Hurricanes, Tsunamis, and Other Catastrophes, Class size: 212, 396
ESS 7: Physical Geology, Class size: 133
ESS 21: On Thin Ice: Climate Change and the Cryosphere, Class size: 441

Graduate Teaching Assistant Summer 2014, 2016
American Indian Summer Institute in Earth System Science (AISESS)

PROFESSIONAL DEVELOPMENT

University of California, Irvine, Division of Teaching Excellence and Innovation

- Pedagogical Fellowship Program 2018-2019
- Pedagogical Liaisons Program 2018
- Certificate in Teaching Excellence 2018
- Course Design Certificate 2018

Center for the Integration of Research, Teaching, and Learning (CIRTL) 2018

- Associate Level Certificate

SERVICE AND OUTREACH

Climate Literacy, Empowerment And iNquiry (CLEAN) Education 2014-2020
University of California, Irvine

Student Chapter of the American Meteorological Society at UCI 2017-2020
University of California, Irvine
Co-Founder and Vice-President (2018-2019)

Teaching Assistant Professional Development Program 2019
University of California, Irvine

Inclusive Instruction Working Group, University of California, Irvine 2019

Mentor, University of California, Irvine 2018-2019
Physical Sciences Undergraduate Mentorship Program

Event Supervisor, Orange County Regional Science Olympiad 2017-2019
Climate Science-Meteorology exam writer and proctor

ABSTRACT OF THE DISSERTATION

Interannual to Centennial-Scale Changes in Southeast Asian Hydroclimate during the Common Era

By

Jessica Ka Main Wang

Doctor of Philosophy in Earth System Science

University of California, Irvine, 2020

Dr. Kathleen Johnson, Chair

The Asian Monsoon system impacts more than two-thirds of the world's population each year by supplying the necessary water resources to sustain agriculture, the economy, and the socioeconomic welfare for billions of people. In recent decades, changes in the strength and spatial extent of the monsoon have led to significant drought and flooding events. Currently, climate models do not agree on future changes in monsoonal rainfall. In order to improve projections of changes in the Asian Monsoon, it is important to investigate how the monsoon has varied in the past. Climate proxy records obtained through archives (such as cave deposits) provide evidence for changes in past climate on a range of timescales.

My dissertation focuses on the Southeast Asian region, where few paleoclimate records that span the last 2,000 years currently exist. I present the first, high-resolution speleothem record from northern Laos. The carbon stable isotope ($\delta_{13}C$) record reveals decades-long megadroughts, consistent with previous findings from regional tree ring records, whereas the oxygen stable isotope ($\delta_{18}O$) record, interpreted as changes in monsoon intensity, exhibits a relationship with solar variability. I identify that multidecadal to centennial-scale shifts in monsoon intensity are linked with solar-forced changes in tropical Atlantic sea surface

temperatures. I also examine the modern interannual variability of precipitation across East China and Southeast Asia over the last 30 years. I show that spatial tripole and dipole rainfall patterns are linked with the El Niño Southern Oscillation and North Atlantic Oscillation, respectfully. Finally, I evaluate how different water pathways and in-cave properties may influence speleothem $\delta_{18}O$ values at our cave site using an integrated speleothem forward model and cave monitoring data. I conclude that combined effects of karst hydrology and in-cave processes contribute to speleothem $\delta_{18}O$ variability.

The collective results of my dissertation help us better understand changes in Southeast Asian hydroclimate on a variety of spatial and time scales. This research builds upon the limited number of paleoclimate records from Laos and the surrounding countries, while contributing to modern rainfall analyses and proxy system modeling studies to better interpret paleoclimate records and improve projections of monsoon rainfall.

Chapter 1

1 Introduction

1.1. The Asian Monsoon System

Monsoons are canonically characterized by a pronounced annual reversal in large-scale atmospheric circulation and low-level winds, which can result in distinct regional precipitation patterns (Webster et al. 1998; Wang et al. 2003; Cheng et al. 2012a). The immense Asian summer monsoon (AM) system plays an important role in the transfer of energy and moisture from the equator to higher latitudes (Webster et al. 1998; Wang et al. 2001a). Increased springtime heating over the Asian continent enhances the land-ocean thermal contrast since the land surface heats faster than the neighboring ocean regions. These temperature variations between the land and ocean initiate the AM in early May, which triggers strong meridional transport of heat and moisture from northern Australia to India and China (Cheng et al. 2012a). The extensive spatial domain of the AM impacts the livelihoods of nearly two-thirds of the global population by providing the necessary water resources during the boreal summer monsoon season (May-September) (Webster et al. 1998). The AM system includes several regional monsoon systems (e.g., Indian, East Asian, and Southeast Asian monsoons) that are distinguished by varying seasonal shifts in surface wind patterns and precipitation distributions (Wang et al. 2005a; Conroy and Overpeck 2011) (Figure 1.1). Varying onset and decay dates, strengths of atmospheric circulation, and spatial precipitation patterns characterize these regional monsoon systems on intraseasonal to interdecadal timescales (Wang et al. 2003; Zhou et al. 2009).

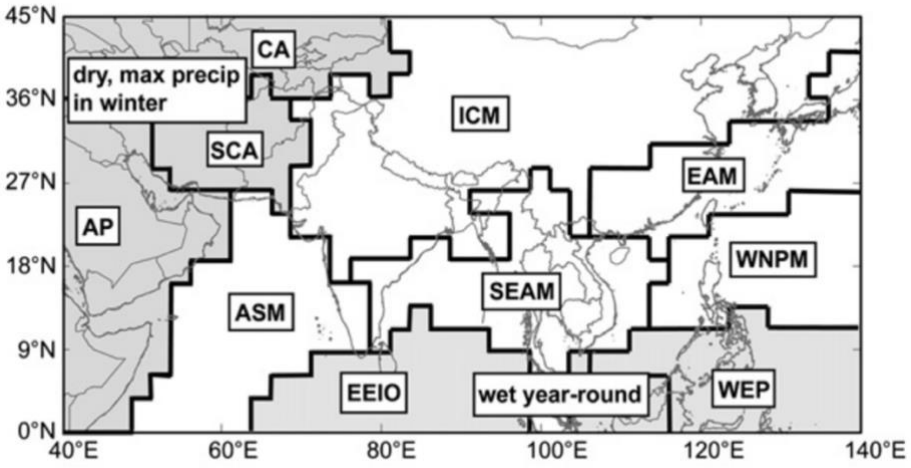

Figure 1.1 The Asian monsoon region and regional monsoon systems as defined using an empirical orthogonal function (EOF)-based regionalization of gridded precipitation values. SEAM refers to the Southeast Asian Monsoon. ICM is the Indian Continent Monsoon and the EAM is the East Asian Monsoon. Modified figure from Conroy and Overpeck (2011).

1.2. Future Monsoon Precipitation

While future global precipitation is expected to generally increase with increasing temperatures in response to rising anthropogenic CO_2 emissions (IPCC 2013), projected regional precipitation patterns in the tropics remain unresolved due to the large inter-model spread (Christensen et al. 2013). The broad spatial pattern of total precipitation changes follows a "wet-gets-wetter" pattern (Held and Soden 2006) or, over the oceans, the warmer-gets-wetter pattern (Xie et al. 2010; Chadwick et al. 2013). Increased specific humidity in a warmer atmosphere can cause more moisture convergence in climatologically wet areas and more moisture divergence over climatologically dry areas, thus producing a "wet-gets-wetter" pattern (Held and Soden 2006). Anthropogenic-influenced factors, such as greenhouse gases, aerosols, land use, and land cover change, are expected to impact the AM system in varying capacities (Kitoh 2017). For example, monsoon circulation is expected to weaken over the tropics, but an increase in aerosols

may cause more rainfall and enhance the amount of available atmospheric moisture (Christensen et al. 2013).

Lower-tropospheric winds are also projected to weaken, which may cause a decrease in the magnitude of convergence over monsoonal rain areas through the 21st century (IPCC 2007). Despite a projected weakening in atmospheric circulation (i.e., a dynamic component), increases in air temperature are expected to cause the land surface to warm faster than the ocean, exacerbating the land-ocean temperature contrasts. The atmosphere's moisture content (i.e., a thermodynamic component) is expected to increase, which can lead to increased moisture flux convergence, local evaporation, and water vapor transport from the ocean to the land due to warmer surface temperatures (Endo and Kitoh 2014). As a result, there is emerging consensus that a thermodynamic component will dominate over any such weakening of monsoon circulation, resulting in more monsoonal precipitation (Ueda et al. 2006).

In addition to changes in annual rainfall patterns, extreme precipitation events over wet tropical regions will likely be more intense and more frequent by the end of the century (IPCC 2013). Mean temperatures have already increased by 0.1°C -0.3°C per decade from 1950 to 2000 over Southeast Asia (IPCC 2013), and the likelihood of record-breaking extreme temperatures continues to increase (Thirumalai et al. 2017). Continued warming in combination with more extreme distributions of rainfall are expected to increase the chance of heat waves, droughts and floods. Some of the societal impacts of these climate changes over Southeast Asia already include declines of crop yield in Thailand, Vietnam, and Indonesia, massive flooding in Vietnam, Indonesia, and Laos, landslides in the Philippines and droughts in many other parts of Southeast Asia (Asian Development Bank. 2009).

Most CMIP5 historical simulations are unable to reproduce observed precipitation patterns (Raghavan et al. 2018). Improvements in global climate models will rely on a robust understanding of the internal climate system, which controls the mechanisms altering the spatiotemporal evolution of monsoon variability and tropical precipitation patterns. In addition, external forcings (e.g., solar variability and volcanic events) are also important for constraining climate model projections (Clemens et al. 1991; Wang et al. 2008b). Altogether, an improved understanding of monsoon dynamics and regional hydroclimate can help improve projections of AM variability and inform adaptation measures for an anthropogenic greenhouse gas-induced warming planet (Solomon et al. 2007).

While instrumental data and historical records provide insights on the last ~150 years of climate across the broader AM region, these data are particularly sparse over mainland Southeast Asia (MSEA) and do not span timescales that are crucial to analyze multidecadal to orbital-scale changes in past climate. In order to achieve a more comprehensive understanding of the annual to multi-centennial shifts in hydroclimate across the AM region, it is important to have a dense network of high-resolution, precisely-dated climate records that spans at least the last two millennia.

1.3. Paleoclimate Archives and Proxy Records

1.3.1 Orbital-Millennial Scale Variability

Paleoclimate proxy records obtained from climate archives, such as speleothems (cave deposits), ice cores, ocean and lake sediment cores, and tree rings, are valuable in evaluating past climate conditions, in response to natural climate variability and external forcings, on a variety of timescales. For instance, speleothems records from the East Asian Summer Monsoon (EASM)

and Indian Summer Monson (ISM) regions have revealed a close relationship between changes in the AM and shifts in Northern Hemisphere summer insolation on orbital timescales (Wang et al. 2001b, 2008b; Kathayat et al. 2016; Cheng et al. 2016). On millennial timescales, a close correspondence between AM variability and climate in the North Atlantic has been observed among paleoclimate records (Dansgaard et al. 1993; Peterson et al. 2000; Liu et al. 2015). Weak EASM events have been linked to North Atlantic ice-rafting events (Wang et al. 2001b, 2008b; Cheng et al. 2009, 2012b), which likely led to a slowdown in the Atlantic Meridional Overturning Circulation (AMOC) and a reorganization of atmospheric and oceanic circulation patterns (Wang et al. 2001b; Cheng et al. 2016). Paleoclimate records from ISM regions also exhibit similar millennial-scale variability driven by North Atlantic climate (Wang et al. 2001b; Cai et al. 2015), though Antarctic glacial and sea-ice retreat have been hypothesized to also influence the ISM region (Cheng et al. 2012a, 2016). Variations in precession and the strength of the AMOC likely influenced meridional temperature gradients, the position of the Intertropical Convergence Zone (ITCZ) (Mohtadi et al. 2016), and subsequently the strength of the AM (Wang et al. 2008b; Cheng et al. 2009). However, there are still uncertainties on the relationship between orbital to millennial-scale forcings and AM variability among speleothem AM records and other proxy records of precipitation and wind strength (Mohtadi et al. 2016; Beck et al. 2018) that call for more paleoclimate records and additional work.

1.3.2 Decadal to Centennial-Scale Variability

Changes in monsoonal precipitation on decadal to centennial-scales among paleoclimate records are subjected to additional debate due to the variable spatiotemporal distribution of monsoon rainfall. Over the last decade, high-resolution proxy records of AM strength have

highlighted significant decadal to centennial-scale hydrologic variability during the Common Era (Zhao et al. 2015, 2016; Yan et al. 2015; Griffiths et al. 2016). However, the consensus of the precise mechanisms or the spatial extent of hydroclimate changes among these records remain unresolved due to the varying climate signals recorded in these records.

The Medieval Climate Anomaly (MCA, 950-1250 CE) and the Little Ice Age (LIA, 1400-1850 CE) (Mann et al. 2009) manifest as periods of anomalous hydrologic conditions in paleoclimate records. During the MCA, paleoclimate records suggest increased precipitation patterns in northern China (Zhang et al. 2008) and decreased precipitation in southern China (Wang et al. 2008b; Hu et al. 2008) and the Indo-Pacific region (Oppo et al. 2009; Conroy et al. 2010), supporting the hypothesis of a northward shift in the ITCZ. However, lake records from the South China Sea (Yan et al. 2011) and other proxy records from the central and eastern tropical Pacific propose that the influence of the El Niño-Southern Oscillation (ENSO) and associated zonal shifts of deep convection played a more important role than ITCZ shifts during this time (Moy et al. 2002; Conroy et al. 2008; Sachs et al. 2009; Yan et al. 2011; Konecky et al. 2013). In addition, tree ring records from Thailand (Buckley et al. 2007b), Vietnam (Sano et al. 2012), and Laos (Buckley et al. 2007a; Xu et al. 2011) have attributed interannual-decadal hydrologic changes to ENSO variability as opposed to ITCZ shifts.

Within the discussions of ITCZ shifts versus ENSO, there are additional debates among studies on the phase of ENSO during these anomalous climate periods. For example, the in-phase rainfall relationships among several tropical Pacific records suggest more El Niño-like condition during the MCA (Tan et al. 2008; Yan et al. 2011). However, the opposite mechanism suggesting more La Niña-like conditions during the MCA, but El Niño-like conditions during LIA, has also been proposed by other studies (Cobb et al. 2003). The phase status of ENSO

during the MCA and LIA continues to be debated and requires further studies (Chen et al. 2016). In light of this previous work, however, it is likely that both ENSO and ITCZ shifts influenced interannual to centennial-scale hydrologic variability throughout the Common Era, including during the MCA and LIA (Tan et al. 2019). A synthesis of paleo-hydrologic records from the western tropical Pacific highlighted the possible combined effects and suggested that the meridional extent of the seasonal ITCZ migration during the LIA possibly contracted at the same time that the Pacific Walker circulation strengthened (Yan et al. 2015; Griffiths et al. 2016). Rather than a uniform southward migration of the ITCZ during the LIA, the latitudinal range of the ITCZ contracted equatorward (Yan et al. 2015; Griffiths et al. 2016), which was hypothesized to be in response to solar irradiance (Bard et al. 2000).

Presently, these hypotheses remain not well-established for Mainland Southeast Asia (MSEA), since many of the previously-published records from MSEA are either short in duration (i.e., only span the last few hundred years) or demonstrate low temporal resolution. To assess future changes in AM variability, specifically over MSEA, it is therefore important to have high-resolution and absolute-dated climate records. By utilizing terrestrial climate archives, such as speleothems, it is possible to better understand past changes in monsoon rainfall and local hydroclimate on interannual to centennial timescales.

1.4. Using Speleothems for High-Resolution Climate Reconstructions

1.4.1. Speleothem Formation

Speleothems are beneficial climate archives for terrestrial reconstructions, particularly in the Northern Hemisphere mid-latitudes (Wang et al. 2008b). Speleothems can be absolute-dated with U-Th methods and exhibit continuous or semi-continuous deposition, which may preserve

orbital to annual-occurring climate signals, making these ideal climate archives for paleoclimate reconstructions.

Speleothems are mostly composed of calcium carbonate ($CaCO_3$), either as calcite or aragonite, and form in limestone caves. They grow layer-by-layer through carbon dioxide (CO_2) degassing from cave drip water over tens of thousands of years. The chemical reactions for the deposition of speleothems are below:

$$CO_2 + H_2O \rightarrow H_2CO_3 \quad (1)$$

$$H_2CO_3 + CaCO_3 \rightarrow Ca^{2+} + 2HCO3^- \quad (2)$$

$$Ca^{2+} + 2HCO_3^- \rightarrow CO_2 + CaCO_3 + H_2O \quad (3)$$

Groundwater (generally sourced from precipitation that falls above the cave) reacts with CO_2 generally sourced from soil and root respiration and decomposition of soil organic matter to form carbonic acid (H_2CO_3) (equation 1), which dissolves the limestone cave bedrock (equation 2). CO_2 is released into the cave air (through CO_2 degassing) when the drip water enters the cave, and bicarbonate is supersaturated causing $CaCO_3$ to precipitate and form speleothems (Fairchild et al. 2006a) (equation 3) (Figure 1.2).

During these processes, geochemical signals (e.g., oxygen and carbon stable isotopes) that are typically sourced from the atmosphere, soil zone, or epikarst (sub-soil zone of fractured and highly weathered bedrock) are incorporated within the calcite layers of speleothems. Variations in oxygen isotope ratios of calcite precipitated under isotopic equilibrium conditions generally reflect the oxygen isotope signal of precipitation above the cave and the cave temperature. Rainfall oxygen isotope ratios may be influenced be a suite of factors including

precipitation amount (Dansgaard 1964), moisture source and transport (Pausata et al. 2011), and large-scale atmospheric monsoonal circulation (Yang et al. 2016). Conversely, the carbon isotope variations in speleothem calcite can reflect changes in the overlying vegetation, soil processes, and in- and above-cave processes (Baker et al. 1997; Genty et al. 2001; Frisia et al. 2011).

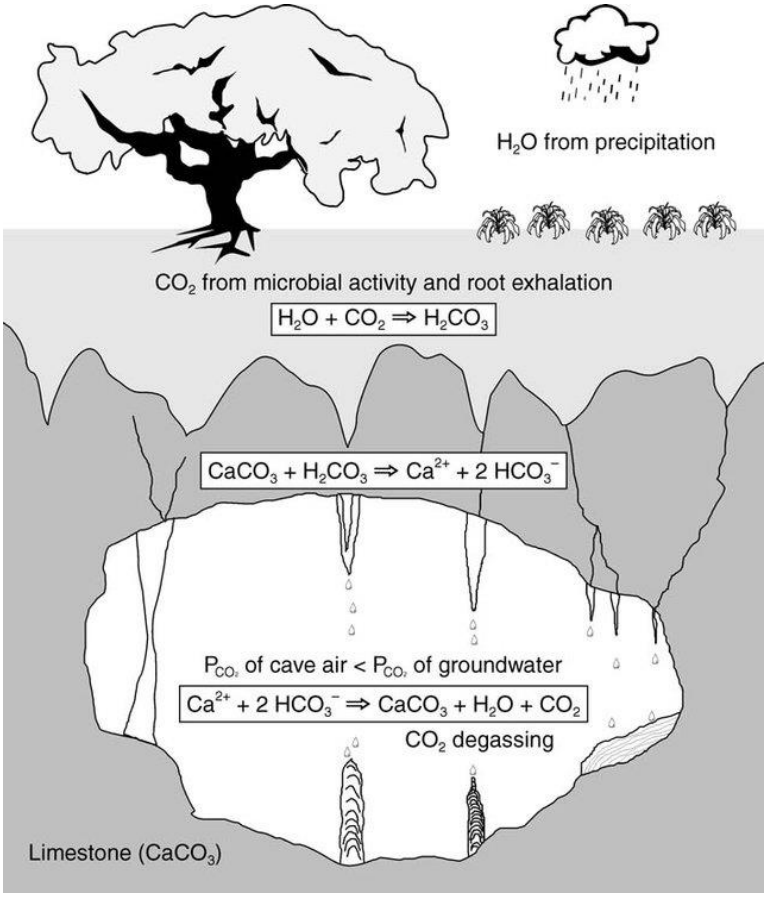

Figure 1.2. Schematic representation of speleothem formation in a karstic environment. Percolating water mixes with high levels of partial pressures (*p*CO2) in the soil due to respiration and decomposition of organic matter. Carbonate minerals are dissolved when in contact with the percolating solution. When the drip water solution enters the cave, which has a lower *p*CO2 than the original soil, CO_2 is degassed and $CaCO_3$ is precipitated (Fairchild and Baker 2012). Figure is from Fleitmann et al. (2004).

1.4.2. The Delta (δ) Notation

Stable oxygen and carbon isotope ratios are expressed in delta notation (δ) and in units of per mill (‰) relative to international reference standards. The conventional and most commonly used standard are Vienna Standard Mean Ocean Water; V-SMOW for water samples and Vienna Pee Dee Belemnite (V-PDB) for carbonates. The delta notation is represented by:

$$\delta^{18}\mathrm{O} = \frac{R_{\text{sample}} - R_{\text{standard}}}{R_{\text{standard}}} \times 1000‰ \quad (4)$$

Where $R = \frac{rare\ isotope}{common\ isotope}$

e.g., R = $_{18}$O/$_{16}$O

1.4.3. Speleothem Chronology

Speleothems are advantageous for paleoclimate reconstructions, because they can be absolute-dated through the uranium-thorium (U-Th) dating method. U-Th dating is based on the radioactive decay of $_{234}$U to $_{230}$Th. Uranium, which is highly abundant and sourced from the soil and bedrock, is highly soluble and transported in solution (e.g., drip water) and co-precipitated during speleothem deposition (Fairchild and Baker 2012). Thorium, however, is insoluble under oxidizing conditions, and therefore does not leach into the bedrock, but is instead adsorbed onto clay minerals (Richards and Dorale 2003). Speleothem calcite, therefore, does not typically contain initial Th and can be radiometrically-dated by measuring the accumulation of radiogenic $_{230}$Th. However, speleothems often contain trace amounts (ppt to ppb level) of initial ("detrital" or non-radiogenic) thorium from impurities, such as clay minerals, which can lead to artificially old U-Th ages (Spötl and Boch 2012). To correct for this initial $_{230}$Th input, the amount of $_{232}$Th

is measured in the sample and then used to estimate an initial $^{230}Th/^{232}Th$ ratio (Fairchild and Baker 2012). The initial Th correction can often be a challenge for very young speleothem with low uranium concentrations and subsequently low ^{230}Th concentrations. In this dissertation, raw ages were corrected for initial Th using an initial $^{230}Th/^{232}Th$ atomic ratio of $4.4 \pm 2.2 \times 10^{-6}$, but values may vary with the host rock and soil characteristics with a range of activity ratios from ~0.2 (Drysdale et al. 2006) to ~18 (Beck et al. 2001). This initial Th correction yielded age differences ranging of one year to 20 years with an average of eight years.

Robust age models are fundamental for paleoclimate reconstructions and speleothem proxy records must be associated with a time scale in order for interpretations of the data can be made (Breitenbach et al. 2012). A variety of different algorithms and programs have been developed as to establish the depth-age relationship for each proxy data point. For example, a Bayesian radiocarbon chronology model called Bchron produces an ensemble of plausible age-depth chronologies that is independent of the source of tie-point chronology and can be calibrated with additional radiocarbon (^{14}C) or U-Th dates (Haslett and Parnell 2008). Another algorithm, StalAge, uses U-Th ages and the corresponding age uncertainties alongside stratigraphic information to further constrain and improve the age model (Scholz and Hoffmann 2011). StalAge eliminates major outliers during the screening process of age data and conducts calculations at a 95% confidence level (Scholz and Hoffmann 2011).

In addition to these algorithms, it is possible to construct a chronology based on counting of annual speleothem laminae in conjunction with U-Th ages. However, speleothem layers may not always be deposited annually, and these bands may be under- or over-counted, leading to greater errors and uncertainties (Shen et al. 2013). A depth-age modeling program, Constructing Proxy Records from Age Models (COPRA), integrates both U-Th ages and sections of laminae

counting to increase the robustness of an age model (Breitenbach et al. 2012). While U-Th ages and supplemented laminae counting may improve the age model, there can be the added challenge in determining the youngest age of the speleothem (i.e., the top age) if the speleothem sample was not actively growing at the time of collection. U-Th-based chronology associated with errors will essentially be floating in time space given that the length of the record is fixed but can be moved along an age scale. To combat these challenges, methods have been developed to determine the top age using a variety of methods including linear interpolation, least-squares polynomial fit, and linear regression (Domínguez-Villar et al. 2012).

1.4.4. Controls of Speleothem $\delta^{18}O$

Over the last few decades, many studies have characterized AM variability and the underlying mechanisms across a variety of timescales using speleothems (Wang et al. 2001b, 2005b, 2008b; Yuan 2004; Zhang et al. 2008; Cheng et al. 2009; Cai et al. 2015). Most notably, the longest speleothem-based record that covers the full U-Th dating range provides a 640,000-year record of EASM variability on orbital to millennial timescales (Cheng et al. 2016). The most common climate proxy extracted from calcite speleothems, specifically stalagmites, is the oxygen isotopic composition, which is expressed by the ratio of $^{18}O/^{16}O$ ($\delta^{18}O$). Speleothems that form under conditions of isotopic equilibrium implies isotopic equilibrium between $CaCO_3$, $HCO3^-$, and H_2O (Hendy 1971). Under isotopic equilibrium conditions, variations in $\delta^{18}O$ of speleothem calcite are dependent on the cave drip water $\delta^{18}O$ and the cave temperature during speleothem precipitation (Wackerbarth et al. 2010). However, variations in drip water $\delta^{18}O$ are usually larger in magnitude compared to that of temperature-dependent fractionation between water and calcite (~-0.23‰/°C) (Kim and O'Neil 1997) and therefore typically dominate the

speleothem $\delta_{18}O$ signal (Lachniet 2009). While this may vary from site to site due to differences in karst hydrology and water pathways, it is commonly assumed that the local rainfall above the cave directly travels through the karst system above the cave and the precipitation $\delta_{18}O$ signal is preserved in the drip water $\delta_{18}O$ that feeds the stalagmite (Hendy and Wilson 1968; Fleitmann et al. 2003).

In the AM region, the precise controls on precipitation $\delta_{18}O$, and subsequently stalagmite $\delta_{18}O$, have been largely discussed and debated over the last couple of decades (Zhang et al. 2019). Chinese stalagmite $\delta_{18}O$ records were originally interpreted to reflect changes in 'monsoon intensity', which referred to the ratio of summer to winter precipitation (i.e., precipitation seasonality) (Cheng et al. 2009). However, different interpretations and language use of the phrase 'monsoon intensity' has resulted in ambiguity and misrepresentations within the paleoclimate community (Dayem et al. 2010). Interpretations of 'monsoon intensity' has mistakenly referred to changes in the intensity of summer rainfall (Cheng et al. 2009; Dayem et al. 2010), implying that more negative $\delta_{18}O$ values denotes more intense summer rainfall. Similarly, some studies have argued that Chinese speleothem $\delta_{18}O$ reflects changes in the local "amount effect", which describes the inverse relationship between local rainfall amount and speleothem $\delta_{18}O$ values (Wang et al. 2001b; Hu et al. 2008; Griffiths et al. 2009). However, a number of other studies from the EASM region have disputed the "amount effect" interpretation. Instead, these studies argue that speleothem $\delta_{18}O$ variations reflect changes in large-scale monsoon circulation patterns, that include changes in precipitation seasonality (Wang et al. 2001a), atmospheric circulation (Tan 2014; Chiang et al. 2015; Zhang et al. 2018a), moisture source region (Maher and Thompson 2012) or the degree of upstream rainout during transport (Pausata et al. 2011). Stalagmite $\delta_{18}O$ interpretations have also varied between ISM and EASM

records, such that, ISM records have indeed interpreted changes in stalagmite $\delta^{18}O$ to local or regional precipitation amount (Berkelhammer et al. 2010; Sinha et al. 2011a). Atmospheric moisture sourced from the Indian Ocean and advected to Chinese cave sites and/or distinctive moisture pathways to East China may also appear as discrepancies among different cave records from the AM region and result in different interpretations of stalagmite $\delta^{18}O$ (Cai et al. 2015).

Given these various hypotheses on the controlling factors of speleothem $\delta^{18}O$, rigorous testing using isotope-enabled climate models have been recently conducted (Comas-Bru et al. 2019; Hu et al. 2019). In support of findings from previous studies, the isotope-enabled climate runs show that precipitation $\delta^{18}O$ variability is associated with large-scale changes in circulation and moisture source but does not necessarily imply fluctuations in the amount of rainfall at the cave sites (Hu et al. 2019). Thus, interpretations of speleothem $\delta^{18}O$ variations are best supported as changes in regional-scale atmospheric circulation and associated changes in moisture source of air masses reaching the monsoon domain (Lachniet 2020).

In this dissertation, monsoon intensity is defined as regional-scale changes in rainfall upstream of our study site (referred to as upstream rainout), specifically over the Bay of Bengal and Indian Ocean, which is most closely related to the strength of the ISM. It is important to note that I made no assumptions about whether monsoon intensity and local rainfall amount should covary.

1.4.5. Controls of Speleothem $\delta^{13}C$

Another useful stalagmite proxy suitable for identifying changes in local hydrology is the carbon isotopic composition ($^{13}C/^{12}C$; $\delta^{13}C$). Interpretations of stalagmite $\delta^{13}C$ are complex, due to the various carbon sources in speleothem calcite, such as the local soil and epikarst zones

(Fairchild et al. 2006a), and the climatic and non-climatic factors that may influence stalagmite $\delta^{13}C$. Variations in stalagmite $\delta^{13}C$ are dependent on the $\delta^{13}C$ of the dissolved inorganic carbon (DIC) of the parent solution, which is canonically influenced by the $\delta^{13}C$ of soil CO_2. Shifts in the $\delta^{13}C$ of soil CO_2 can vary according to (1) the ratio of C_3 plants ($\delta^{13}C$ ~ -25‰) to C_4 plants ($\delta^{13}C$ ~ -13‰) in the overlying vegetation cover (Dorale et al. 1998; Genty et al. 2001), (2) contributions from atmospheric CO_2 (Genty et al. 2003), and/or (3) changes in biogenic activity. For example, low respiration rates by microbial organic matter oxidation and root respiration during drought conditions may shift $\delta^{13}C$ to more positive values (i.e., closer to atmospheric CO_2 values (~ -8‰) than to soil CO_2 values (~ -25‰) (Genty et al. 2001). Conversely, increased soil respiration during wet periods cab result in higher soil pCO_2 and more negative $\delta^{13}C$ values of soil CO_2 (gas), dissolved inorganic carbon (water) and eventually stalagmite $\delta^{13}C$ (Oster et al. 2010).

Further changes in $\delta^{13}C$ may occur depending on (1) the degree of host rock carbon contribution due to changes in open versus closed system dissolution conditions (Hendy, 1971; Oster et al. 2010), (2) CO_2 degassing and associated prior calcite precipitation (PCP) within the epikarst and cave (Johnson et al. 2006; Mühlinghaus et al. 2007; Frisia et al. 2011), and/or (3) kinetic fractionation (Baker et al. 1997). PCP is thought to increase during drier periods when dewatering of the karst system enhances $^{12}CO_2$ degassing from the infiltrating water, leading to more positive values of stalagmite $\delta^{13}C$ (Fairchild et al. 2000, 2006a; Johnson et al. 2006; Oster et al. 2010; Treble et al. 2015). Slower drip rates during dry periods contribute to longer residence times in the epikarst and more exposure to air space in the fractures and cavities above the cave, enhanced CO_2 degassing, and increased likelihoods of PCP and more positive stalagmite $\delta^{13}C$ values (Mühlinghaus et al. 2007; Frisia et al. 2011). Lastly, kinetic fractionation

during CO_2 degassing may occur when the rate of CO_2 loss from solution is too rapid to maintain equilibrium between aqueous carbon dioxide and bicarbonate ions, which can lead to higher $\delta_{13}C$ values (Hendy 1971; Frisia et al. 2011).

Despite these various processes, speleothem $\delta_{13}C$ shifts are found to be sensitive to factors that all relate to climate: changes in vegetation cover, the degree of microbial activity in the soil, and the effective water balance in the karst system (Genty et al. 2003; Griffiths et al. 2010, 2012; Oster et al. 2010). These processes typically respond in the same direction to hydrological changes, regardless of the various mechanisms responsible for changes in stalagmite $\delta_{13}C$ (Wong and Breecker 2015). As such, more positive $\delta_{13}C$ values are typically indicative of drier conditions at a study site and vice versa (Wong and Breecker 2015).

1.5. Proxy System Modeling

While stalagmite proxy records have provided extensive information on past AM variability and tropical hydroclimate, the climate signals embedded within the calcite layers of stalagmites are subjected to filtering by environmental conditions in complex ways. For example, the karst hydrology of a cave (e.g., effects of transport and mixing of drip water $\delta_{18}O$ through the epikarst) have the potential to filter out the seasonal to interannual climate signals present in precipitation $\delta_{18}O$ (Baker and Bradley 2010; Dee et al. 2016). An approach to improve our understanding of these processes is a forward-modeling method known as Proxy System Modeling (Evans et al., 2013). Traditional calibration techniques using instrumental records and reanalysis data are useful to clarify interpretations of speleothem $\delta_{18}O$ data. Even so, proxy system models (PSMs) can further quantify the relationship between the $\delta_{18}O$ signals recorded in stalagmites and the environmental inputs (e.g., precipitation, temperature) that may have

influenced the signal (Evans et al. 2013; Dee et al. 2015). This method can improve our ability to distinguish the impact of climate variability versus hydrological processes on speleothem $\delta_{18}O$ by quantifying uncertainties and distinguishing the signals between the proxy data and the modeled data. In addition to simulating the propagation of uncertainties, PSMs are designed to improve interpretations of proxy records. The physical processes within the karst system that ultimately affect speleothem $\delta_{18}O$ are distinguished in several stalagmite-based proxy models (Truebe et al. 2010; Baker and Bradley 2010; Wackerbarth et al. 2010).

1.5.1. Karst Hydrology and In-Cave Processes

Several studies have highlighted this increased ability to distinguish the impact of climate variability versus (non-climatic) hydrological processes on stalagmite $\delta_{18}O$ using detailed observations of precipitation, drip water, and modern stalagmite $\delta_{18}O$ values (Baker and Bradley 2010; Moerman et al. 2014). Since the climate signal to noise ratio (signal:noise) over the last millennium is much lower compared to that of millennial to orbital timescales, it is particularly important to consider the impact of transport and mixing on shorter timescales that may cause some degree of hydrologic "smoothing" that takes place as the rainfall infiltrates down through the epikarst (Bradley et al. 2010; Dee et al. 2017; PAGES Hyro2k Consortium 2017).

Early developments of karst (topography formed by dissolution of limestone) forward models began with Fairchild et al. (2006b), who utilized a linear reservoir approach for a two-layer model. This simple model represented the possible flow pathways and distinguished the geochemical variability in the soil and karst in southwestern England. Baker et al. (2010) utilized a single reservoir model for an Ethiopian speleothem that grew from drip water that traveled through two discrete flow paths (e.g., (1) diffuse seepage through the karst matrix and (2)

fracture-fed flow). Several modifications to improve the complexity of this simple model included incorporating a parameter for higher drip water $\delta_{18}O$ values due to evaporation at the soil surface, a parameter for diffuse and matrix flow into the water stores, and a parameter for speleothem precipitation under non-equilibrium processes (Baker et al. 2010).

While these previously-published models have successfully distinguished various karst processes, other PSMs are focused on the in-cave processes that impact the climate signals in stalagmites. As previously mentioned, speleothems that form under conditions of isotopic equilibrium implies isotopic equilibrium between $CaCO_3$, $HCO3^-$, and H_2O (Hendy 1971). However, in-cave properties and processes can lead to disequilibrium isotope fractionation, which considers all chemical and isotope reactions between molecules, which disturb isotope equilibrium (Deininger et al. 2012; Deininger and Scholz 2019). For example, variations in cave air movement can allow for evaporative fractionation of drip water $\delta_{18}O$ values (Deininger et al. 2012) or high supersaturation of drip water with respect to calcite can lead to rapid calcite precipitation after CO_2 degassing (Mickler et al. 2006; Deininger et al. 2012). The drip interval (i.e., time between two subsequent drips) may also influence the degree of isotope disequilibrium (Kaufmann 2003a; Mühlinghaus et al. 2007, 2009; Frisia et al. 2011; Deininger et al. 2012) and ultimately alter stalagmite $\delta_{18}O$ values.

A newly-developed forward model that integrates both karst hydrology and water pathways with in-cave processes is known as Karstolution (Treble et al. 2019). Karstolution incorporates two models, which couples an existing karst hydrology PSM (Baker et al. 2013) with an in-cave fractionation PSM (Deininger and Scholz 2019). Karstolution is useful for better understanding the physical processes occurring at the study site, analyzing the assumptions of karst linearity and in-cave isotopic fractionation, and working with global climate models and

large climate reconstructions (Treble et al. 2019). Karstolution uses an input time series of climate data (e.g., rainfall amount, surface temperature, evapotranspiration, and rainfall $\delta_{18}O$ at a monthly timesteps) and considers a configuration of karst and in-cave conditions to output modelled stalagmite $\delta_{18}O$. Using a PSM such as Karstolution is important when identifying key processes that could alter the climate signal interpreted in the stalagmite $\delta_{18}O$ data. While there are PSMs that also consider changes in stalagmite $\delta_{13}C$ due to various non-climatic factors, this dissertation focuses solely on stalagmite $\delta_{18}O$ PSMs. Specifically, I used Karstolution to identify how hydrologic conditions may influence interannual changes in stalagmite $\delta_{18}O$ using cave-site specific monitoring data.

1.6. Modern Precipitation Variability

Extensive work has been done to better understand more recent changes (~last 50 years) in interannual precipitation change associated with the AM system. Interannual precipitation variability across East China over the last few decades has been well-characterized by meridional dipole and tripole structures (Hsu and Liu 2003; Hsu et al. 2007; Han and Zhang 2009; Ye and Lu 2012). The tripole pattern illustrates wet conditions over the Yangtze River region and dry conditions to the north and south or vice versa (Hsu et al. 2007; Huang et al. 2012; Day et al. 2015). Conversely, the dipole rainfall pattern describes out-of-phase variations in precipitation between southeastern and northeastern China (Ding et al. 2008; Qian et al. 2014; Sun and Wang 2015).

These spatial rainfall patterns across the EASM region has also been observed in historical documents and speleothem records (e.g., Wang et al. 2001a). A recent synthesis of high-resolution paleoclimate records of moisture or precipitation variability from the EASM region

revealed spatially distinct precipitation variations over the last millennium (Chen et al. 2015, 2019a). On centennial timescales, studies have shown various periods during which there were generally drier conditions in southern China, while the northern part was wetter (Chen et al. 2015), representing the observed dipole pattern. On the other hand, the tripole pattern of precipitation variability has been linked to the timing and duration of distinct stages of the EASM related to insolation-forced shifts in the position of the westerlies relative to the Tibetan Plateau during the Holocene (last ~11,700 years) (Kong et al. 2017). Multiproxy paleoclimate evidence has shown that AM precipitation did not respond uniformly to past changes in insolation or AMOC (Chiang et al. 2015; Zhang et al. 2018b; Huang et al. 2018), suggesting that the dipole and/or tripole rainfall patterns may persist across a wide range of timescales.

While several studies have focused on rainfall patterns across the MSEA region, (Misra and DiNapoli 2014; Mie et al. 2015; Tsai et al. 2015; Shrivastava et al. 2017; Ratna et al. 2017), none thus far have analyzed how MSEA precipitation patterns are linked to the observed dipole or tripole precipitation patterns in East China or the dynamic mechanisms responsible for the potential linkage. Evaluation of the underlying interactions altering modern spatial patterns of rainfall across East China and MSEA can provide more insight into past changes in monsoon rainfall and improve interpretation of monsoon and hydroclimate paleoclimate records.

1.7. Research Objectives

My main dissertation objectives are to better understand mainland Southeast Asian climate variability over the Common Era by addressing the following questions:

1. How has Southeast Asian hydroclimate varied over the last two millennia on multidecadal to centennial timescales?

2. What are the dominant mechanisms that characterize interannual MSEA precipitation variability in recent decades?
3. Is there a coupling of modern-day MSEA and East Asian monsoon summer precipitation through meridional tripole and/or dipole spatial modes and what are the driving mechanisms?
4. How can non-linear karst processes and in-cave disequilibrium isotope fractionation alter the stalagmite $\delta_{18}O$ signals and what are the impacts of cave temperature, ventilation, and other metrics on changes in stalagmite $\delta_{18}O$?

1.8. Region of Interest and Study Site

The Southeast Asian Monsoon (SEAM), a regional monsoon of the larger AM system, dominates the modern climate of our study site that is located in northern Laos (Tham Doun Mai Cave, 20°45'N, 102°39'E, elevation 360 m). More than two-thirds of the mean annual precipitation (1195 mm/year) occurs during the summer monsoon months from May–September. The duration of the SEAM wet season is one of the longest of the regional AM systems and extends nearly twice the time of the Indian monsoon (range of 120 to 160 days and 80 to 120 days, respectively) (Misra and DiNapoli 2014). The onset of the SEAM occurs in late boreal spring (May) and is characterized by the sudden shift in winds from northeasterly to southwesterly. Strong winds from the Indian Ocean transport warm moist air into the region and additional moisture flows through directly from the Andaman Sea, and Gulfs of Martaban and Thailand to MSEA (Misra and DiNapoli 2014). The study region focused on in this dissertation is situated at the interface between the Indian and East Asian monsoons, which can lead to complex interactions and precipitation variability over MSEA (Conroy and Overpeck 2011). In

my dissertation, I focus on changes in mostly MSEA hydroclimate and precipitation variability during the Common Era and also include precipitation variations over East China as it pertains to spatiotemporal changes in MSEA rainfall.

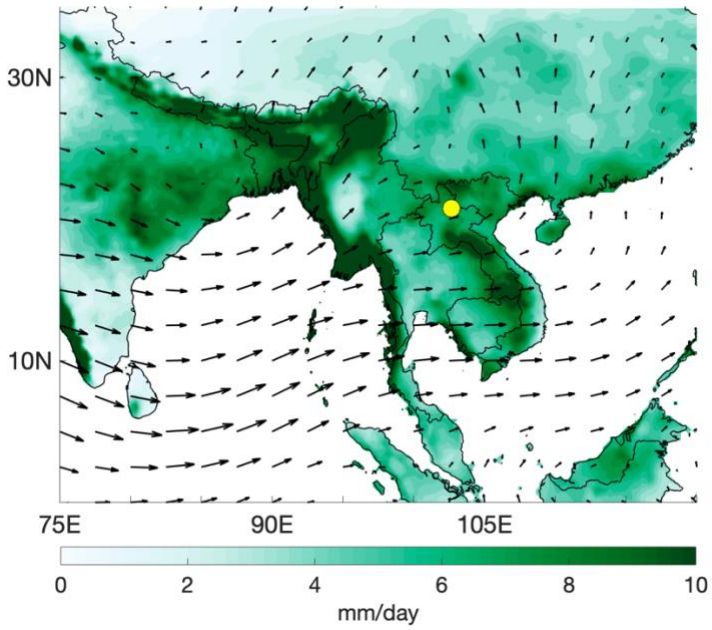

Figure 1.3. Summer (JJAS) precipitation and 850 mb winds climatology. Mean JJAS precipitation (1951-2007 CE) derived from Asian Precipitation - Highly-Resolved Observational Data Integration Towards Evaluation (APHRODITE) (Yatagai et al. 2012). 850 mb winds are derived from NCEP Reanalysis mean (1951-2007 CE) (Kalnay et al. 1996). The location of Tham Doun Mai Cave, Laos is indicated by the yellow circle.

1.9. Chapter Outline

In Chapter 2, I present a new, high-resolution stable isotope record ($\delta_{18}O$ and $\delta_{13}C$) from a northern Laos stalagmite. As previously stated, 'monsoon intensity' is defined as changes in rainfall upstream of our study site (i.e., upstream rainout), specifically over the Bay of Bengal and Indian Ocean, which is most closely related to the strength of the ISM. This definition highlights that an identified increase in monsoon intensity (upstream rainout) recorded at Tham

Doun Mai Cave does not necessarily imply an increase in local precipitation amount above the cave site. Previous work has shown that interannual variations of precipitation $\delta^{18}O$ at our study site do not strongly correlate with local precipitation amount, but instead reflect upstream rainout over the Bay of Bengal and Indo-Pacific warm pool regions, large-scale monsoon intensity, and influences from ocean-atmosphere interactions (Yang et al. 2016). The $\delta^{18}O$ record shows persistent multidecadal to centennial variations in monsoon intensity over the 1900-year record, whereas the $\delta^{13}C$ record exhibits centennial-scale variations in local water balance and highlights the presence of megadroughts that generally match those recorded by tree ring records. In addition to these new paleoclimate data, the study utilizes a novel approach that integrates both paleoclimate data with climate model simulation output. Specifically, solar-forced climate simulations from the Community Earth System Model-Last Millennium Ensemble (CESM-LME) (Otto-Bliesner et al. 2016) were used to disentangle the observed significant correlation between the $\delta^{18}O$ record and solar variability after 1200 CE. The modeling results showed that centennial-scale $\delta^{18}O$ variability over the past millennium may be driven by solar-forced changes in upstream rainout over the tropical Indian Ocean, which modify the $\delta^{18}O$ of moisture transported to our study site without necessarily affecting rainfall amount. Supplementary information is presented in Appendix A.

In Chapter 3, I present a modern observational study that focuses on the interannual precipitation variability across MSEA and East China. I use various data products, including satellite precipitation data and reanalysis climate datasets. The results show that the leading precipitation modes across MSEA and East China are characterized by tripole and dipole precipitation modes. These modes are closely related to and likely influenced by the El Niño Southern Oscillation and the North Atlantic Oscillation, respectively. The first leading mode

(denoted by a tripole precipitation pattern) demonstrates an in-phase precipitation pattern between MSEA (specifically Laos and Vietnam) and South China. However, the second leading mode (denoted by a dipole precipitation pattern) is characterized by an out-of-phase precipitation pattern between MSEA and South China. The conclusions from this study have implications for not only understanding future changes in precipitation patterns in these regions, but also interpreting paleoclimate records reflecting precipitation changes and monsoon patterns across MSEA and East China. While additional work is needed to test the hypotheses presented in this work, this study introduces several mechanisms that may explain past spatial precipitation patterns across the AM region.

In Chapter 4, I use a speleothem proxy forward model, Karstolution (Treble et al. 2019), to identify how key processes within the karst system and changes in hydrologic pathways may alter the stalagmite $\delta^{18}O$ at our study site. By using cave monitoring data and climate inputs from an isotope-enabled global spectral model (IsoGSM) (Yoshimura et al. 2008), I assess how in-cave processes and conditions impact various stalagmites in the same cave through sensitivity analyses. The IsoGSM model applies spectral nudging towards the meteorology captured by the National Center of Environmental Prediction/Department of Energy (NCEP/DOE) reanalyses. Therefore, the precipitation isotopes simulated by IsoGSM closely agrees with the Global Network of Isotopes in Precipitation (GNIP) database (Baker et al. 2013). By modifying the original model configurations, the output data from Karstolution exhibited a one-year lag compared to the output using the original model configurations. These results suggest that variations in karst hydrology and water pathways can directly impact stalagmite $\delta^{18}O$ changes. By configuring the model with monthly means observational data from TM Cave, these results build the foundation in further improving interpretations of TM Cave stalagmite $\delta^{18}O$ variability.

The collective results of my dissertation help us understand both past changes in monsoon intensity, local hydroclimate, and modern-day precipitation patterns across MSEA and surrounding regions impacted by the broader AM system. My interest in the MSEA region is motivated by the limited number of paleoclimate records than span the last two millennia and the high vulnerability of countries within MSEA to precipitation changes associated with anthropogenic climate change. The paleoclimate record from my dissertation is available via NOAA's National Climate Data Center and publicly accessible (doi: 10.1016/j.epsl.2019.115737 https://www.ncdc.noaa.gov/paleo-search/study/27332).

Chapter 2

2 Hydroclimatic variability in Southeast Asia over the past two millennia

Adapted from:

Wang, J.K., K.R. Johnson, A. Borsato, D.J. Amaya, M.L. Griffiths, S. Frisia, G.M. Henderson A. Mason, 2019, Hydroclimatic Variability in Southeast Asia over the Last Two Millennia, Earth and Planetary Science Letters, 525, 115737. doi: 10.1016/j.epsl.2019.115737

Supporting information located in Appendix A.

2.1. Overview

The spatiotemporal variability of the Asian Monsoon (AM) over the last two millennia has been attributed to a combination of external solar and volcanic forcing and/or internal coupled atmosphere-ocean dynamics, but the relative importance of these mechanisms remains unresolved. The present knowledge of multidecadal to centennial-scale AM variability over Mainland Southeast Asia is not well-constrained, despite substantial progress in understanding seasonal to decadal variability from tree ring records. Here we present the first high-resolution stable isotope ($\delta_{13}C$ and $\delta_{18}O$) speleothem record from northern Laos spanning the Common Era (~50 BCE to 1880 CE). The $\delta_{13}C$ record reveals substantial centennial-scale fluctuations primarily driven by local water balance. Notably, the driest period at our site occurred from ~1280 to 1430 CE, during the time of the Angkor droughts, supporting previous findings that this megadrought likely impacted much of Mainland Southeast Asia. In contrast, variations in stalagmite $\delta_{18}O$ reflect changes in rainfall upstream from our study site. Interestingly, the $\delta_{18}O$ record exhibits a positive correlation with solar activity that persists after 1200 CE, contrary to the findings in previous studies. Solar-forced climate model simulations reveal that these $\delta_{18}O$

variations may be driven by solar-forced changes in upstream rainout over the tropical Indian Ocean, which modify the $\delta_{18}O$ of moisture transported to our study site without necessarily affecting local rainfall amount. We conclude that future rainfall changes in Mainland Southeast Asia are likely to be superimposed on multidecadal to centennial-scale variations in background climate driven primarily by internal climate variability, whereas solar forcing may impact upstream rainout over the Indian Ocean.

2.2. Introduction

The Asian Monsoon (AM) system is known to vary on a range of timescales, from orbital to interannual (Wang et al. 2005b; Zhang et al. 2008; Cook et al. 2010; Berkelhammer et al. 2010; Griffiths et al. 2016; Cheng et al. 2016). AM variability has been linked to orbitally-forced changes in Northern Hemisphere summer insolation (Cheng et al. 2016). Additionally, millennial-scale AM changes have been linked to North Atlantic ice rafting events and the corresponding changes in the strength of the Atlantic Meridional Overturning Circulation (AMOC) (Wang et al. 2001b). However, there are fewer studies that have focused on the mechanisms underlying higher-frequency AM variability. Centennial to decadal-scale AM variations have thus far been attributed to some combination of external solar and volcanic forcing (Zhang et al. 2008; Yan et al. 2015) and/or internal coupled ocean-atmosphere dynamics (Cook et al. 2010; Berkelhammer et al. 2010; Buckley et al. 2010; Sinha et al. 2011a), but the relative importance of these mechanisms is still uncertain due, in part, to the paucity of sub-decadal resolution paleoclimate records. Furthermore, projections of AM changes in response to anthropogenic greenhouse gas forcing are still a challenge for climate models (Mohtadi et al. 2016). While most models project that overall AM precipitation will increase despite a projected

weakening of monsoon circulation, no such trends have been clearly observed (Christensen et al. 2013). Recent precipitation trends have instead exhibited substantial regional variability that has been primarily attributed to internal ocean-atmosphere dynamics (Conroy and Overpeck 2011). Given the complex dynamic nature of the AM and the short length of instrumental observations, our understanding of regional AM variability remains incomplete. The development of robust and precisely dated paleoclimate records is therefore critical to better characterize the timing and mechanisms of centennial to decadal-scale regional AM variability over the Common Era.

Speleothem oxygen isotope ($\delta^{18}O$) records from China and India have been widely used to reconstruct past AM variability (Cheng et al., 2016; Sinha et al., 2011a; Wang et al., 2001; Zhang et al., 2008), with more negative values widely interpreted as evidence for a stronger AM and vice-versa. However, the precise mechanism driving the $\delta^{18}O$ in the AM region is still debated and interpretations include changes in local or regional precipitation amount (Berkelhammer et al. 2010; Sinha et al. 2011a), precipitation seasonality (Wang et al. 2001b), atmospheric circulation (Chiang et al. 2015; Zhang et al. 2018a), and the degree of upstream rainout during transport (Pausata et al., 2011). While orbital and millennial scale $\delta^{18}O$ changes have been widely linked to changes in summer insolation and AMOC, respectively, several previous studies have suggested that decadal to centennial-scale speleothem $\delta^{18}O$ variability may be attributed to external solar changes due to significant spectral peaks at frequencies associated with known solar cycles (Neff et al. 2001; Zhang et al. 2008; Zhao et al. 2015). However, given the small radiative forcing associated with solar variability, the complex controls on speleothem $\delta^{18}O$, and the incomplete understanding of physical processes through which solar variations may influence the AM, the nature and robustness of the relationship remain unclear. Other speleothem $\delta^{18}O$ studies have attributed decadal to centennial-scale variability to internal

coupled ocean-atmosphere modes, such as the El Niño Southern Oscillation (ENSO) and the Atlantic Multidecadal Oscillation (AMO) (Berkelhammer et al. 2010; Zhao et al. 2015). Few speleothem studies have utilized additional proxies, such as carbon isotopes, which, when combined with $\delta^{18}O$ data, could add valuable climate information to more fully examine the AM response to both internal climate variability and external forcings.

Speleothem carbon isotope variations ($\delta^{13}C$) have been found to reflect shifts in the local water balance through hydrologically-sensitive processes related to soil and vegetation efficiency and in or above-cave processes (Genty et al. 2001; Johnson et al. 2006; Frisia et al. 2011). Enhanced CO_2 degassing and calcite precipitation in the epikarst or on the cave ceiling during dry periods lead to preferential loss of $^{12}CO_2$ from the infiltrating water to the cave air, which shifts the $\delta^{13}C$ of subsequent stalagmite calcite to more positive values (Johnson et al. 2006). Similarly, decreased soil and root respiration during dry periods can contribute to lower soil pCO_2 and more positive $\delta^{13}C$ values of the carbonate (Bajo et al., 2017). Despite the complex controls on speleothem carbon isotopes, shifts towards more positive $\delta^{13}C$ are often interpreted as drier conditions, whilst more negative $\delta^{13}C$ values are interpreted as wetter conditions above the cave site. For instance, a recent study from southern China reported that centennial-scale changes in speleothem $\delta^{13}C$ were sensitive to local water balance variations associated with regional hydrological change (Liu et al. 2016). Despite recent advances in understanding the factors that control speleothem $\delta^{13}C$ (Wong and Breecker 2015), few studies from the AM region have focused on the link between speleothem $\delta^{13}C$ variability and local hydroclimate or monsoon variability.

At present, limited paleoclimate records that span the last two millennia exist across Mainland Southeast Asia (MSEA), where the majority of rainfall is delivered by the Southeast

Asian Monsoon (Conroy and Overpeck 2011). Even slight changes in the intensity or timing of monsoon rainfall can have profound societal and economic impacts on the region with recent severe droughts and floods (Thirumalai et al. 2017) highlighting the critical need to better constrain the nature of past and future hydroclimate changes. Tree rings and lake sediment records have provided insight on MSEA precipitation variability on interannual to centennial timescales (Buckley et al. 2010; Chawchai et al. 2015; Yamoah et al. 2016a). Absolute-dated precipitation records from tree ring width series spanning the last several centuries suggested that ENSO is one of the most important drivers for interannual to decadal-scale droughts in the region (Cook et al. 2010; Buckley et al. 2010). A multi-proxy record from lake sediments in northern Thailand revealed multidecadal to centennial-scale precipitation variability during the last two millennia, which was linked to low-frequency ENSO-like patterns and/or shifts in the position of the intertropical convergence zone (ITCZ) (Chawchai et al. 2015; Yamoah et al. 2016a). These lake and tree ring records did not provide evidence for a strong solar variability influence on MSEA climate (Buckley et al. 2010), unlike several speleothem $\delta^{18}O$ records from the broader AM region (Zhang et al. 2008; Zhao et al. 2015). This disagreement among climate archives, along with the complex controls on precipitation $\delta^{18}O$, suggests the possibility that solar activity may influence speleothem $\delta^{18}O$ variability without necessarily impacting local hydroclimate.

To address this issue, here we present the first high-resolution, precisely dated speleothem stable isotope ($\delta^{18}O$ and $\delta^{13}C$) record from MSEA spanning the last two millennia. The $\delta^{18}O$ and $\delta^{13}C$ records reveal substantial multidecadal to centennial-scale oscillations, which we interpret as reflecting variations in rainout upstream of our study site and local water balance, respectively. Our $\delta^{13}C$ results suggest that centennial-scale precipitation variations in the region

are likely dominated by internal climate variability. Through comparisons with solar activity records and solar-forced climate model simulations, we propose that solar-forced changes in precipitation over the Indian Ocean may drive multidecadal to centennial-scale speleothem $\delta^{18}O$ variability at our site.

2.3. Study Site and Climatology

Tham Doun Mai Cave (TM cave; 20°45'N, 102°39'E) is a ~3,745 m-long cave located at 352 m above sea level in Luang Prabang Province, Laos (Figure A.1; Appendix A). Mean annual rainfall in the region is ~1,200 mm, ~70% of which is delivered during the summer monsoon season (June-September), when strong southwesterly winds transport warm moisture-laden air masses sourced primarily from the Indian Ocean and Bay of Bengal to MSEA (Figure A.1). Mean monthly rainfall $\delta^{18}O$ values exhibit strong seasonality, with the summer monsoon moisture being significantly depleted in ^{18}O with respect to boreal winter moisture.

Isotope-enabled climate model results showed that modern $\delta^{18}O$ of precipitation at TM cave is not significantly correlated to local precipitation amount (Yang et al. 2016). However, strong correlations with two measures of AM strength, sea level pressure and vertical wind shear over the Indian Ocean and Bay of Bengal, instead suggest an important influence of upstream rainout on precipitation $\delta^{18}O$ at TM cave (Yang et al. 2016). In this study, we utilize the term "AM intensity" to refer to the degree of rainout associated with this convective activity upstream from TM cave, which includes the Indian Ocean, Indian sub-continent, and the Bay of Bengal. Although the influence from the amount effect (i.e., a tendency for lower $\delta^{18}O$ values in rainfall from strongly convective systems) (Dansgaard 1964) cannot be entirely ruled out, we interpret TM speleothem $\delta^{18}O$ values primarily as a proxy for AM intensity. Increased upstream rainout

during strong AM periods leads to more negative $\delta_{18}O$ values at TM cave without necessarily requiring a change in local precipitation amount in northern Laos (Pausata et al. 2011).

2.4. Methods

2.4.1. Speleothem Chronology

Speleothem TM-17 was sampled ~200 m from the cave entrance and was not actively growing at the time of collection. It is a 60 cm long, candle-shaped stalagmite, but for this study we focus only on the top ~4 cm. Seven powdered samples (~200 mg/each) were drilled from the central growth axis of TM-17 using a Dremel tool fitted with a diamond dental bur (Figure 2.1a). $^{230}Th/^{234}U$ ages were determined using multi-collector inductively coupled plasma mass spectrometry (MC-ICP-MS) at the University of Oxford, UK (Table A.1) following methods outlined in previous studies (Hu et al. 2008; Mason and Henderson 2010). All samples were corrected for initial ^{230}Th using an initial $^{230}Th/^{232}Th$ value of $4.4 \pm 2.2 \times 10^{-6}$. The U-Th ages lie in stratigraphic order and range from 229 ± 19 to 1927 ± 12 years before present (years BP, where present equals 1950 CE), indicating an average growth rate of ~20 μm/year (Figure 2.1; Table A.1). High-resolution analyses on TM-17 conducted via synchrotron radiation X-ray fluorescence (XRF) microscopy (Appendix A) show clear laminations in Sr concentration spaced at ~20 μm intervals, suggesting that they are annual in nature. To further constrain the age model, we conducted annual laminae counting on the Sr synchrotron XRF map and anchored this floating laminae counting age model to the U-Th ages using a least-squares fit method (Domínguez-Villar et al. 2012) (Figure 2.1c). The final age model indicates that TM-17 formed between ~50 BCE to 1880 CE with an average age uncertainty of 26 years (Appendix A).

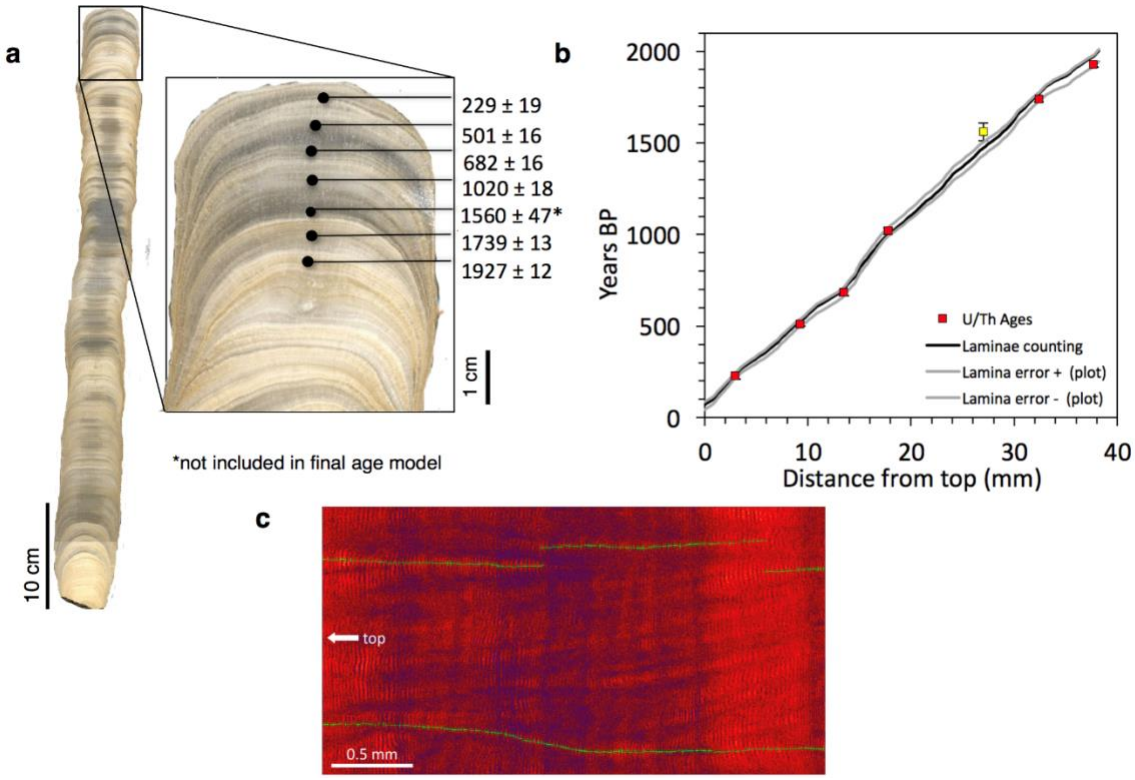

Figure 2.1. TM-17 morphology and age model (a) Scanned image of stalagmite TM-17 cut parallel to the growth axis. Zoomed-in image shows the section of stalagmite TM-17 composed by alternating compact columnar calcite layers (dark grey) and porous columnar calcite layers. Black dots indicate the positions of ^{230}Th dates measured. The ages are reported in years BP (before 1950 CE). (b) Age-depth plot using the U-Th ages (red squares) coupled with the laminae counting. The 2σ U-Th error bars are shown, but in most cases are smaller than the symbols. The grey thick lines correspond to age model uncertainty constructed from the U-Th 2σ error bars by propagating the 3% laminae counting (LC) error within each section between two adjacent U-Th ages. The yellow square represents the U-Th age (U3) that was not included in the final age model due to the large uncertainty on the raw age, which indicates a poor analysis. (c) Strontium synchrotron micro XRF map of the central section of TM-17**.** The map is rendered in temperature scale (red = high, blue = low value). The alignments of green crosses centered on the lower intensities (blue) laminae at the top and bottom of the image visualize two sets of laminae counting.

2.4.2. Stable Isotope Analyses

A total of 903 powdered samples were micromilled at 0.04 mm intervals (~2- to 4-year resolution) along the central growth axis of TM-17. Powdered samples (~30-70 mg) were weighed and analyzed for carbon and oxygen isotope (δ^{13}C, δ^{18}O) composition on a Thermo

Finnigan Kiel IV carbonate device coupled with a Delta V Plus isotope ratio mass spectrometer at the University of California, Irvine. All results are expressed using conventional δ notation in per mil (‰) relative to the V-PDB standard. A total of 18 standards (IAEA-CO-1, NBS-18, and OX, an in-house quality control standard) were analyzed during each run of 28 unknown samples. Duplicate measurements of NBS-18 and IAEA-CO-1 standards show a long-term standard deviation of 0.04 ‰ for $\delta_{13}C$ and 0.07‰ for $\delta_{18}O$ (1σ).

2.4.3. Model Analyses

To assess the influence of solar-forced tropical climate variability on multidecadal TM-17 $\delta_{18}O$ fluctuations, we used runs from the Community Earth System Model Last Millennium Ensemble (CESM-LME) (Otto-Bliesner et al. 2016). CESM-LME is available from 850-2005 CE with a vertical resolution of 30 pressure levels in the atmosphere and a horizontal resolution of ~2° for the atmosphere and land and ~0.3°-1.0° for the ocean and sea ice coupled model. In the present study, we analyzed the ensemble mean of four runs forced only with varying solar intensity (Otto-Bliesner et al. 2016) and perturbed with slightly different initial conditions. To better compare our record with CESM-LME variables, we interpolated TM-17 $\delta_{18}O$ to regularly spaced time intervals of every two years from 50 BCE to 1878 CE (n = 965). Likewise, the ensemble mean anomalies were then annually averaged and interpolated to our regularly spaced age model from 850 CE to 1878 CE (n = 515). To isolate low-frequency variability, TM-17 $\delta_{18}O$ and model data were then subject to a 4_{th}-order Butterworth filter with a 50-year period cutoff. Comparisons were then made between our low-passed $\delta_{18}O$ record and the low-passed ensemble mean from 1200 CE to 1878 CE. We chose to focus on this time period due to the high temporal

coherence multidecadal to centennial timescales between our record and the total solar intensity used to force CESM-LME that begins around 1200 CE (Figure 2.3e, Figures. A.5 and A.6).

As a measure of the zonal circulation along the equator, we calculated the zonal mass streamfunction (ψ_x) as:

$$\psi_x(t,x,p) = \frac{2\pi a}{g}\int_0^p [u_D]dp \qquad (1)$$

Where a is the radius of the earth, g is the gravitational constant, p is pressure, and $[u_D]$ is the divergent component of the zonal wind field averaged from 5˚S-5˚N (Yu and Zwiers 2010).

Correlation significance for the model analyses was determined using Monte-Carlo methods. First, we generated 1,000 different pairs of uncorrelated, white noise time series and subjected them to a 4th-order Butterworth filter with a 50-year period cutoff. Then, we correlated these low-passed random pairs of time series and created a null distribution of correlation coefficients. Unless otherwise noted, correlations between TM-17 $\delta^{18}O$ and CESM-LME model data were taken to be significant if they fell outside of the 95% confidence interval of this null distribution.

2.5. Results

The TM-17 $\delta^{18}O$ values range from - 9.2‰ to - 8.0‰ and exhibit multidecadal to centennial-scale fluctuations with lower values recorded from ~50 BCE to 500 CE and higher values from 1200 CE to 1880 CE (Figure 2.2a, Figure A.2). These variations are likely dominated by low-frequency changes in AM intensity, though they may also be modified in part

by hydrological processes in the epikarst (Bradley et al., 2010; Evans et al., 2013) (Appendix A). These hydrologic effects have the potential to filter or reduce the amplitude of seasonal to interannual climate frequencies leading to hydrologic "smoothing" or reddening of the $\delta_{18}O$ signal during the proxy formation process as precipitation infiltrates through the epikarst. These processes therefore may shift interannual to decadal-scale speleothem $\delta_{18}O$ signals towards lower frequencies relative to the associated climate signals, though these effects are less likely to influence the multidecadal to centennial-scale variations we focus on here (Bradley et al. 2010; Dee et al. 2017; PAGES Hyro2k Consortium 2017).

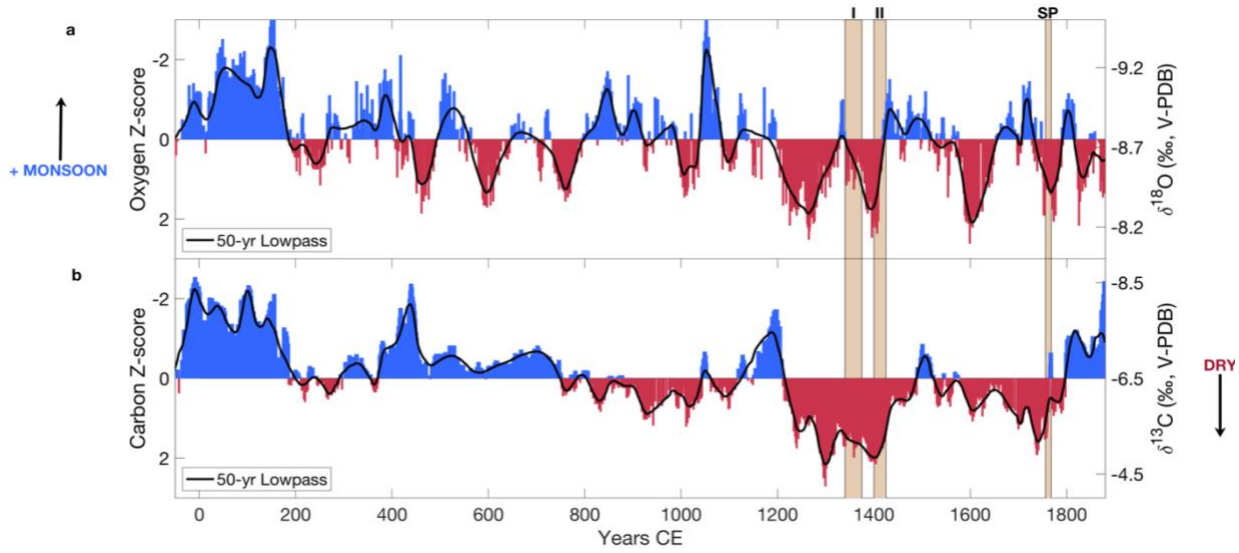

Figure 2.2. Stable isotope record of Southeast Asian hydroclimate from stalagmite TM-17. (a) $\delta_{18}O$ record and (b) $\delta_{13}C$ record. Standard (z) scores are shown for records. The black lines represent the 50-year low pass filtered data. $\delta_{18}O$ values are interpreted as reflecting monsoon intensity, whereby more negative z-scores (blue) reflect increased monsoon intensity (upstream rainout) and vice versa. $\delta_{13}C$ values are interpreted as a local water balance record, whereby more negative z-scores (blue) represent wetter conditions and positive values (red) represent drier conditions at the cave site. Vertical brown bars identify the Angkor I and II Droughts (I and II, respectively) (Buckley et al. 2010) and the Strange Parallels Drought (SP; 1756-1768 CE) (Cook et al. 2010).

The TM-17 $\delta_{13}C$ values range from -8.4‰ to -4.4‰ and are characterized by multidecadal to centennial-scale variability that is superimposed on a millennium-long positive trend, with more negative values from 51 BCE to 750 CE and more positive values from ~1200 to 1800 CE (Figure 2.2b; Figure A.2). Considering that the TM-17 stalagmite has a regular and straight candle-shaped morphology and columnar fabric (Figure 2.1), indicative of a slow and almost constant drip rate (Frisia and Borsato, 2010), it is reasonable to infer that the $\delta_{13}C$ increases were mainly driven by climate-related soil and/or vegetation processes associated with drier conditions (Mühlinghaus et al. 2007) (Appendix A). Similar to the processes impacting $\delta_{18}O$, it is also likely that vegetation and soil processes may act to smooth the interannual to decadal-scale precipitation variability, leading to apparent reddening of the $\delta_{13}C$ spectra compared with the precipitation signal.

2.6. Discussion

2.6.1. Regional Monsoon Variability and Drought History

To evaluate the regional coherency of AM variability, we compare high-resolution, precisely dated speleothem records that span the last millennium or longer with the TM-17 $\delta_{18}O$ record. Stalagmite $\delta_{18}O$ records from Wanxiang and Dongge Caves, China (Zhang et al. 2008; Zhao et al. 2015) and a composite record from Dandak and Jhumar Caves, India (Sinha et al. 2007, 2011a) reveal similar multidecadal to centennial-scale $\delta_{18}O$ fluctuations over the last millennium, but the TM-17 record does not exhibit strong correlations with these records (Figure 2.3). This disagreement may reflect a combination of chronological uncertainty, hydrologic processes, and/or differences in regional climatology and precipitation $\delta_{18}O$ controls (Hu et al. 2017; PAGES Hyro2k Consortium 2017).

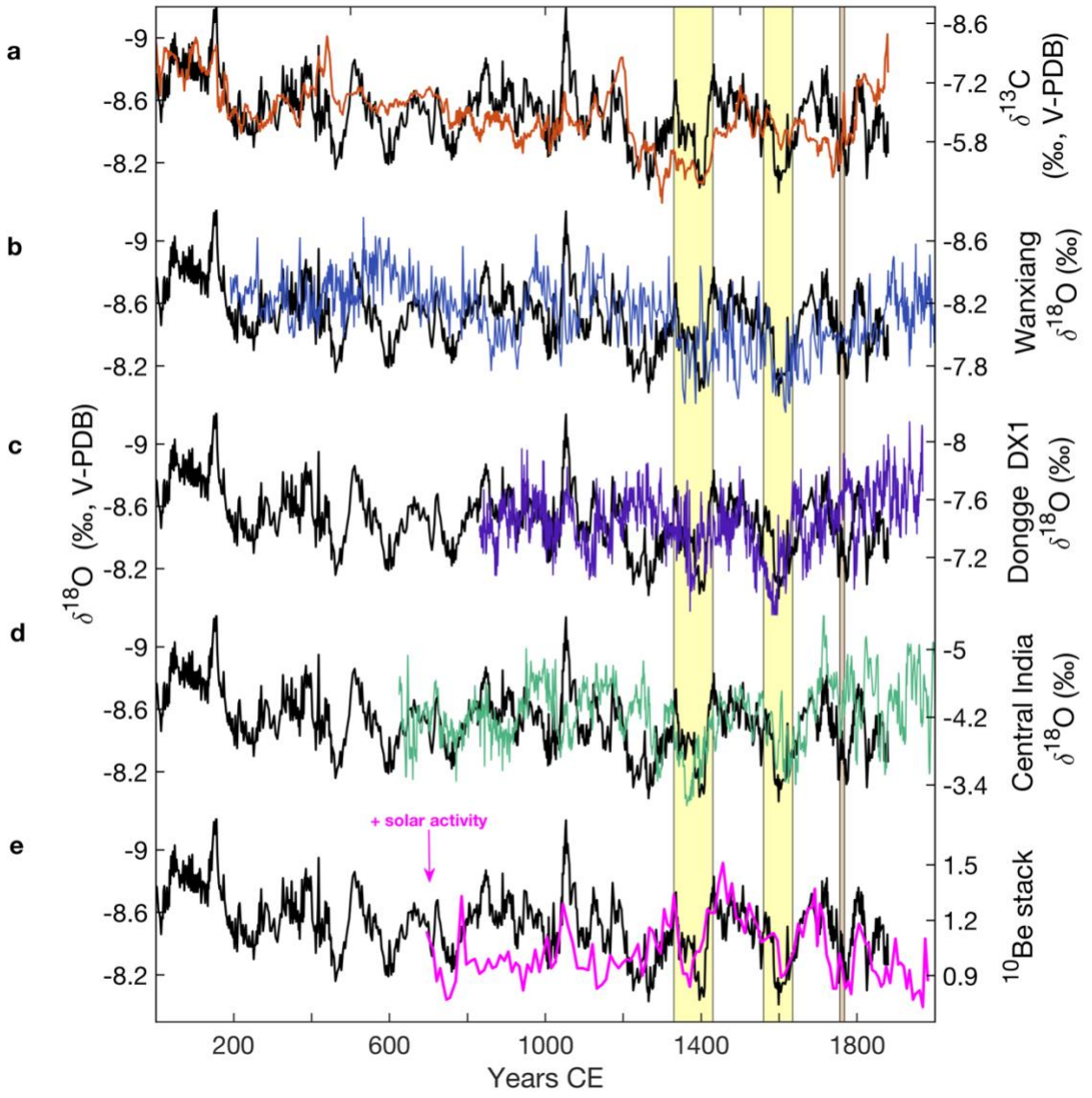

Figure. 2.3. Comparison of the TM-17 record with regional speleothem records and solar activity. The black line in all panels shows the stalagmite TM-17 $\delta_{18}O$ record compared with (a) Stalagmite TM-17 $\delta_{13}C$ (this study). (b) Stalagmite $\delta_{18}O$ from Wanxiang Cave, China (Zhang et al. 2008). (c) Stalagmite $\delta_{18}O$ from Dongge Cave, China (Zhao et al. 2015). (d) Composite stalagmite $\delta_{18}O$ record from Dandak and Jhumar Caves (Sinha et al. 2011a). (e) $_{10}$Be stack derived from Central Antarctica ice cores (Delaygue and Bard 2011). The vertical yellow bars denote the "weak monsoon" periods (1330-1430 CE and 1560-1635 CE). The y-axes in all panels are oriented such that weaker monsoon intensity and stronger solar activity are down.

Nevertheless, some common features of the records are worth discussing in more depth, such as two notable "weak monsoon" periods dated from 1330 to 1430 CE and from 1560 to 1640 CE that appear in all four records (Figure 2.3). These periods correspond to the highest $\delta^{18}O$ values observed in the four stalagmite records and coincide with historical accounts of famine in India (Sinha et al. 2007) and social turmoil in China (Zhang et al. 2008). These weak monsoon periods recorded in these stalagmites suggest a common mechanism driving precipitation $\delta^{18}O$, which, as the modern precipitation $\delta^{18}O$ systematics suggests (Yang et al., 2016) does not necessarily imply synchronous precipitation amount changes at each site. For instance, decreased rainfall over the Indian monsoon region could lead to increased $\delta^{18}O$ at the Indian cave sites due to the amount effect, but also increased $\delta^{18}O$ of precipitation at "downstream" cave sites in Southeast and East Asia due to the upstream rainout mechanism and vice versa (Pausata et al. 2011). Alternatively, decreased rainout upstream of all sites could also lead to consistent shifts in $\delta^{18}O$ towards more positive values at each location.

The TM-17 $\delta^{13}C$ record exhibits the most positive values from 1280 to 1430 CE (Figure 2.2b), suggesting the driest conditions of the last two millennia occurred during this period. Similarly, the Lake Pa Kho record from Thailand exhibits some of the driest conditions and lowest effective moisture from ~1300 to 1500 CE (Chawchai et al. 2015; Yamoah et al. 2016a) (Figure A.3). Tree-ring based Palmer Drought Severity Index (PDSI) records from the AM region identified two major drought periods during the late 14^{th} and early 15^{th} centuries. These were referred to as the Angkor I and II droughts, which were then related to the collapse of the Khmer Empire (Buckley et al. 2010, 2014) (Figure 2.3). This period also coincides with a growth hiatus in a ^{14}C-dated speleothem record from Cambodia that was interpreted as indicating drought conditions (Hua et al. 2017). The tree ring records also highlight the spatially-extensive

Strange Parallels (SP) megadrought (1756–1768 CE), which coincided with widespread famine in India and China (Cook et al. 2010; Buckley et al. 2014). This event is clearly expressed as positive $\delta_{13}C$ and $\delta_{18}O$ excursions in TM-17, indicating dry conditions in northern Laos and weakened monsoon intensity, respectively, at that time (Figure 2.2).

Given the different controls on speleothem $\delta_{18}O$ and $\delta_{13}C$ values and the substantial variability in regional precipitation patterns in the AM region (Conroy and Overpeck 2011), it is not unusual for regional proxy records to exhibit discrepancies or fall out of phase from one another during some periods. For example, the TM-17 $\delta_{13}C$ record, Vietnamese tree ring records (Buckley et al. 2010) and Thai lake records (Chawchai et al. 2015; Yamoah et al. 2016a) do not show significant evidence for drought-like conditions during the second identified weak monsoon period from 1560 to 1635 CE (Figure A.3), which other studies identified as an extreme drought period in China and India (Zhang et al. 2008; Zhao et al. 2015). Furthermore, previous studies from the broader AM and tropical Pacific regions have focused on disentangling contrasting hypotheses to explain anomalous climate intervals, particularly the Medieval Climate Anomaly (MCA, 950-1250 CE) and the Little Ice Age (LIA, 1400-1850 CE) (Griffiths et al. 2016). Some paleoclimate proxy records link meridional shifts of the ITCZ to key changes in tropical Pacific hydroclimate (Zhang et al. 2008; Sachs et al. 2009; Tierney et al. 2010), while others implicate the influence of ENSO and associated zonal shifts of deep convection as the dominant drivers (Yan et al. 2011; Konecky et al. 2013). The TM-17 $\delta_{18}O$ record suggests decreased AM intensity, while the $\delta_{13}C$ record indicates overall drier conditions during the LIA, both of which are consistent with records of hydroclimatic variability in MSEA and Palau (Buckley et al. 2010; Richey and Sachs 2016; Yamoah et al. 2016a) (Figure 2.2, Figure A.3). The drying trend and/or drought-like conditions observed from these records conflict with other

paleoclimate records from the South China Sea (Yan et al. 2015) and Indonesia (Konecky et al. 2013), which show wetter conditions during the LIA that can be linked to a meridional ITCZ contraction and/or zonal deep convection shifts (Figure A.3). While the TM-17 record supports previous findings of dry conditions in MSEA during the LIA that point to a southward shift of the ITCZ or shifts in zonal convection, it has no clear evidence for a significant hydroclimatic shift during the MCA.

2.6.2. Solar influence on Low-Frequency $\delta^{18}O$ Variability

Previous studies have suggested a relationship between solar activity and AM speleothem $\delta^{18}O$ changes on multidecadal to centennial timescales (Neff et al., 2001; Zhang et al., 2008; Zhao et al., 2015), though some found that the relationship was either temporally inconsistent or only played a minor role (Berkelhammer et al. 2010; Sinha et al. 2011b). We investigated the potential influence of solar activity by comparing the TM-17 $\delta^{18}O$ and $\delta^{13}C$ time series with three records of solar variability: total solar irradiance (TSI) (Vieira et al. 2011), sunspot number (Solanki et al. 2004), and ^{10}Be concentrations derived from ice cores (Delaygue and Bard 2011) (Figures 2.3e and A.5). Reported correlation coefficients are Pearson's *r* values. Significance testing was conducted using a combination of 1,000 Monte Carlo iterations and time-series modeling in the frequency domain to consider the effect of serial correlation (Macias-Fauria et al. 2012). Notably, the most significant correlations between the $\delta^{18}O$ profile and reconstructed TSI ($r = 0.42$, $p < 0.01$), sunspot number ($r = 0.40$, $p < 0.05$), and ^{10}Be concentration ($r = -0.55$, $p < 0.01$) occur after 1200 CE for both unfiltered and 50-year low passed filtered data (Figures. A.5 and A.6, Table A.2). These significant correlations suggest decreased AM intensity corresponds with periods of increased solar irradiance and vice versa. By contrast, the TM-17

$\delta_{13}C$ record, exhibits no significant correlation with solar activity (Figure A.5), indicating that internal variability may be a more important driver of local precipitation on multidecadal to centennial timescales. We note that a potential caveat of this analysis stems from the age uncertainty in the proxy records (Hu et al. 2017) but given the strong similarities between the TM-17 $\delta_{18}O$ record and all three solar proxy records on multi-decadal to centennial timescales, this relationship is worth further consideration. We therefore focus the remainder of our discussion on the potential solar influence on the TM-17 $\delta_{18}O$ record, which does appear to be consistent with changes in solar irradiance (Figures A.5 and A.6).

To further investigate solar influence, we conducted cross-wavelet analyses between the $\delta_{18}O$ values and solar activity proxy records (Figure A.6). A strong shared power on multidecadal to centennial timescales between $\delta_{18}O$ and TSI, sunspot number, and $_{10}Be$ was observed. While the phasing between $\delta_{18}O$ and sunspot number oscillates, suggesting a less consistent influence of solar irradiance, there is consistent phasing post-1200 CE among all three solar proxies, specifically during the Spörer (1400-1510 CE) and Maunder (1645-1715 CE) Minimums (Figure A.5 and A.6). Spectral analysis of the TM-17 $\delta_{18}O$ data does not provide evidence for a robust or persistent ~210-year cycle (Figure A.2 and Appendix A), whereas other stalagmite records have revealed significant periodicities similar to the ~210-year solar cycle of de Vries-Suess (Wang et al. 2005b; Novello et al. 2016). Persistent multidecadal to centennial-scale periodicities, however, emerge in the wavelet transform analysis (Figure A.2) as well as persistent centennial-scale power at in the wavelet coherence analysis with the solar proxies (Figure A.6), in particular after 1200 CE.

This monsoon-solar relationship observed in our record contrasts with earlier studies that observed the opposite relationship, such that periods of increased AM rainfall correspond with

periods of increased solar irradiance (Zhang et al. 2008; Zhao et al. 2015). While these Chinese stalagmite studies note that some periods of decreased solar irradiance, such as the Spörer Minimum, coincide with wetter conditions, they attribute this to the influence of internal climate variability (Zhang et al. 2008; Zhao et al. 2015). A recent southeastern Tibetan Plateau stalagmite $\delta_{18}O$ record, on the other hand, revealed a monsoon-solar relationship similar to our findings: multiple periods of increased AM rainfall (more negative $\delta_{18}O$) were associated with decreased solar activity over the last millennium (Tan et al. 2018). Similarly, a positive relationship between South American Summer Monsoon (SASM) intensity and solar irradiance on centennial timescales was recently inferred from a stalagmite $\delta_{18}O$ record from Midwestern Brazil (Novello et al. 2016). This suggests that solar forcing could potentially lead to an anti-phase relationship between SASM and AM speleothem records, similar to the so-called global monsoon pattern observed on longer timescales and linked with meridional ITCZ shifts (Cheng et al. 2012a). A comparison between our TM-17 $\delta_{18}O$ record and SASM proxy records, however, does not show a significant inverse relationship on multidecadal to centennial timescales (Figure A4). This mismatch may reflect multiple factors, including chronological limitations, regional variability in monsoon precipitation patterns, differing controls on speleothem $\delta_{18}O$, and/or the complex climate dynamics linking AM with SASM climate.

In addition to an opposite monsoon-solar relationship, the temporal nature of the relationship also differs between our study and previously published records, all of which suggest non-stationary behavior in the solar forcing-AM relationship. For example, the Wanxiang Cave record showed similar timing between AM and solar irradiance peaks between ~950-1250 CE (Zhang et al. 2008), whereas the Dandak Cave record showed coherence between Indian summer monsoon precipitation amount and solar variability from ~800-1290 CE

(Berkelhammer et al. 2010). As a result of these temporally inconsistent relationships, both studies concluded that internal climate variability was likely a more important factor driving local hydroclimate change. It is interesting that our observed monsoon-solar relationship appears to strengthen at ~1200 CE, around the time these other relationships weakened, and persists for the remainder of the record (~680-year period). This may reflect true spatiotemporal variability in the response of precipitation $\delta_{18}O$ to solar forcing in the AM region (Tan et al. 2018), though could also reflect the variable influence of internal coupled climate modes such as ENSO or the AMO on AM intensity (Zhao et al., 2015; Berkelhammer et al., 2010).

Overall, our results imply that solar variability may exhibit a significant influence on the TM $\delta_{18}O$ record, in particular since 1200 CE. These results warrant further consideration for the role of solar forcing on changes in AM precipitation and, hence speleothem, $\delta_{18}O$. Here we conduct a more through exploration of the potential mechanisms underlying the observed strong positive correlation between TM-17 $\delta_{18}O$ and solar variability (Figure 2.3e, Figures. A.5 and A.6) utilizing climate model simulations.

2.6.3. Atlantic SSTs Influence Asian Monsoon Precipitation $\delta_{18}O$

To explore solar-forced mechanisms that could influence low-frequency $\delta_{18}O$ variability at our site, we correlated the low-pass filtered TM-17 $\delta_{18}O$ record (50-year cutoff) with the ensemble mean of the "solar forcing only" simulations in the Community Earth System Model Last Millennium Ensemble (CESM-LME) (Otto-Bliesner et al. 2016). Each solar-forced ensemble member of CESM-LME is initialized by slightly different initial conditions, which largely cancel out in the ensemble mean. Therefore, CESM-LME ensemble mean variability can be interpreted as having been driven by the common external forcing (i.e. solar forcing). Since

TM-17 $\delta_{18}O$ showed some consistency with the same solar variability that is used to force CESM-LME, it is reasonable to compare our time series directly to the CESM-LME ensemble mean as a first approximation of how solar forcing may influence AM intensity as it pertains to the time variability of our record.

We primarily focused on the period since 1200 CE, since TM-17 $\delta_{18}O$ exhibits significant correlations during this time period with all three solar records (Table A.2). Correlations of TM-17 $\delta_{18}O$ with solar-forced CESM-LME sea surface temperature (SST) anomalies reveal the strongest and most significant positive correlations with tropical Atlantic SSTs (Figure 2.4). This relationship is significant in all four solar-forced ensemble members (Figure A.7), increasing our confidence that these correlations are not spurious. In addition, we repeated the model analysis for the full overlapping period between the $\delta_{18}O$ and LME runs in the solar-only forcing runs. The results are qualitatively consistent, suggesting that the relationship is physically consistent (Figure A.8).

Previous studies have suggested that the relatively small radiative forcing from solar variability could potentially explain large SST changes in the Atlantic via non-linear responses of the climate system to amplifying feedbacks (Gray et al. 2010). For instance, a "top-down" mechanism was proposed, wherein solar-induced changes to stratospheric ozone and temperature gradients propagate downwards to influence North Atlantic atmospheric and ocean circulation (Meehl et al. 2009). These changes may be further amplified through feedbacks related to the AMOC (Caesar et al. 2018). Alternatively, it has been proposed that the small solar forcing signal may be amplified through "bottom-up" processes involving coupled atmosphere-ocean dynamics and associated changes to the Walker and Hadley circulation (Meehl et al. 2009). Regardless of how tropical Atlantic SSTs may respond to solar forcing, we utilized the CESM-

LME solar-forced simulation to further explore mechanisms through which solar-forced SST changes in the tropical Atlantic could influence AM intensity and, hence, speleothem $\delta_{18}O$ at the TM cave site.

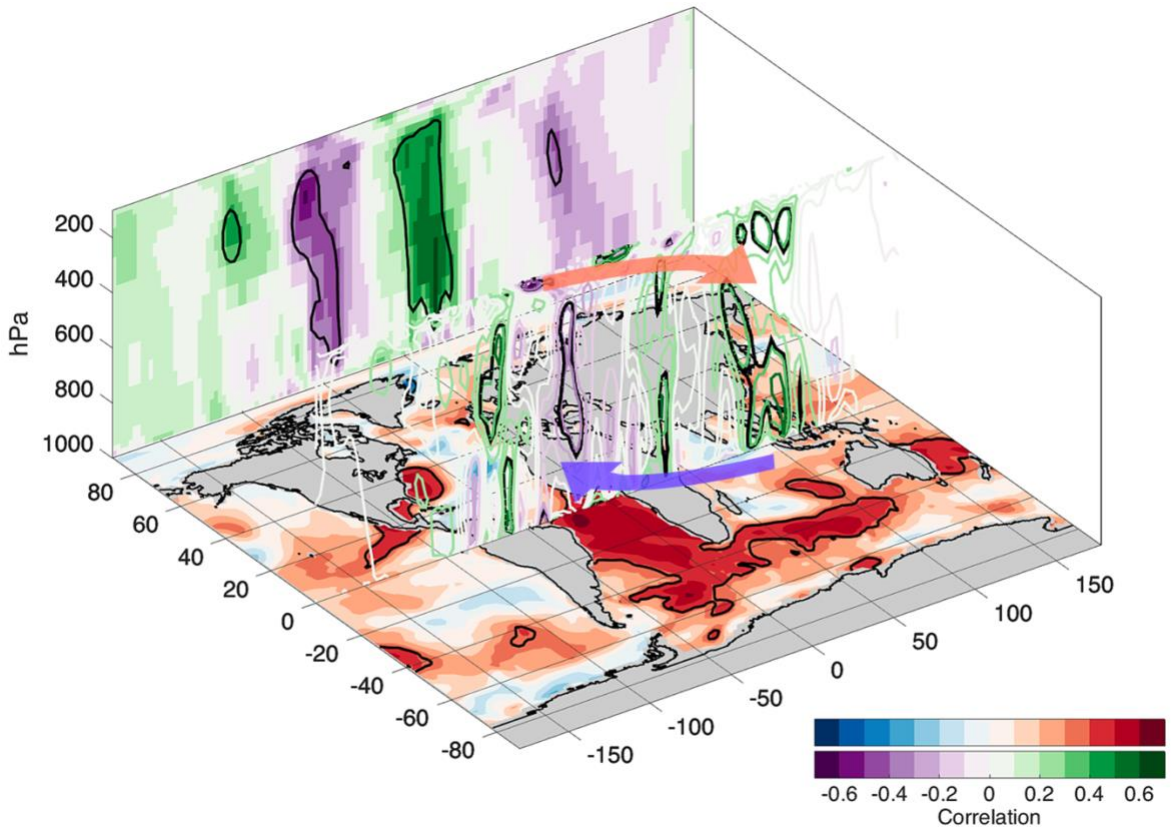

Figure 2.4. Atmosphere-ocean response to solar forcing. TM-17 $\delta_{18}O$ correlations with ensemble mean CESM-LME solar forcing only SST anomalies (x/y plane shading), omega (ω) (x/z contours), and the zonal mass streamfunction (ψ (x/z shading) averaged 5˚S-5˚N. The sign convention is such that positive (negative) ω and ψ correlations correspond to subsidence (convection) and clockwise (counter-clockwise) circulations, respectively. Note the ψ section on the back wall corresponds to values straddling the equator. Thick black contours indicate correlation significance at 95% confidence level. The blue arrow illustrates surface flow converging onto the warm tropical Atlantic, whereas the red arrow indicates upper-level divergence associated with the resulting deep convection.

Our results show that $\delta_{18}O$ is significantly negatively correlated with a dipole of zonal mass streamfunction (ψ_x) circulation anomalies that straddle the tropical Atlantic and are

consistent with the low-level convergence of near-surface winds initiated by warmer Atlantic SSTs (Figure 2.4 back wall shading). These convergences lead to increased deep convection over the tropical Atlantic, which is also apparent in $\delta^{18}O$ correlations with model vertical velocity (ω) (Figure 2.4 equatorial vertical cross-section). Deep convection over the warm Atlantic is compensated by broad zonal bands of atmospheric subsidence over much of eastern Africa and the eastern tropical Indian Ocean, as indicated by positive correlations between CESM-LME ω and TM-17 $\delta^{18}O$ over these regions (Figure 2.4). Subsidence over the tropical Indian Ocean consequently promotes increased atmospheric stability, lower cloud heights, and decreased precipitation, which are consistent with correlations between speleothem $\delta^{18}O$ values correlations and modeled precipitation (Figure 2.5). Taken together, our results suggest that less upstream rainout over the tropical Indian Ocean, a key source of moisture to the broad AM region (Baker et al. 2015; Pathak et al. 2017), could lead to more positive $\delta^{18}O$ values of the water vapor reaching TM.

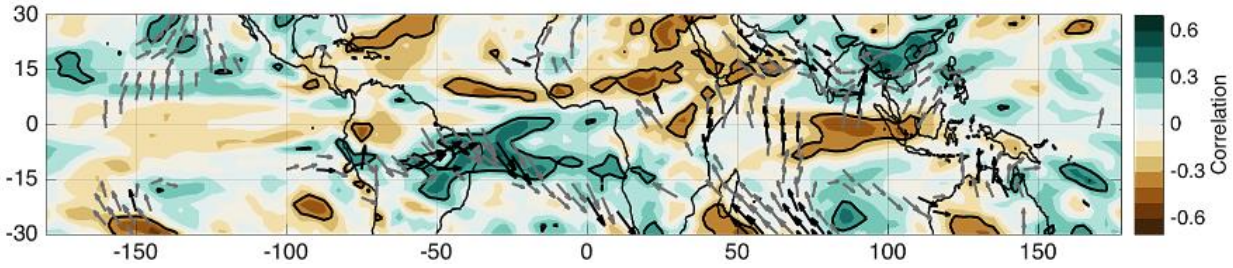

Figure 2.5. TM-17 $\delta^{18}O$ correlated with ensemble mean CESM-LME solar forcing-only precipitation**.** TM-17 $\delta^{18}O$ correlated with CESM-LME total precipitation rate (shading) and 850mb wind fields (arrows). Thick black contours and black (grey) arrows indicate correlation significance at 95% (80%) confidence level based on the distribution of 1,000 randomly generated low-pass filtered time series. All time series were subjected to a 50-year low pass filter.

Correlations between TM-17 $\delta^{18}O$ with 850 mb winds reveal increased cross-equatorial southerly winds from the tropical Indian Ocean and further supports that decreased precipitation

over the tropical Indian Ocean could lead to the transport of higher $\delta^{18}O$ moisture to TM Cave (Figure 2.4). These changes may be further reinforced by increased contribution of ^{18}O enriched moisture from the Bay of Bengal. However, it is difficult to quantitatively distinguish the relative importance of upstream rainout or other potential factors (such as moisture source region or rainfall amount) controlling multidecadal to centennial-scale $\delta^{18}O$ variability without long-term isotope-enabled climate model simulations and other multi-proxy speleothem data.

Volcanic eruptions represent the largest natural forcing to the climate system over the last millennium (Robock 2000) and can potentially explain long-term trends seen in last millennium reconstructions (McGregor et al. 2015). To investigate whether volcanic forcing could provide an alternate explanation for the TM-17 $\delta^{18}O$ variability, we repeated our analyses with the CESM-LME volcanic-only runs and found no similar correlations that would indicate a substantial volcanic influence on our record (not shown), which provides us confidence in our solar results. However, when we repeated our analyses using the CESM full-forcing runs, we found that the full forcing results were more similar to the volcanic-only runs. A possible explanation may be that strong volcanic forcing events are the single largest radiative forcing agents in the fully forced ensemble mean and therefore dominate the overall signal (Otto-Bliesner et al. 2016). As such, this may make it difficult to identify solar-forced changes in the full-forcing experiments that are relatively subtle compared to the strong volcanic eruptions used to force CESM-LME. Additionally, there are likely large uncertainties in the timing and magnitude of volcanic eruptions used to force CESM-LME (Sigl et al. 2014). Finally, our record does not preclude the possibility of volcanic influence on interannual to decadal-scale precipitation $\delta^{18}O$ variability, which may be reddened or otherwise obscured by karst hydrologic

processes. Therefore, despite these discrepancies, our results may still offer insight on the influence of solar forcing on multi-decadal to centennial-scale precipitation $\delta^{18}O$ variability.

2.6 Conclusions

This study presents a new high-resolution speleothem stable isotope ($\delta^{18}O$ and $\delta^{13}C$) record from northern Laos that spans most of the Common Era (~50 BCE to 1880 CE). The $\delta^{18}O$ record is interpreted to reflect upstream rainout over the Indian Ocean, Bay of Bengal, and Indian monsoon region, whereas the $\delta^{13}C$ record reflects local water balance through impacts on soil-vegetation processes. The $\delta^{18}O$ record contains significant multidecadal to centennial-scale variability and exhibits positive correlations with records of solar variability, which are opposite to those previously reported (Zhang et al. 2008; Zhao et al. 2015). The $\delta^{13}C$ record, on the other hand, shows no relationship to solar forcing, but does contain significant centennial-scale variability, with generally dry conditions throughout the LIA. The driest conditions of the record occur during the 13th-15th centuries, consistent with other regional records (Buckley et al. 2010, 2014; Chawchai et al. 2015; Yamoah et al. 2016a). Overall, the $\delta^{13}C$ record provides evidence that internal variability likely played a more important role than solar forcing in driving multidecadal to centennial-scale precipitation variability in MSEA.

Based on the observed solar forcing-$\delta^{18}O$ relationship, this study proposes one hypothesis to explain multidecadal to centennial-scale variations in speleothem $\delta^{18}O$ possibly associated with solar-forced increases in convection and rainfall over the Indian Ocean. Results of the solar forcing only experiments from the CESM-LME suggest that increased tropical Atlantic SSTs resulting from increased solar irradiance may lead to modifications in zonal atmospheric circulation and increased subsidence over the tropical Indian Ocean, leading to less upstream

rainout over a key moisture source for the AM region (Baker et al. 2015; Pathak et al. 2017). This proposed mechanism offers a plausible explanation for the increased speleothem $\delta_{18}O$ values at our site during periods of increased solar activity, without requiring any solar-forced changes in local precipitation amount, thus providing a potential explanation for some periods when the $\delta_{18}O$ and $\delta_{13}C$ records differ.

While age uncertainty and proxy formation processes present challenges for conducting this type of multi-proxy analysis and data-model comparison (Hu et al. 2017; PAGES Hyro2k Consortium 2017), the data presented here provide a baseline of MSEA natural climate variability on multidecadal to centennial timescales, which is critical for understanding the extent that external forcing and internal variability will impact AM intensity and MSEA water resources in the coming decades. Through a novel model-data comparison, we propose a new mechanism to explain the potential solar influence on AM region precipitation $\delta_{18}O$. Future research including development of additional high-resolution paleoclimate records, isotope-enabled climate model analyses, and proxy system modeling will be needed to further constrain the impacts of external forcing and internal climate variability on speleothem $\delta_{18}O$ and $\delta_{13}C$ records in the AM region.

Acknowledgements

We thank Joyce White, Bounheuang Bouasisengpaseuth, Norseng Sayvongdouane, Sengphone Keophanhya and other participants in the Middle Mekong Archaeology Project and Lao government officials and departments for their assistance with the fieldwork, which was funded in part by Henry Luce Foundation grant to the University of Pennsylvania Museum. We would like to thank D. Zhang for assistance with stable isotope analyses and D. Howard, V. Vanghi,

and E. Anderson for assistance in synchrotron analyses. This work was supported by National Science Foundation P2C2 awards 1603056 and 1405472 to K.R.J., and NSF awards 1602947 and 1404932 and a William Paterson University Center for Research summer grant to M.L.G. This work was also supported by NSF Graduate Research Fellowships DGE-1321846 to J.K.W and DGE-1144086 to D.J.A. Petrographic and synchrotron work was supported by the Australian Research Council Discovery Project grant DP160101058 to S.F. The XRF analyses were undertaken at the X-ray fluorescence microscopy beamline of the Australian Synchrotron, Victoria, Australia.

Chapter 3

3 Pacific and Atlantic controls on the relationship between Mainland Southeast Asia and East China interannual precipitation variability

3.1. Overview

The Asian monsoon region is highly dependent on boreal summer rainfall, which directly impacts the socio-economic stability and welfare of billions of people each year. Precipitation variability over East China has been extensively studied and is characterized by meridional tripole and dipole precipitation structures. In contrast, few studies have focused on precipitation variability over Mainland Southeast Asia (MSEA) and the possible relationship with the variability over East China. Here we focus on how interannual precipitation variability across MSEA during 1983-2017 may be associated with the tripole or dipole patterns using an empirical orthogonal function (EOF) analysis. The first EOF shows a meridional tripole pattern in East China summer precipitation and an in-phase relationship between MSEA and South China. In contrast, the second EOF shows a meridional dipole pattern in East China precipitation and an out-of-phase relationship between MSEA and South China. We show that the first EOF mode is a delayed precipitation response to the El Niño-Southern Oscillation (ENSO), while the second EOF mode is a simultaneous precipitation response to the remote influence of the North Atlantic Oscillation (NAO). These results suggest that in-phase and out-of-phase variations in precipitation between MSEA and South China may be used to gauge the relative importance of local Pacific and remote Atlantic influences on climate across the AM region.

3.1. Introduction

Interannual precipitation variability across East China has been well-characterized by meridional dipole and tripole structures (Hsu and Liu 2003; Hsu et al. 2007; Han and Zhang 2009; Ye and Lu 2012). The tripole pattern illustrates a positive rainfall anomaly center along the Yangtze River region and negative anomaly centers to the north and south or vice versa (Hsu et al. 2007; Huang et al. 2012; Day et al. 2015). Conversely, the dipole rainfall pattern describes out-of-phase variations in precipitation between southeastern and northeastern China (Ding et al. 2008; Qian et al. 2014; Sun and Wang 2015).

The spatial heterogeneity in precipitation across East China occurs particularly during boreal summer due to the East Asian Summer Monsoon (EASM) (Ding et al. 2008). The EASM exhibits several meridional quasi-stationary stages during its seasonal evolution and distinct transitions of abrupt change (Ding and Chan 2005). The differential heating between the Asian continent and the Pacific Ocean induces a low-level pressure contrast, which causes low-level monsoon flow from the South China Sea to East Asia (Sui et al. 2013). Sea surface temperature (SST) variations in the tropical Pacific and Indian Oceans related to the El Niño-Southern Oscillation (ENSO) exert significant influence on the EASM (Wang et al. 2000; Wu et al. 2003, 2009; Hsu et al. 2007; Feng et al. 2011). Following an El Niño event, cooling over the western Pacific can induce an anticyclonic circulation anomaly through a Gill-Matsuno type response, which can sustain this anomaly to the following summer through local air-sea interactions (Wang et al. 2000). The positive southeasterly wind anomaly on the west side of this anomalous anticyclone can strengthen the EASM and impact precipitation over East China (Wang et al. 2000; Wu et al. 2003). Other studies have suggested that ENSO can also strengthen the EASM through anomalous warming of Indian Ocean SSTs (Xie et al. 2009, 2016), which can trigger a

low-level anticyclonic circulation anomaly in the western north Pacific (Du et al. 2009; Xie et al. 2016). Shifts in the strength or zonal extensions of the Western Pacific Subtropical High (WPSH) (Sui et al. 2007; Wu and Zhou 2008) can also impact summer rainfall patterns over East China (Gong and Ho 2002). During periods when the WPSH intensifies, shifts southward, or extends westward, above-normal precipitation is expected along the Yangtze river valley and northward into southern Japan (Mao et al. 2010). These WPSH variations can be driven by SST anomalies over the western tropical Pacific (Sui et al. 2007; He et al. 2015) or the equatorial central Pacific (Wang et al. 2013; He et al. 2015), both of which are linked to ENSO.

In addition to ENSO impacts on East Asian summer precipitation, the remote influence of the North Atlantic Oscillation (NAO) in the preceding winter and spring on the Asian monsoon via modifications in the strength and location of the 200-hPa jet stream has been widely documented in studies (Yang et al. 2004; Sung et al. 2006; Zuo et al. 2012). However, recent studies have demonstrated the impact of the concurrent summer NAO (SNAO) on East Asian precipitation patterns (Sun et al. 2008; Folland et al. 2009; Linderholm et al. 2011, 2013; Wang et al. 2018). Linderholm et al. (2011) proposed that North Atlantic storm tracks and transient eddy activity associated with the SNAO led to the observed significant positive (negative) correlations with rainfall over southeastern China (central East China). Furthermore, thermal forcing over the Tibetan Plateau may provide an intermediate bridge effect in this teleconnection that leads to the dipole pattern in East China summer rainfall. Negative SNAO events have been associated with decreased precipitation over southeastern China and wet conditions along the Yangtze River basin and vice versa leading to this Eurasian teleconnection between the SNAO and EASM (Wang et al. 2018).

Despite the current literature on the leading modes of interannual to interdecadal precipitation variability in East China (He et al. 2017; Qiu and Zhou 2019), we stress that few studies have considered precipitation variability over Mainland Southeast Asia (MSEA) in relation to East China precipitation. Spatial patterns of precipitation vary greatly across the broad Asian Monsoon region and MSEA is geographically-situated at the boundaries among several distinct regional systems (including the EASM and the Indian Summer Monsoon (ISM)), such that MSEA precipitation patterns may be influenced by the complex dynamic interactions among these systems (Wang et al. 2002). Similar to the reliance in China, the economies of MSEA countries largely depend on the success of the entire agricultural sector, including farming, forestry, and fishing (Mekong River Commision 2005). Therefore, variations in summer rainfall can play a significant role in millions of lives. While a number of studies have focused on MSEA interannual precipitation variability (Misra and DiNapoli 2014; Mie et al. 2015; Tsai et al. 2015; Shrivastava et al. 2017; Ratna et al. 2017), none have investigated how MSEA precipitation patterns may be linked to the observed dipole or tripole precipitation patterns in East China or the dynamic mechanisms responsible for the potential linkage.

The motivation for this work stems from not only including MSEA in the analysis of the relationship between precipitation variability and climate phenomena (e.g., ENSO), but also the potential implications for paleoclimate studies and climate projections. Proxy evidence obtained from climate archives, such as speleothems, tree rings, and lakes, has been widely utilized to extend the record of EASM precipitation variability beyond the instrumental record, and increasingly suggests significant regional variability in the precipitation response to external forcing and internal climate variations. For instance, a synthesis of high-resolution paleoclimate records interpreted as moisture or precipitation variability from the EASM region revealed

spatially distinct precipitation variations (Chen et al. 2015, 2019a) over the last millennium. On centennial timescales, studies have shown various periods during which there were generally drier conditions in southern China, while the northern part was wetter (Chen et al. 2015). This spatial pattern of "south flood-north drought" observed since the late 1970s (Gong and Ho 2002; Ding et al. 2008) has also been observed in historical documents and speleothem records from eastern China (Wang et al. 2001a). Increasingly, multi-proxy paleoclimate evidence suggests that Asian monsoon precipitation also did not respond uniformly to past changes in insolation or Atlantic Meridional Overturning Circulation (AMOC) (Chiang et al. 2015; Zhang et al. 2018b; Huang et al. 2018), signifying that the dipole and/or tripole rainfall patterns may persist across a wide range of timescales. Despite efforts to synthesize multi-proxy records from across East Asia, there are few high-resolution proxy records from MSEA, limiting our understanding of past rainfall patterns (Buckley et al. 2010; Chawchai et al. 2015; Yamoah et al. 2016b; Wang et al. 2019). Given the heterogeneous nature of precipitation response to both external forcings and internal climate variability, further analyses of spatial and temporal precipitation variability and the underlying mechanisms in both modern and paleo-data are necessary for improving our understanding of regional precipitation variability across the broad Asian Monsoon region.

The present study aims to investigate the interannual precipitation variability across East China and MSEA, with a focus on identifying how MSEA precipitation variations are linked to the observed East China interannual dipole and tripole precipitation patterns. The main goal of this study is to analyze the dynamical mechanisms that give rise to these spatial precipitation patterns between MSEA and East China and to examine the possible relations with atmospheric teleconnections. The implications for this work extend for both paleoclimate studies and precipitation projections for East China and MSEA. Climate change in response to increasing

greenhouse gases (IPCC 2013) have already influenced regions of MSEA, observed through extreme weather events, including droughts, floods, and tropical cyclones (Asian Development Bank. 2009). Direct impacts already observed include decline of agricultural yields in Thailand, Vietnam, and Indonesia, massive flooding in Vietnam, Indonesia, and Laos, landslides in the Philippines and droughts in many other parts of MSEA (Asian Development Bank. 2009). Therefore, an improved understanding of the coupling (or decoupling) of interannual precipitation patterns can aid in improving future projections of precipitation variability across the broader Asian Monsoon region where they continue to remain uncertain over the next century (Christensen et al. 2013).

3.2. Data and methods

This study uses the multi-satellite, high-resolution Precipitation Estimation from Remotely Sensed Information using Artificial Neural Networks-Climate Data Record (PERSIANN-CDR) precipitation product that provides daily precipitation estimates at 0.25° spatial resolution for the period from January 1983 to December 2017 (Ashouri et al. 2015). The primary source of precipitation data is collected from infrared (IR) satellite data of global geostationary satellites, and the model is pre-trained using the National Centers for Environmental prediction stage IV hourly precipitation data to meet calibration requirements. Model parameters are held fixed and the model is run using the historical record GridSat-B1 infrared data (Knapp 2008). Global Precipitation Climatology Project (GPCP) (Adler et al. 2003) monthly 2.5° spatial resolution product is then used to reduce biases in precipitation estimates. The dataset is available from: https://www.ncdc.noaa.gov/cdr. Here we focus on the seasonal

mean precipitation averaged in July and August over East China and MSEA (100-124°E and 8-45°N).

Additional datasets used in this study include the following: 1) monthly means reanalyses of zonal and meridional winds at 850-hPa, 200-hPa geopotential heights, vertical velocity (omega) and vertically-integrated zonal and meridional moisture flux and vertically-integrated moisture flux divergence at 0.75° x 0.75° spatial resolution from the European Centre for Medium-Range Weather Forecasts (ECMWF) reanalysis (ERA5) data; 2) the NOAA Extended Reconstructed SST data at 2.0° x 2.0° provided by the National Oceanic and Atmospheric Administration/National Climate Data Center (Huang et al. 2017). All the reanalysis datasets used in this study cover the same 35-year period as the PERSIANN-CDR precipitation dataset.

To identify the dominant modes of East China and MSEA summer precipitation variations, we apply an empirical orthogonal function (EOF) analysis on PERSIANN-CDR precipitation, averaged during the boreal summer months, over the region that is bounded by 100°- 124°E and 8°- 45°N. In order to capture both the observed meridional tripole pattern in East China based on previous studies (Chiang et al. 2015) and the precipitation variability over MSEA, it was necessary to exclude the western coastal portion of MSEA (e.g., Myanmar and parts of Thailand). The region of MSEA that includes Laos, Vietnam, and Cambodia has particular paleoclimate significance due to the presence of several published paleoclimate records that span at least the last few hundred years and longer (Buckley et al. 2010; Xu et al. 2011; Sano et al. 2012; Wang et al. 2019). The PERSIANN-CDR dataset was selected over longer-term precipitation datasets because of the higher spatial resolution available. Following previous studies (Chiang et al. 2015; Day et al. 2015; Kong et al. 2017; Zhang et al. 2018b), boreal summer is defined as July and August (JA). This monthly averaged period best represents

the overlap of two intraseasonal stages of precipitation over East Asia that characterize the dominant mode of East Asia summer rainfall interannual variability (Chiang et al. 2015). In this study, the precipitation variability across East China and MSEA are decomposed into the spatial patterns of the two leading modes (EOF1 and EOF2, hereafter). The corresponding PCs (PC1 and PC2) represent their temporal variations.

Statistical significance of correlation coefficients and anomalies based on linear regression are determined by Student's *t* test at the 90% confidence interval. Anomalies are defined as the deviations from the seasonal mean after removing the linear trend. All the time series and data presented in this study are unfiltered and detrended.

3.3. Results

3.3.1. Leading Precipitation Modes and Associated Circulation Anomalies

The climatology of mean JA climate during the period 1983-2017 is characterized by prevailing westerly and southwesterly winds that transport warm, moist air from the Indian and tropical Pacific Oceans and cause heavy precipitation along the coastal regions of MSEA and the Philippines (Figure 3.1). Precipitation over MSEA is also somewhat influenced by local orographic effects, which can lead to heterogeneous rainfall patterns among neighboring countries (Chang et al. 2005; Wang et al. 2012b). Additionally, southerly winds from the South China Sea transport moisture-laden air into East China and towards the Yangtze River valley. The presence of a dominant anticyclonic wind pattern off East Asia is also shown in the JA climatology.

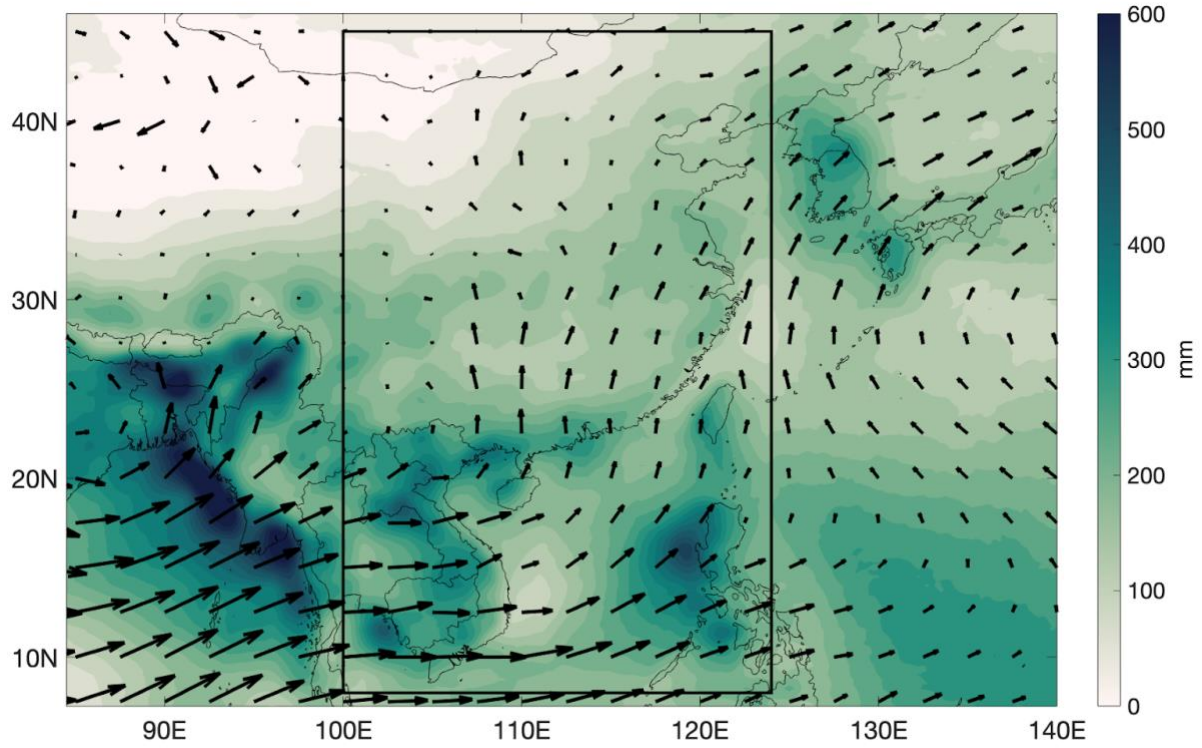

Figure 3.1. Summer (July-August) precipitation (shading, mm) and 850-hPa winds (vector, m s^{-1}) climatology derived from PERSIANN-CDR data (Ashouri et al. 2015) and ERA5 reanalysis dataset for the period 1983-2017. Wind vectors are scaled by a factor of 2.

We focus on the first two leading modes from the EOF analysis to examine the interannual precipitation variability across East China and MSEA. These two EOF modes are distinguished from the rest of the EOF modes based on their eigenvalues (not shown) and together explain 36% of the precipitation variability in the study region (denoted by the black box in Figure 3.1). The first EOF mode (EOF1; accounting for 23% variance) clearly illustrates a meridional tripole pattern. Positive loading values are centered just north of the Yangtze River region and negative loading values are present to the north and south (Figure 3.2a). This meridional tripole pattern over East China is broadly consistent with other studies, though these studies have referred to this first EOF mode as the dipole mode (Han and Zhang 2009). The time series of PC1 exhibits interannual and interdecadal variability (Figure 3.2b). In addition to the

meridional tripole pattern observed in the EOF1, we distinguish that precipitation variations in MSEA are broadly in-phase with those over South China, which we describe as the region just northwest of the Pearl River Valley region.

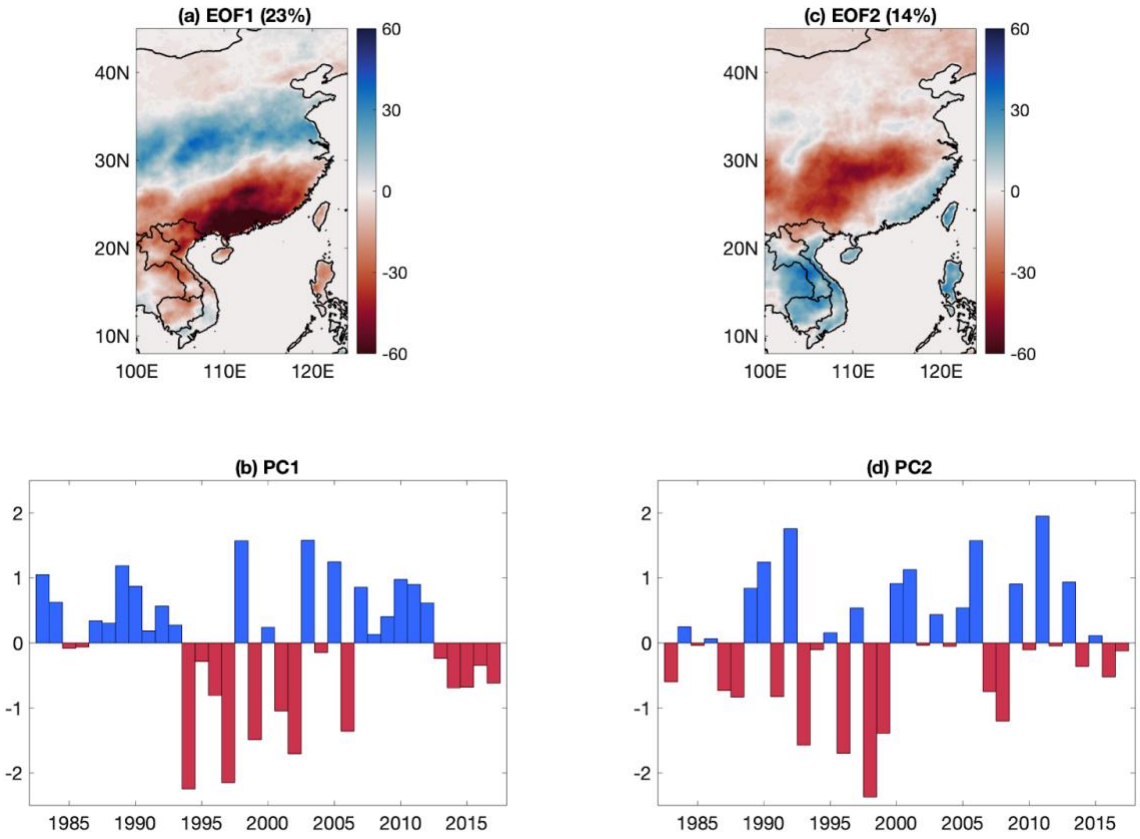

Figure 3.2. Spatial patterns of the (a) first and (b) second EOF modes of JA precipitation and the respective principal components (c) PC1 and (d) PC2.

The second EOF mode (EOF2; accounting for 14% variance) mostly describes the relatively uniform negative loading pattern across East China, which is contrasted by a positive loading region extending from coastal southeastern China to MSEA (Figure 3.2c). Unlike the EOF1 mode, the EOF2 mode is distinguished by out-of-phase precipitation variations between MSEA and most of south China (excluding the coastal regions). These analyses confirm that the

EOF1 and EOF2 patterns represent two different relationships between MSEA and East China (particularly the South China) precipitation variability.

To investigate the dynamic mechanisms associated with these two EOF modes, we first regress precipitation and 850-hPa wind anomalies onto PC1 across the broad Asian monsoon region (Figure 3.3). The tripole pattern revealed in EOF1 is consistent with a rainbelt centered just north of the Yangtze River region and reduced rainfall to its north and south. The regression of 850-hPa winds reveals an anomalous low-level anticyclone centered around 20°N and 115°E, suggesting a strengthening and westward extension of a western Pacific anomalous anti-cyclone. (Figure 3a). Dynamically, the anomalous anticyclone can induce descending motion and contribute to the drier conditions over both South China and MSEA regions.

Additionally, water vapor transport and supply play important roles in this precipitation pattern. The regression of vertically-integrated moisture flux onto PC1 shows near-identical circulation patterns as the regression of 850-hPa winds onto PC1 (Figure 3.3b). The anomalous anticyclone induces divergent water vapor flux out of MSEA and South China, while there is convergent motion north of Yangtze River region. The easterly anomalies to the south of 20°N transport moisture out of MSEA and towards the Bay of Bengal and Indian Ocean, which can contribute to the decreased precipitation pattern observed over MSEA. These patterns of moisture transport support the physical representation of the tripole pattern observed in the EOF1 pattern and the in-phase precipitation variations between South China and MSEA. These results indicate that the strengthening and westward extension of an anomalous anti-cyclone can be a key contributor to the first mode of precipitation variability and the in-phase relationship between MSEA and South China precipitation.

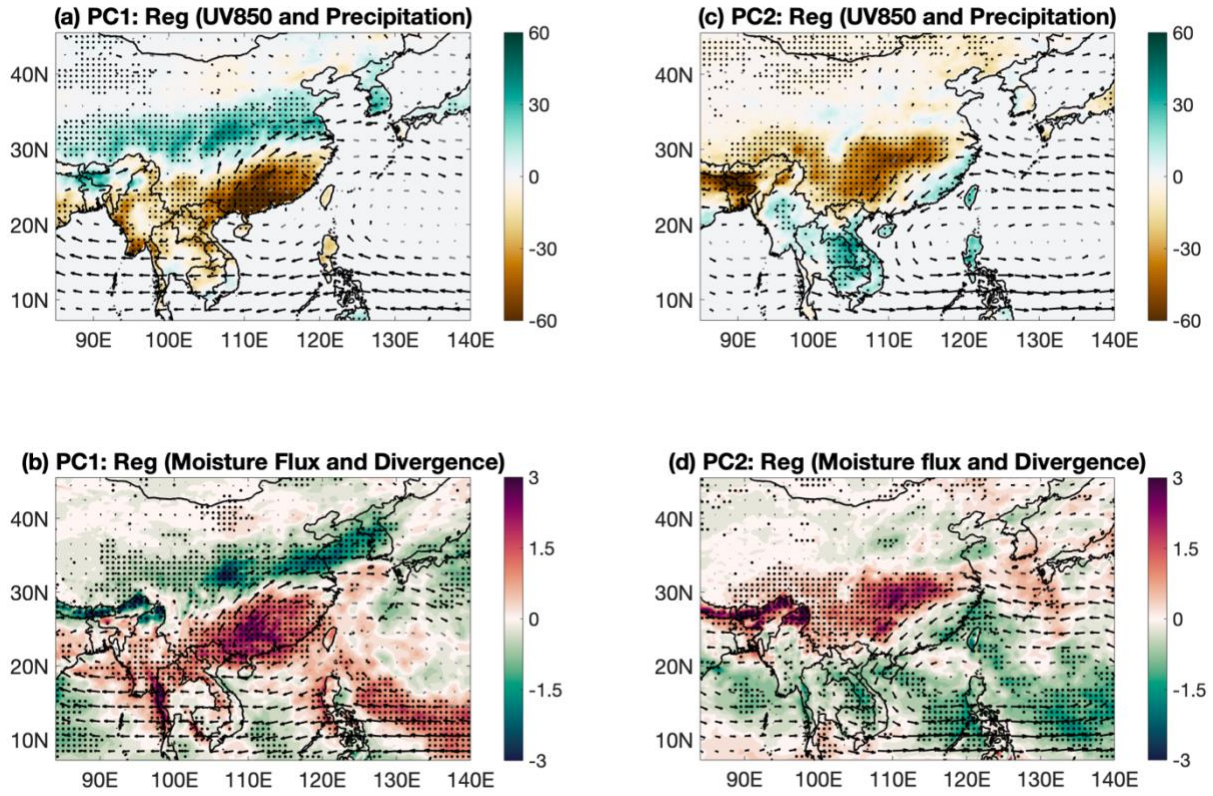

Figure 3.3. The regression maps of JA precipitation (mm) and 850-hPa winds (m s^{-1}) onto (a) PC1 and (c) PC2 for 1983-2017. The linear regression of the vertical integral of water vapor transport (vectors, kg (m s)$^{-1}$) and vertically integrated moisture divergence (shading, kg m^{-2}) onto (b) PC1 and (d) PC2 shows similar patterns. The black vectors and black stippled regions in a-d denote significance at the 90% confidence level.

We repeat the same analyses for PC2 and compare how anomalous wind and moisture circulation patterns impact the observed dipole pattern in EOF2. The regression of 850-hPa wind anomalies onto PC2 is characterized by anomalous easterly winds centered around 30°N and is accompanied by anomalous cyclonic circulation to the south and anomalous anticyclonic circulation to the north (Figure 3.3c). The anomalous anticyclone centered around Japan is weaker and the vectors are not all statistically significant at the 90% confidence level. However, the significant, stronger anomalous cyclone extends from the coast of South China on the western edge to the central western Pacific on the eastern edge (Figure 3.3c). The regressions of

moisture transport and divergence show water vapor transport and convergence over the Philippine Sea, South China coast, and MSEA, whereas anomalous moisture divergence and moisture flux from the western Pacific contributes to the observed decreased precipitation over South China (Figure 3.3d).

These results indicate that the influence of an anomalous anti-cyclone plays an important role in both the meteorological and water budget aspects of the EOF1 pattern, such that dry conditions persist in both South China and MSEA. However, the anomalous easterly flow associated with the EOF2 pattern produces drying in south-central China, but the cyclonic circulation anomaly to the south over the South China Sea produces wet anomalies over MSEA. In the next section, we investigate potential mechanisms that may have produced these anomalous circulation centers and subsequently anomalous precipitation patterns.

3.3.2. Surface to Upper-Troposphere Patterns

We analyze the 200-hPa geopotential height (Z200) anomalies to determine whether the observed precipitation patterns are linked to perturbations in the upper troposphere (e.g., the Asian westerly jet stream or barotropic wave trains). To highlight the wave components of upper-air structure, zonal means are subtracted from the anomalies prior to the regression analysis. The regression onto PC1 shows a positive Z200 anomaly over South China and a negative Z200 anomaly north of the Yangtze River valley (Figure 3.4a). These two anomalies lead to anomalous descending motions over South China and MSEA and ascending motions over North China, respectively, and contribute to the tripole precipitation pattern of EOF1. Figure 3.4b shows the vertical cross sections of the regression of omega velocity anomalies onto PC1. The zonal averages in these plots were taken over the longitudinal region of 100° to 124°E (box

in Figure 3.1). Anomalous ascending motion is clearly shown to occur north of ~30°N where the negative Z200 anomaly is located, while anomalous descending motion is present over the region between 15°N to 30°N where the positive Z200 anomaly appears (Figure 3.4b). These latitudinal rain bands correspond to the respective loading patterns and precipitation anomalies associated with EOF1 (see Figure 3.2a), which suggest that the Z200-induced descending motion also contribute to the in-phase precipitation variations between MSEA and South China. Figure 4a shows that these two Z200 anomaly centers may be associated with that of a wave train-like pattern, which originates around the northern flank of the Tibetan Plateau. Taken together, variations in the low-level anticyclone may affect the water vapor transport, whereas the wave train in the upper atmosphere may lead to anomalous descending and ascending motion that could contribute to the EOF1 pattern of precipitation variability.

The Z200 regression onto PC2 is dominated by a zonal wave train pattern that extends from the tropical Atlantic to the western Pacific via Eurasia (Figure 3.4c). Over East Asia, the regression pattern is characterized by an anomalous cyclone over North China and an anomalous anticyclone off the coast of Central China. This anomaly is right above the 850hPa anticyclonic wind anomalies over Central and South China (see Figure 3.3c). Therefore, the surface circulation anomalies associated with EOF2 are observed in both the lower to upper atmospheres, which suggests the barotropic circulation anomalies associated with a zonally-extended wave train from the Atlantic produce the out-of-phase precipitation pattern between South China and MSEA. This wave train weakens the band of zonal winds centered at 30°N and off East China (see Figure 3.3c and 3.4c), which can then induce anomalous ascending to the south and anomalous ascending to the north due to geostrophic adjustments. The anomalous vertical motions are confirmed by Figure 4d where vertical velocity (omega) anomalies are

regressed onto PC2. Anomalous ascending motion is positioned between ~10°-20°N (i.e., over the MSEA region), whereas descending motion is centered between 25°-30°N (Figure 3.4d). Therefore, the zonally-extended wave train in the upper troposphere induces surface anomalous circulation, affecting moisture transport and anomalous vertical motions, to give rise to the EOF2 precipitation pattern and the out-of-phase relationship between MSEA and South China.

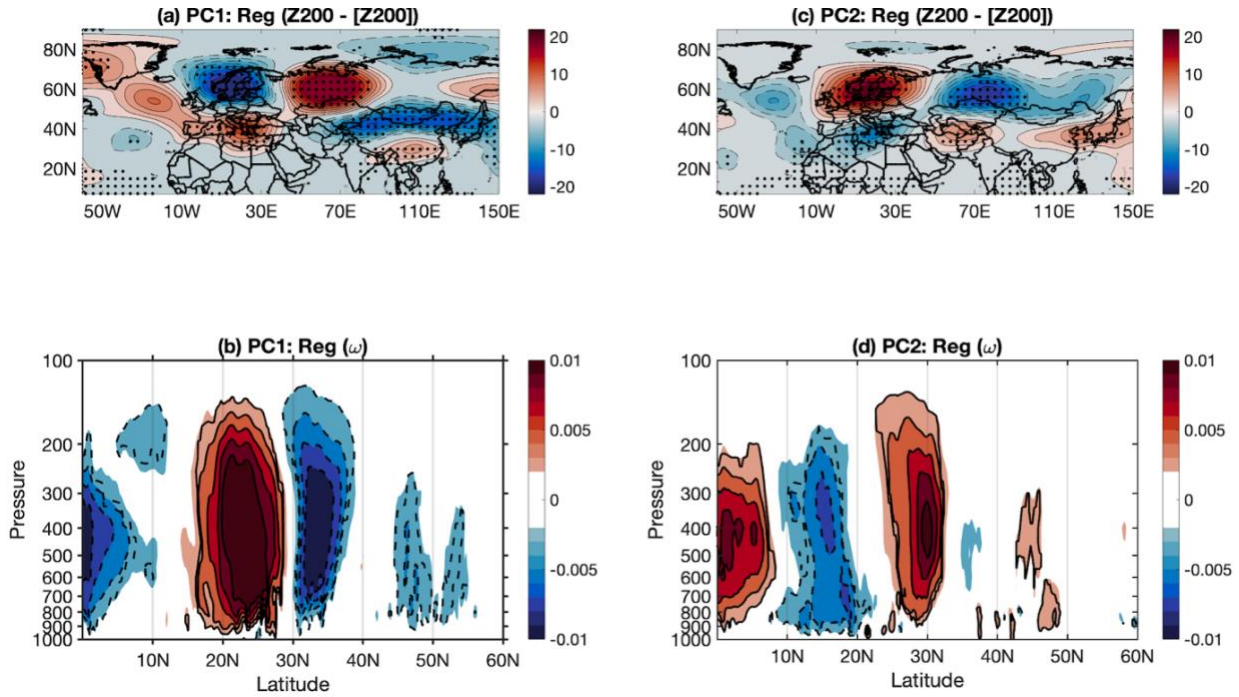

Figure 3.4. The regression maps of Z200 minus the zonal mean and vertical velocity (Pa s^{-1}) onto (a,b) PC1 and (c,d) PC2, respectively. The solid (dashed) contours present positive (negative) values. The black stippled regions in (a,c) and the black contours in (b,d) denote significance at the 90% confidence level.

3.3.3. Linked Teleconnections with Precipitation Modes

The tripole precipitation pattern in EOF1 is indicative that the anomalous anti-cyclone in the western Pacific is an important circulation system of precipitation in East China and MSEA. We further explore whether ENSO plays a key role in precipitation variability across South China through its delayed impacts on the WPSH as observed in previous studies (Wang et al.

2000; Xie et al. 2009). The correlation coefficient between PC1 and previous December-January-February (DJF) Niño3.4 index, which is defined as the average SST anomaly over 5°S-5°N 170°-120°W, is calculated as $r = 0.29$ and is statistically significant at the 90% level. The year-to-year comparison between the Niño3.4 index and the PC1 shows coherence in which the preceding winter eastern tropical SSTs align with shifts in the PC1, though some significant ENSO events including the 2015-2016 event do not appear as a large shift in the PC1 (not shown).

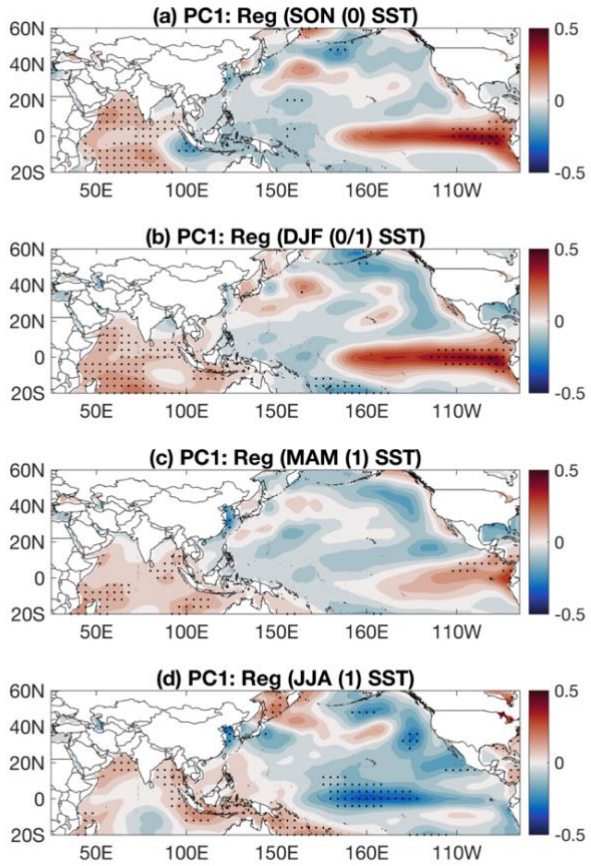

Figure 3.5. The regression maps of SST in (a) SON (0), (b) DJF (0/1), (c) MAM (1), and (d) JJA (1) onto PC1. The black stippled regions denote significance at the 90% confidence level. The value 0 represents the previous year and the value 1 represents the concurrent year.

To examine the possible connection between ENSO and the EOF1 mode, we regress SST anomalies onto PC1 from the preceding autumn to the concurrent summer of the EOF analysis. In the preceding autumn (Figure 3.5a), positive SST anomalies over the tropical eastern Pacific indicate developing El Niño conditions. The typical Indian Ocean warming induced by the developing El Niño is also evident in the regression pattern. Atmospheric teleconnections and ocean dynamics associated with El Niño induce a basin-wide surface warming over the tropical Indian Ocean (Nigam and Shen 1993; Masumoto and Meyers 1998; Klein et al. 1999; Lau and Nath 2000; Xie et al. 2002; Yang et al. 2007). Meanwhile, negative SST anomalies are present over the western tropical Pacific. The warm SST anomalies expand westward towards the tropical central Pacific by winter (Figure 3.5b). In the following spring (Figure 3.5c), SST anomalies decrease in the tropical eastern Pacific as the El Niño decays. The positive SST anomalies induced by the El Niño-like conditions are still present in the tropical Indian Ocean and act as a capacitor to produce delayed impacts on the atmosphere over the western North Pacific (Lau et al. 2003; Xie et al. 2009; Du et al. 2009; Wu et al. 2010).

The developing El Niño should also excite an anomalous anticyclonic circulation over the western North Pacific (Wang et al. 2000) through a Gill-type response, which can also be maintained through local atmosphere-ocean coupling during the decaying summer. A weakened Walker circulation initiated by the El Niño-like conditions induces anomalous divergence and downward motion over the Maritime continent and an anticyclone over the Philippines also prolongs the impact of ENSO (Wang et al. 2000). Through these three mechanisms, the preceding El Niño event can produce a delayed intensification impact on the WPSH in the following summer (Chen et al. 2019b). Finally, in the concurrent summer, the central tropical Pacific SST anomalies transition to negative anomalies (Figure 3.5d). The regression shown in

Figure 3.5 confirms that the EOF1 mode of precipitation variability is linked to an ENSO forcing, which results in in-phase precipitation variations between MSEA and South China precipitation variations.

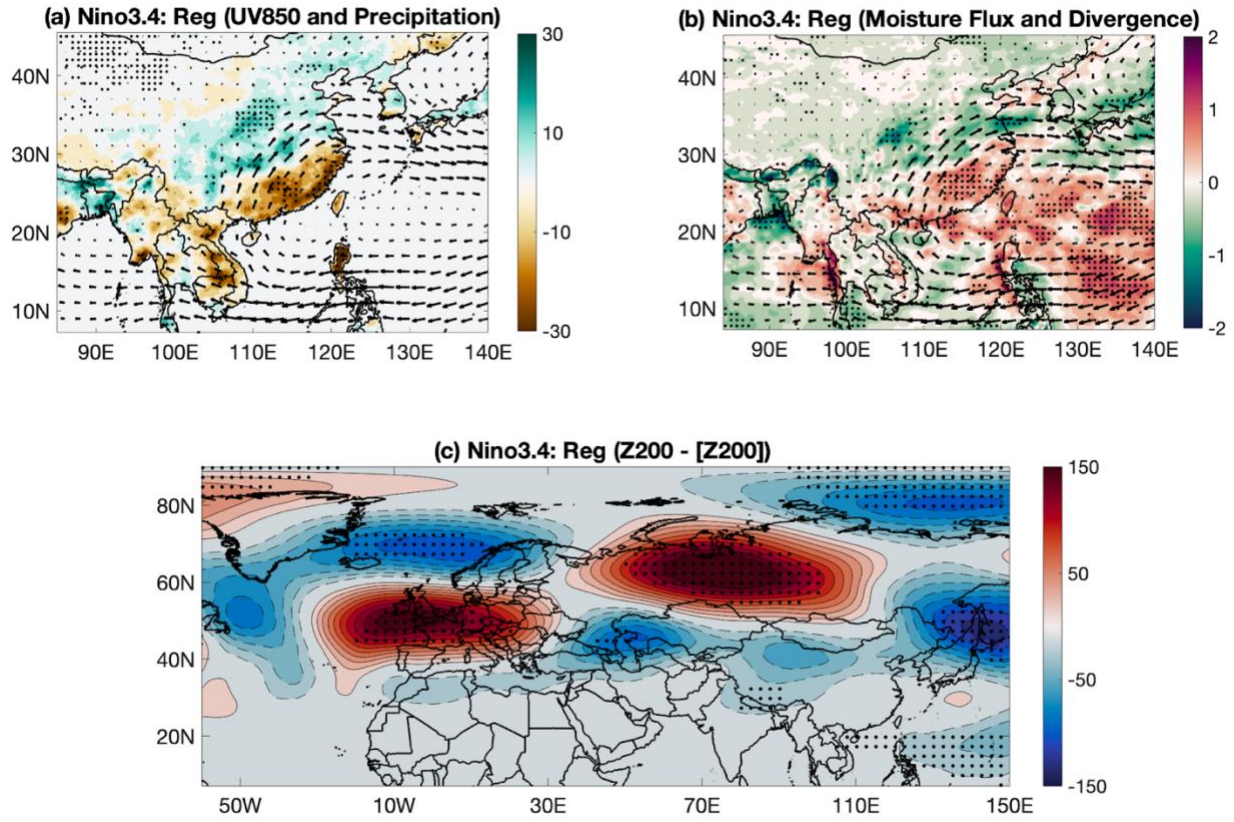

Figure 3.6. As in Fig. 3, but for the (a,b) regression maps onto DJF Niño3.4 index for 1983-2017. The regression map of Z200 minus the zonal mean and vertical velocity (Pa s^{-1}) onto (c) DJF Niño3.4 index also shown. The black vectors in (a,b) and black stippled regions in a-c denote significance at the 90% confidence level. The solid (dashed) contours present positive (negative) values.

We repeat the regression analysis that we conducted onto PC1, but onto the DJF Niño3.4 index. Near-identical circulation anomalies are present in the regression maps. There is the presence of an anomalous anti-cyclone at 850hPa (Figure 3.6a), the associated moisture fluxes that diverge out of MSEA and South China and converge into Yangtze River region (Figure

3.6b), and a wave train at 200-hPa emanating from the northern flank of Tibetan Plateau toward South China (Figure 3.6c). Given these similar circulation anomalies and patterns, the regression of precipitation does show the in-phase precipitation variations between South China and MSEA (Figure 3.6a). Lastly, we examined precipitation anomalies in JA following all major El Niño and La Niña events since 1982. Here, El Niño (La Niña) events were selected based on NOAA's criterion that the Ocean Niño Index (ONI) be greater or equal to (less than or equal to) 0.5ºC for a period of at least five, consecutive and overlapping three-month seasons. Five El Niño events (1982, 1987, 1991, 1997, and 2015) were classified as either strong or very strong, with a 3-month Niño 3.4 average greater than 1.50 and 2.0, respectively (Figure 7a).

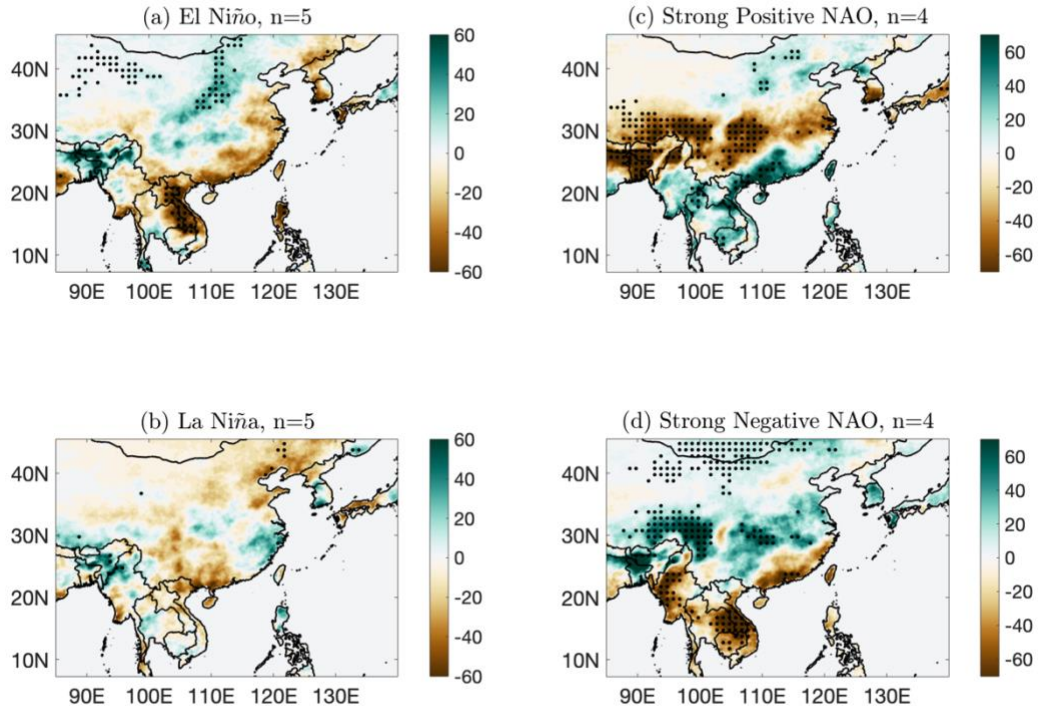

Figure 3.7. Composite precipitation anomalies (mm) for (a) strong/very strong El Niño events (b) strong La Niña events and strong (c) positive and (d) negative NAO events. The black stippled regions represent significance at 90% confidence level. The n values present the number of years that are composited in each panel.

The analyzed La Niña years were the following: 1988, 1998, 1999, 2007, and 2010. Qualitatively speaking, the composites of these events suggest that El Niño likely plays a role in producing the meridional precipitation pattern and the in-phase relationship between South China and MSEA, as noted in previous studies (Jin et al. 2016). However, precipitation anomalies during La Niña events do not appear to be robust (Figure 7b). Possible explanations may be that (i) La Niña events are typically weaker than El Niño events due to nonlinear dynamic processes (Burgers and Stephenson 1999), (ii) interdecadal modulations of La Niña events in response to Pacific climate shifts over the last several decades may have muddled the precipitation signals (Wang et al. 2012a), or (iii) a combination of others factors influencing East China and MSEA precipitation as well as ENSO, such as Indian Ocean (Watanabe and Jun, 2002) or North Atlantic SSTs (Wang et al. 2011).

We then evaluated the dynamic mechanisms influencing the EOF2 mode of precipitation variability and the out-of-phase variations between South China and MSEA precipitation. As previously mentioned, upper-tropospheric anomalies are dominated by a zonally-extended wave train structure that originates from the North Atlantic Ocean and extends towards the Japan Sea. We explore the possible relationship between EOF2 and the NAO, which is the leading variability mode in the atmosphere over the North Atlantic (Hurrell 1995). We find the highest correlation between PC2 and the average of May-June-July (MJJ) values of the NAO index from the Climate Prediction Center with a correlation coefficient of $r = 0.43$ that is statistically significance at 99% confidence level. Previous studies have found that the EASM and the preceding spring (April-May) NAO are well-correlated. Gu et al. (2009) showed that the March NAO is closely related to a leading precipitation mode, which exhibits out-of-phase variation between the Yangtze river valley and southeast China. Although the EOF analysis did not

include MSEA, the spatial pattern in southeast China and the Yangtze River region is similar to the spatial pattern seen in EOF2 of our study (Figure 3.2b and their Figure 3.1b).

We repeat the regression analyses onto the NAO index as was done for PC2 to assess whether the MJJ NAO may induce similar anomalies. The regression maps of precipitation anomalies and low-level winds onto the NAO index show qualitatively similar results as the regression maps onto PC2 (Figure 8a). Some differences do exist, for example, the cyclonic circulation pattern centered over the South China Sea that likely induces more precipitation over South China compared to that of the regression map onto PC2 (Figure 3c). The low-level cyclonic pattern is mostly concentrated over the South China Sea (Figure 3.8a) as opposed to an elongated anticyclonic pattern (Figure 3.3c). However, the patterns of vertically-integrated moisture flux patterns, such as, the moisture divergence over parts of South China that extends into the Yangtze River region remain consistent (Figure 3.8b). The regression map onto Z200 also highlights the barotropic pattern observed in the regression map onto PC2 and supports the lower geopotential heights over MSEA and the wave train-like patterns that appear to originate from the North Atlantic through Eurasia and propagate southeastward into South China (Figure 3.8c). This wave train between the North Atlantic and East Asia has been observed in other studies (Bao-Qiang and Ke 2012). Lastly, we examined JA precipitation anomalies observed during all major NAO events since 1982. Here, the strong NAO events were selected based on years in the MJJ index that exceeded one standard deviation. We identified four strong positive NAO events (1992, 1994, 2008, 2013) and four strong negative NAO events (1993, 1998, 2008, 2012) events. By compositing the associated precipitation anomalies during these NAO years, it is clear that during strong NAO events, the precipitation anomalies resemble

the EOF2 pattern and South China and MSEA show an overall pattern of precipitation variations that are out-of-phase (Figures 3.7c and 3.7d).

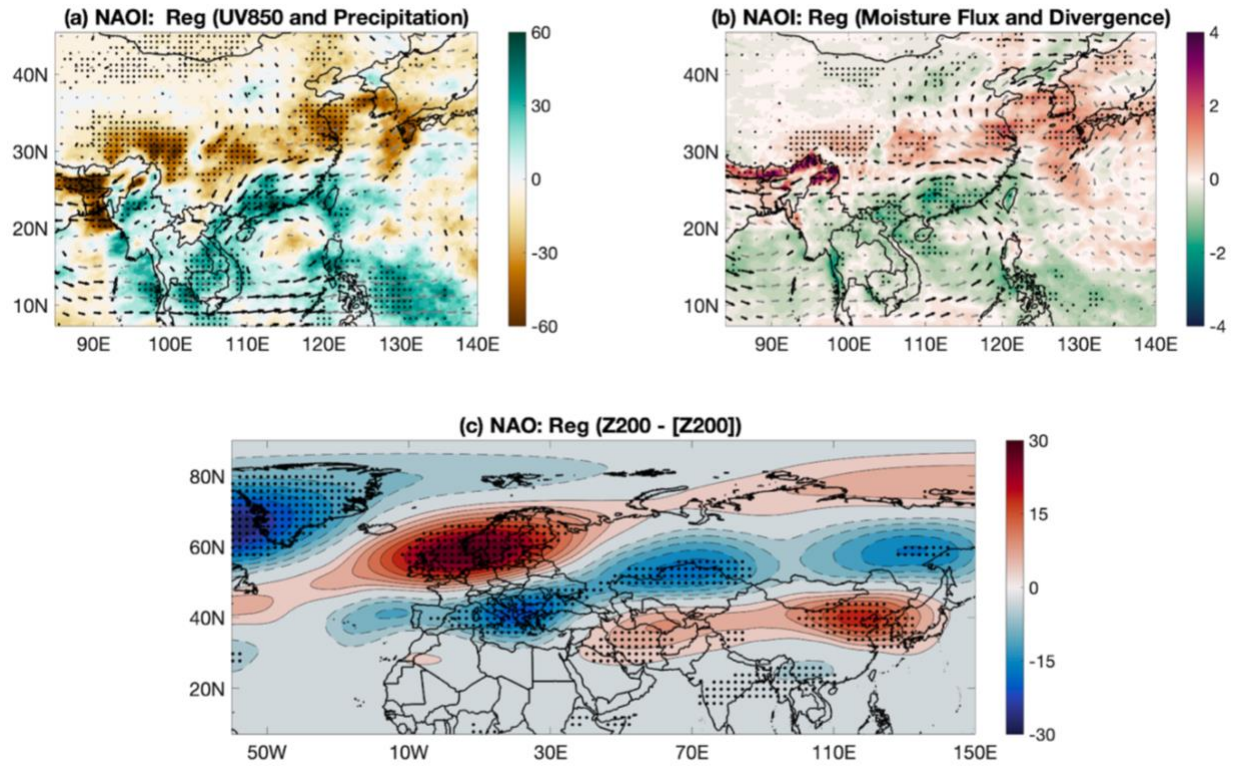

Figure 3.8. As in Fig. 6, but for the (a-c) regression maps onto MJJ NAO index for 1983-2017.

These analyses support our findings that the EOF1 and EOF2 modes of precipitation variability likely represent responses of East China and MSEA precipitation to ENSO and NAO forcings, respectively. We emphasize that the dominant precipitation patterns across East China vary between these two modes, but also the relationship between MSEA and South China also changes. We hypothesize that precipitation anomalies in these two regions should reflect an in-phase relationship during strong ENSO events and potential out-of-phase precipitation variations in response to a remote Atlantic forcing.

3.4. Conclusions

Precipitation across East China and MSEA is characterized by strong interannual variability. The features of the interannual variations of JA mean rainfall for East China and MSEA were assessed using satellite precipitation data. The spatial structure of summer rainfall over East China and MSEA were analyzed using the EOF method for the period of 1983-2017. Results showed that the leading mode of interannual precipitation variability over the last few decades is characterized by a meridional tripole pattern and in-phase precipitation variations between South China and MSEA. We conclude that this precipitation mode is likely driven by anomalous anti-cyclone variations over the western Pacific in response to ENSO. Conversely, the second leading mode of interannual precipitation variability is characterized by a meridional dipole pattern and an out-of-phase relation between South China and MSEA precipitation. This mode is primarily driven by a zonally-extend wave train from the North Atlantic sector and associated with the summer NAO. Therefore, the in-phase and out-of-phase relationship between MSEA and South China precipitation manifest the relative controls of the local Pacific ENSO forcing and the remote Atlantic NAO forcing.

This study discusses the interannual variability across East China and MSEA, but it should be mentioned here that precipitation over these regions experiences significant interdecadal variations as well (Huang et al. 2013; Sun and Wang 2015). Previous studies have revealed a variety of other factors contributing towards the interdecadal variability of East Asian climate, such as the Pacific Decadal Oscillation (Wang et al. 2008a; Feng et al. 2014). A 10-year high-pass Butterworth filter was initially applied to the PERSIANN-CDR precipitation dataset similar to the methods in other studies (Hsu et al. 2007; Jin et al. 2016; He et al. 2017). However, both the EOF modes and the regression analyses yielded similar results to the final results

presented here, highlighting a potential caveat of the PERSIANN-CDR dataset, which cannot capture the interdecadal variations due to the 35-yearlong dataset. Moreover, it will be intriguing to further analyze how the response from ENSO and/or NAO forcings on the relationships between South China and MSEA evolve in the future due to climate change. The present study focuses on a small set of strong ENSO and NAO events given the temporal limitation of the precipitation data set and calls for additional studies to evaluate how the ENSO and NAO remote forcings may influence the interdecadal precipitation variations between South China and MSEA.

In addition to investigating these relationships on interdecadal timescales, other studies have analyzed past changes in the EASM climate over glacial-interglacial timescales through paleoclimate proxy records and paleoclimate model simulations. These studies have found that meridional precipitation patterns in East China are present on longer timescales (Chiang et al. 2015; Kong et al. 2017; Zhang et al. 2018b), though the forcing is likely different than for the modern interannual variability. For instance, the tripole pattern of precipitation variability has been shown to be driven by the timing and duration of distinct stages of the EASM related to insolation-forced shifts in the position of the westerlies relative to the Tibetan Plateau (Kong et al. 2017) during the Holocene. While the present study does not find a strong argument towards a shift in the westerly jet in influencing East China precipitation patterns, it does provide additional insight on the mechanisms influencing precipitation variability in both East China and MSEA. Our findings can have significant implications for paleoclimate studies that utilize precipitation proxies from the Asian Monsoon region, specifically MSEA and South China (Wang et al. 2019) to infer the relative Pacific and Atlantic teleconnections on past East Asian climate. By identifying the dominant controls on interannual precipitation patterns across MSEA

and East China, our results can help improve paleoclimate proxy comparisons among sites situated within these two regions. While additional studies are needed to clarify whether the ENSO and NAO forcings on the relationships between South China and MSEA are stationary on longer timescales, our results combined with additional paleoclimate records from MSEA and South China can provide a more comprehensive and broad view of the EASM system during both the instrumental and paleoclimate periods. Future studies that combine climate proxies, observational data, and output from global circulation models are necessary to further investigate the spatial and temporal patterns of precipitation variability across East China and MSEA.

Acknowledgments

We thank Zachary M. Labe, Dillon J. Amaya, and Michael L. Griffiths for valuable discussions and suggestions. PERSIANN-CDR data were obtained from http://chrsdata.eng.uci.edu/. We acknowledge the ERA5 reanalysis data is from the Copernicus Climate Change Service (C3S) (2017): ERA5: Fifth generation of ECMWF atmospheric reanalysis of the global climate. The data were downloaded from Copernicus Climate Change Service Climate Data Store (CDS), March 2019. https://cds.climate.copernicus.eu/cdsapp#!/home. Monthly ONI data obtained by the NOAA/PSD through https://www.esrl.noaa.gov/psd/data/correlation/oni.data. *NOAA_ERSST_V5 data provided by the NOAA/OAR/ESRL PSD, Boulder, Colorado, USA, from their Web site at https://www.esrl.noaa.gov/psd/*. This work was supported by the National Science Foundation Graduate Research Fellowship Grant DGE-1321846 to J.K. Wang, National Science Foundation grants AGS-1505145 and AGS-1833075 to J.-Y. Yu, and NSF P2C2 award 1603056 to K.R. Johnson. The authors declare no competing financial interests.

Chapter 4

4 Distinguishing karst hydrology impacts from climate variability using an isotope-enabled forward model

4.1. Introduction

4.1.1. Identifying Climatic and Non-Climatic Controls on Stalagmite $\delta^{18}O$

Physical climate signals incorporated into climate archives, such as speleothems, can provide insights on past local to global changes on a variety of timescales. Speleothems are advantageous in studying past climate, since they are often well preserved in their respective environments, exhibit fast growth rates, and can be absolute-dated. Geochemical signals, such as the oxygen stable isotope composition ($\delta^{18}O$), are preserved within the calcite growth bands in speleothems. By evaluating past changes in speleothem $\delta^{18}O$ beyond the instrumental period (circa 1850), we can work towards improving our ability to constrain current climate models and improve projections of climate change. However, interpretations of speleothem $\delta^{18}O$ values are often complicated due to processes prior to and during calcite precipitation that may alter or distort the assumed climate signal recorded. Two specific factors include the non-linear nature of karst hydrology and in-cave isotopic fractionation (Hartmann and Baker 2017).

It is commonly assumed that speleothem $\delta^{18}O$ values reflect linear changes in the precipitation $\delta^{18}O$ that falls above the cave and directly travels through the karst system, which can be influenced by a number of factors, including rainfall amount and the moisture source region and transport (Dansgaard 1964; LeGrande and Schmidt 2009). However, cave monitoring efforts have highlighted the non-linear nature of karst hydrology that may complicate these

interpretations. These efforts include weekly to seasonal observations of cave conditions, drip water, and hydrology at different study sites (Spötl et al. 2005; Frisia et al. 2011; Baldini et al. 2012; Baker et al. 2014; Markowska et al. 2015; Duan et al. 2016). These studies have highlighted how variations in infiltrating recharge water, mixing of various water stores, and water movement can impact speleothem $\delta^{18}O$ signals (Ayalon et al. 1998; Mischel et al. 2015). These processes can be further influenced by a mixture of different flow pathways (e.g., fracture and diffuse flow) and soil and epikarst evapotranspiration (Cuthbert et al. 2014). Seasonal to interannual climate signals in speleothem $\delta^{18}O$ records may then be filtered out or "smoothed" (Baker and Bradley, 2010). Therefore, the preservation of crucial climate information from speleothems may be subjected to lags, seasonal biases, or enhancements of the isotopic signal (Ayalon et al. 1998; Baker et al. 2000; Tooth and Fairchild 2003).

Understanding $\delta^{18}O$ fractionation processes during formation also poses difficulty in interpreting speleothem records, given the complex interplay among processes in the soil, epikarst, and inside the cave (Deininger and Scholz 2019). Calcite precipitation under conditions of isotopic equilibrium implies that precipitated calcite is in isotopic equilibrium with the water (Hendy 1971). However, in-cave conditions and processes may prevent isotopic equilibrium and have a significant impact on the temporal evolution of the speleothem $\delta^{18}O$ values through various fractionation processes. For example, evaporative fractionation of drip water $\delta^{18}O$ may occur in caves with low relative humidity and slow in-cave air transport or ventilation (Deininger et al. 2012). Additionally, rapid precipitation after CO_2 degassing due to supersaturation of the drip water relative to calcite (Mickler et al. 2006; Mühlinghaus et al. 2009; Deininger et al. 2012) or changes in the drip interval between two subsequent drops may also affect the degree of isotopic disequilibrium (Kaufmann 2003b; Mühlinghaus et al. 2007, 2009; Frisia et al. 2011;

Deininger et al. 2012; Riechelmann et al. 2013). Therefore, it is important to consider these effects of disequilibrium isotope fractionation processes, in addition to changes in the karst hydrology, to improve our quantitative understanding of speleothem $\delta^{18}O$ climate signals and the influence of climate and environmental factors on these variations.

4.1.2. Proxy System Models

Proxy system models (hereafter referred to as PSMs) have introduced a novel application for quantifying the physical, chemical, or biological understanding of how an environmental signal is preserved in a climate archive (Evans et al. 2013). These forward models can integrate output from climate model simulations and reanalysis data as input data to quantify the sensitivity of speleothem $\delta^{18}O$ values to various environmental processes impacting proxy interpretation (Evans et al. 2013; Wong and Breecker 2015). These approaches can progress our ability to distinguish the effects of climate variability versus hydrological processes by predicting the expected observations in actual paleoclimate observations, and thereby make more direct comparisons with published paleoclimate records (Evans et al. 2013). PSMs can be used to identify the specific environmental forcings that influence paleoclimate observations, for example, variations in precipitation, temperature, and/or atmospheric circulation (Dee et al. 2015). Thus, these results can help to accurately identify the magnitude of uncertainties in speleothem $\delta^{18}O$ interpretations.

PSMs have proven to be effective in paleoclimate reconstructions by improving signal interpretation in proxy records (Steinman et al. 2013) and assisting in constraining climate models (Dee et al. 2016). This enhanced ability to distinguish the impacts of climate variability versus non-climatic hydrological processes on speleothem $\delta^{18}O$ has been achieved using detailed

observations of precipitation, drip water, and modern speleothem $\delta_{18}O$ (Baker and Bradley 2010; Moerman et al. 2014). Furthermore, PSMs have allowed users to investigate the hydrological uncertainties in speleothem $\delta_{18}O$ due to disequilibrium fractionation processes of drip water $\delta_{18}O$ prior to calcite deposition. Yang (2016) quantified the range of possible $\delta_{18}O$ values due to non-climatic hydrologic variabilities over interannual to decadal timescales using a PSM known as the KarstFor model (Baker et al. 2010). Using existing model output from a spectrally-nudged isotope enable climate model, IsoGSM (Yoshimura et al. 2008) to drive KarstFor, the study analyzed the mean $\delta_{18}O$ discrepancy observed among four stalagmites records from the same cave in northern Laos. The simulated output $\delta_{18}O$ time series (also referred to as pseudoproxy time series) from KarstFor were influenced by varying parameters, including precipitation $\delta_{18}O$, evapotranspiration, and mixing of water through different pathways. The study concluded that the absolute magnitude of 1.2‰ observed among the stalagmites were likely due to hydrological variability within the same cave and highlighted how multiple stalagmite records from the same cave can exhibit different variations in $\delta_{18}O$ values depending on the hydrological pathways and mixing occurring prior to calcite precipitation (Yang 2016).

4.2. Karstolution Overview

Over the last few decades, the development of forward models with the purpose of identifying the contributions of climate, karst hydrology, and/or speleothem fractionation processes have steadily increased (Baker and Bradley 2010; Baker et al. 2013). However, as identified in Treble et al. (2019), several of these PSMs focus only on in-cave (Mühlinghaus et al. 2007, 2009; Deininger et al. 2012) or soil processes (Wackerbarth et al. 2010, 2012; Dreybrodt and Scholz 2011) and have simplified representations of karst processes. Other PSMs,

on the other hand, focus only on the karst processes and have a simplified representation of the in-cave processes (Truebe et al. 2010; Baker and Bradley 2010; Baker et al. 2013; Cuthbert et al. 2014; Dee et al. 2015). Since the development and improvements of these models, (Treble et al. 2019) presented the first integrated stalagmite $\delta_{18}O$ PSM called Karstolution, which integrates an existing karst hydrology model (KarstFor) with an in-cave fractionation PSM (ISOLUTION) (Deininger et al. 2012; Baker et al. 2013; Deininger and Scholz 2019).

Baker et al. (2013) presented a lumped parameter model, known as KarstFor, that was initially introduced by (Bradley et al. 2010) and improved over several adaptations (Baker and Bradley 2010; Treble et al. 2013). This model integrates soil evaporation, monthly precipitation, and overflow based on user-defined climate inputs into the model. Mixing and movement through the soil, and epikarst are considered and in-cave equilibrium isotope fractionation between water and calcite is assumed (Baker et al. 2013). This hydrological modeling approach has led to quantitative assessments of the relative importance of precipitation, temperature, and water balance.

While KarstFor models the complexities of karst hydrogeology, ISOLUTION, an in-cave fractionation PSM, focuses on the disequilibrium isotope fractionation processes during the formation of speleothems (Deininger et al. 2012; Deininger and Scholz 2019). This PSM calculates the $\delta_{18}O$ values of the calcite precipitated at the top of a stalagmite from drip water that is supersaturated with respect to calcite (Deininger and Scholz 2019). The solution is sourced via the water that drips from the cave ceiling and referred to as the cave drip water. ISOLUTION accounts for the isotope fractionation processes during the precipitation of calcite (referred to as the disequilibrium isotope fractionation), in response to, changes in cave temperature, cave air pCO_2, drip interval, and drip water pCO_2 (an equivalent for the drip water

Ca^{2+} concentration), relative humidity, and cave ventilation during speleothem growth (Deininger et al. 2012; Deininger and Scholz 2019). Currently, ISOLUTION is noted to be the most comprehensive model that estimates the effect of various cave parameters (e.g., in-cave evaporation and isotope fractionation) on speleothem calcite that may affect growth and the speleothem proxy signals (Treble et al. 2019).

By combining the KarstFor and ISOLUTION models together, Treble et al. (2019) presented Karstolution, which accounts for both karst and in-cave processes and comprehensively covers processes from above the cave surface down to stalagmite deposition. Karstolution is coded in Python and is publicly available on GitHub (https://github.com/swasc/karstolution). This integrated surface-to-stalagmite $\delta^{18}O$ PSM is based on a simplified representation of a karst system that is not derived from fundamental laws (Treble et al. 2019) (Figure 4.1). It is important to note that this first iteration of Karstolution is best suited for hypothesis testing given its limited model complexity, which creates difficulty in comparing model parameters with physical properties of the proxy systems and limits the direct comparison of modeled $\delta^{18}O$ output with an observed stalagmite $\delta^{18}O$ record (Treble et al. 2019).

A total of five "pseudoproxy" (i.e., modeled) time series are the outputs from Karstolution (identified as Stal1, Stal2, Stal3, Stal4, and Stal5), which represent five different stalagmites at a cave site and are influenced by a series of different configurations related to karst hydrologic pathways (Figure 4.1). Changes in Stal2 and Stal3 are mostly influenced by the incoming rainfall $\delta^{18}O$ that is mixed with the solution in Karst Store 2 and therefore retain the seasonality of rainfall $\delta^{18}O$ as opposed to the site-specific variations in karst hydrology and in-cave conditions. Therefore, stalagmites Stal2 and Stal3 are not illustrated in Figure 4.1 and will

not be a focus in this chapter. Stal1, Stal4, and Stal5, on the other hand, take into consideration both the karst hydrological pathways and the various cave parameters as described by ISOLUTION (Deininger and Scholz 2019) and are illustrated in the conceptual model.

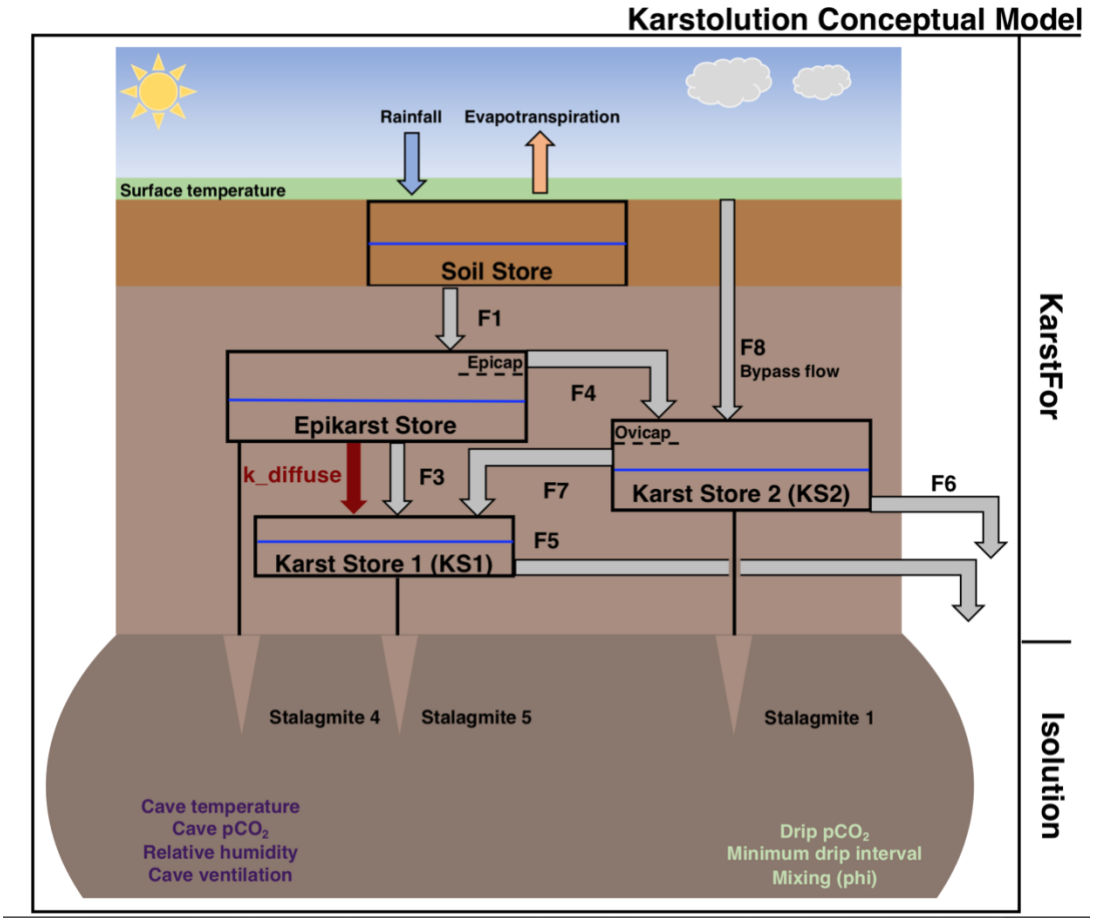

Figure 4.1. Conceptual diagram of the Karstolution model. The black boxes represent the various reservoirs, blue lines represent the initial water levels, grey arrows represent fracture flow, and the maroon arrow represents diffuse flow. Each of the stalagmite outputs (Stalagmite 1, Stalagmite 4, and Stalagmite 5) consider various cave parameters as described by ISOLUTION (Deininger and Scholz 2019). Stal2 is fed by drip water that is a mixture of Karst Store 1 and the incoming rainfall and Stal3 is fed by drip water that is mixed with Karst Store 1, incoming rainfall and the previous step of rainfall. Because these modeled stalagmites are less likely to be influenced by both karst hydrology and in-cave processes, these stalagmites are not illustrated in the diagram. See Table 4.1 for a summary of model inputs and user-defined parameters. Figure adapted from Treble et al. (2019).

The karst component of Karstolution mirrors the KarstFor version presented in (Baker et al. 2013), with four reservoirs (Soil Store, Epikarst, Karst Store 1 and Karst Store 2) at given initial values (mm), which are then recalculated starting with the Soil Store at a monthly time step (Figure 4.1). The $\delta_{18}O$ values in each store vary with each time step based on the water balance calculations. There are three stalagmite outputs (Stal1, Stal4, and Stal5) that are defined by different karst configurations, as modelled in (Baker et al. 2013). For each stalagmite output, the ISOLUTION aspect of Karstolution is applied to account for in-cave kinetic fractionation processes using both the cave parameter inputs and input reservoir water $\delta_{18}O$ to simulate the stalagmite $\delta_{18}O$ values.

In this chapter, I present a case study of Tham Doun Mai Cave (hereafter referred to as TM Cave) using monitoring data to configure the parameters in Karstolution. By comparing the various modeled stalagmite $\delta_{18}O$ time series, I can investigate the dependence of stalagmite $\delta_{18}O$ on one or more cave specific parameters and/or karst hydrological processes. The objectives of this chapter include the following: (i) demonstrate how Karstolution can be used to evaluate how changes in modeled stalagmite $\delta_{18}O$ may be influenced by the relative effects of climatic, karst, and in-cave fractionation processes, (ii) quantify the contributions of hydroclimatic processes versus in-cave processes on the variability of simulated stalagmite $\delta_{18}O$ values, and finally (iii) investigate the processes that may drive the observed lags among stalagmites and other climate archive records.

Table 4.1. Selected model parameter values and corresponding descriptions. All parameter names are from the conceptual figure in Figure 4.1. Table adapted from Treble et al. (2019) and Deininger and Scholz (2019).

Parameter	**Description**	**Final Configuration**
Soil store (mm)	Initial storage volume in the soil store	Initial: 50 Max: 150

Epikarst (mm)	Receives drainage from Soil Store via F1	Initial: 100 Max: 350 Epicap: 150
Karst store 1 (mm)	Primary store that receives drainage from Epikarst via k_diffuse and/or F3; may also receive overflow from KS2 via F7	Initial: 50 Max: 850
Karst store 2 (mm)	Secondary karst store via F4 and drains via F6 or switchable overflow to KS1 via F7	Initial: 10 Max: 80 Ovicap: 20
F1 (mm/month)	Soil Store to Epikarst	0.2
F3 (mm/month)	Fracture flux from Epikarst to KS1; can be set to 0 if flow is dominated by diffuse flow	0.001
F4 (mm/month)	Epikarst to KS2 activated when threshold 'Epicap' is reached	.2
F5 (mm/month)	Drainage flux of KS1 to Stal5	.02
F6 (mm/month)	Drainage flux of kS2 to Stal1	.08
F7 (mm/month)	Overflow KS2 back to KS1 when 'Ovicap' is exceeded	1
k_diffuse (mm/month)	Flux via PDF function to simulate diffuse flow	0.01
Phi (ϕ)	Mixing parameter of drip water with the water layer on the stalagmite surface. ϕ=1 implies limited splashing on the top of the stalagmite.	1
k_eevap	Epikarst evaporation (function of ET for timestep)	0
k_δ^{18}O_soil	Soil evaporation δ^{18}O fractionation	0.03
k_δ^{18}O_epi	Epikarst evaporation δ^{18}O fractionation	0

4.3. Site Description

The landlocked country of Laos is characterized by rugged mountains and rolling hills. The Annamite Range extends through the northeastern and eastern region of Laos and runs parallel to Vietnam's coast, while the Luang Prabang Range straddles northwestern Laos and northern Thailand. Laos experiences a tropical monsoon climate and receives more than two-

thirds of annual precipitation from the Southeast Asian Monsoon (SEAM) during May-September (Lau and Yang 1997). The onset of the SEAM occurs in late boreal spring and is characterized by a seasonal shift of winds from northeasterly to southwesterly (Misra and DiNapoli 2014). Warm, moist air from the Indian Ocean and the Bay of Bengal flows towards Laos during the monsoon season with additional moisture from the Andaman Sea and Gulfs of Martaban and Thailand (Misra and DiNapoli 2014).

Our study site, TM Cave, is situated adjacent to the Nam Ou River in Luang Prabang Province, Laos (N20°45', E102°39'; 352 m above sea level; Figure 4.2). The cave is formed in a Late Paleozoic limestone karst massif that rises several hundred meters above river level. Dense, tropical vegetation expands from the river bank towards the cave entrance (~30 m above river level) and continues up a steep, rocky slope of the karst tower above. The terrain above the cave is rocky and densely vegetated, with a patchy and thin soil cover (up to ~60 cm deep). TM Cave is approximately 3.75 km long. The first several hundred meters of the cave is situated above an active river passage, followed by a steep drop off down to the river level, and the cave continues up and downstream. The thickness of the overlying bedrock varies from a few meters close to the entrance of the cave and up to hundreds of meters in the deepest sections. The sample locations for cave monitoring measurements are beneath at least 100 m of bedrock, though the steep karst tower could make the overburden even higher above the sampling locations, since some parts of the cave are under as much as 400 m of bedrock. The main part of the cave is separate from a smaller entrance chamber by a short narrow crawl space. Given the single small (1.5 m x 2 m) known entrance, the mean cave temperature is ~ 22°C (close to the expected mean surface temperature). Mean cave air pCO_2 is ~600 ppm, though this average is based on cave monitoring

data available only from January- March. Therefore, seasonal fluctuations in cave ventilation cannot be ruled out at TM Cave. Lastly, relative humidity is typically >95% year-round.

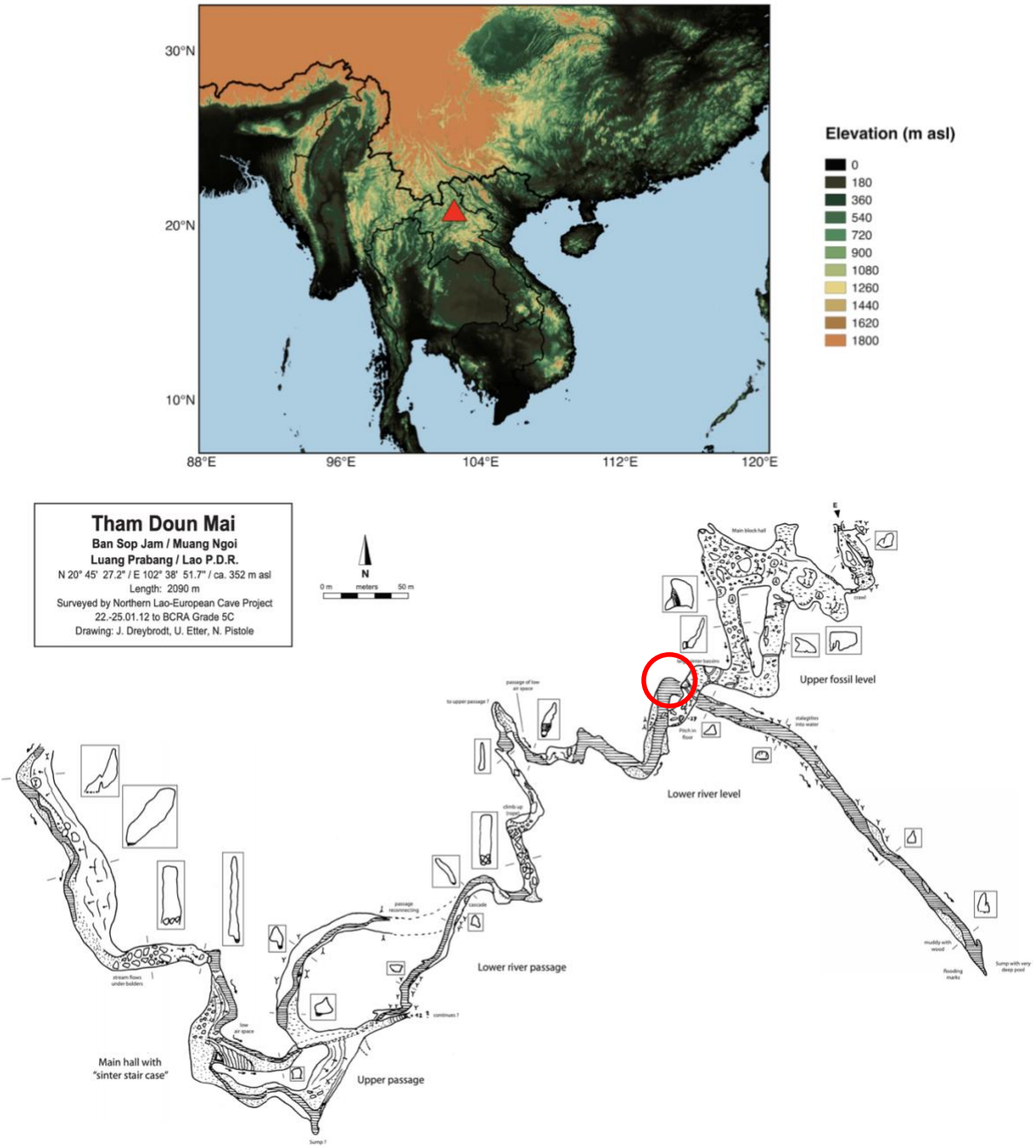

Figure 4.2. Study site location. (a) Elevation map of Southeast Asian region with red triangle representing the location of Tham Doun Mai Cave (TM Cave) in northern Laos. (b) Cave map of TM Cave (Dreybrodt and Laumanns 2013). The red circle represents the location where stalagmite TM-17 sample was collected. The E in the upper right corner represents the entrance into the cave.

A stalagmite record from TM Cave recently published is based on a stalagmite sample, identified as TM-17, and was collected from a steep slope ~200 m from the entrance and roughly halfway down a 26 m drop from the cave upper level to the active river passage (Wang et al. 2019) (Figure 4.2). The slow growth rate, regular and constant morphology, and columnar calcite of TM-17 suggest that the stalagmite likely formed via diffuse flow due to matrix porosity that was constant over time (Treble et al. 2013). TM-17 was not an active stalagmite at the time of collection in 2013 and therefore no monitoring data was obtained at the collection site. However, other drip water and modern calcite samples were collected from nearby sites in TM cave.

4.4. Methods

4.4.1 Cave Monitoring Data

Cave monitoring efforts at TM Cave began in 2010 and are currently ongoing, albeit continuous monthly data are only available for one to two-year periods. These data still provide crucial information to better understand the drip water and karst hydrology characteristics and the cave environment in which the stalagmites are growing. The collected monitoring data are used to calculate the monthly means of relative humidity, temperature, and cave air pCO_2 needed to configure Karstolution. TM Cave drip water data were collected from various drip sites during fieldwork excursions in December 2010, January 2013, February 2015, and February 2017 for stable isotope (Table B.1) and Ca^{2+} measurements (Table B.2). In addition, monthly cave drip water samples were collected by a local Laos contact in 2011 (24 samples collected) for a total of 59 drip water samples (Table B.1). Two sets of hourly temperature (°C) and relative humidity (%) data were collected during the periods of December 2010 until October 2012 and January

2013 through April 2013 using HOBO Pro v2 Temperature/Relative Humidity data loggers placed inside TM Cave.

Records of drip water counts were recorded via a drip water logger (Driptych Stalagmate) that was placed near the cave balcony on which TM-17 was collected (Figure B.1). The balcony drip rate data is available from February 2015 - September 2016. Limited cave air pCO_2 observations and modern calcite $\delta^{18}O$ values were collected via glass plate collections during the fieldwork campaigns. Lastly, a suite of hydro-geochemical measurements, including alkalinity, pH, and conductivity of drip water were periodically collected in 2010, 2013, 2015, and 2017 at various drip water sites (Table B.3).

Drip water pCO_2 data are required to run Karstolution, since ISOLUTION simulates speleothem $\delta^{18}O$ values in dependence of the drip water pCO_2 among other cave parameters. Using the function, CALCPCO2.m, in the ISOLUTION model, the cave drip water pCO_2 values were calculated using the drip water [Ca^{2+}] data collected from drips closest to where TM-17 was collected (Deininger and Scholz 2019). The function converts Ca^{2+} concentrations (in units of mol/l) in a pCO_2-equivalent using the mass laws of CO_2-H_2O-$CaCO_3$-system assuming chemical equilibrium (Deininger and Scholz 2019). Concentrations of Ca^{2+} (in ppm) were an estimate based on inductively-coupled plasma mass spectrometry (ICP-MS) counts per second that were normalized to a standard and multiplied by the standard concentration. An average temperature of 21.5°C was used to calculate the pCO_2-equivalent values for the observational measurements each year. Because drip water Ca^{2+} concentrations were collected from several locations in 2013, 2015, 2017, drip water pCO_2 were averaged among all three years' data and rounded to 2000 ppmV. This value was then implemented as the average drip water pCO_2 year-round in TM Cave.

4.4.2 Input Data

The required climate input data to run Karstolution include monthly values of rainfall, evapotranspiration, and rainfall $\delta^{18}O$. Since long-term precipitation isotope time series from the Global Network Isotope in Precipitation (GNIP) database are limited and discontinuous for Laos, an isotope enabled global spectral model (IsoGSM) (Yoshimura et al. 2008) is used to investigate the hydrological uncertainties in speleothem $\delta^{18}O$. This model applies spectral nudging towards the meteorology captured by the National Center of Environmental Prediction/Department of Energy (NCEP/DOE) reanalyses. As previously mentioned, due to the absence of an extensive monitoring program, assumptions are made that several cave variables, including temperature and relative humidity are held constant all year round. In addition, cave-air and drip water pCO_2 values are limited by non-continuous measurements and also estimated to remain constant throughout the year (Table 4.2). The climatological averaged values configured in the model are as followed: cave temperature is set at a constant value of 22°C year-round, relative humidity is 95%, cave *p*CO2 is 600 ppmV and drip water *p*CO2 is 2000 ppmV.

The parameter values assigned in Karstolution and used to configure the model are listed in Table 4.1. The primary hydrological control on drip water $\delta^{18}O$ is the relative side of each water reservoir and the water flux in and out of each store (Baker et al. 2013). Given a reservoir size that is large relative to the water outflow, $\delta^{18}O$ variability is expected be low and drip water supply to be continuous. Conversely, a high drainage rate relative to the reservoir size results in high $\delta^{18}O$ variability and discontinuous water outflow (Baker et al. 2013). The final configurations are based on values that were chosen arbitrarily but are consistent with values presented in Yang (2016) that assigned the highest volume to the primary karst store (Karst Store 1) followed by the Epikarst store. A series of model runs were attempted to find the “preferred”

parameter set similar to (Baker et al. 2013). However, this method did not yield successful results, since the model could be tweaked arbitrarily with near finite values. Future work beyond the scope of this chapter call for a systemic method to vary each parameter term that more accurately reflects the karst hydrology at TM Cave.

4.4.2. Modified Model Configurations

In previous versions of KarstFor (Baker and Bradley 2010), only fracture flow pathways were considered, which implied that the flow into reservoirs were immediately mixed. In Karstolution, diffuse flow is introduced and includes flow through smaller fractures in which no mixing occurs and follows the approach of (Treble et al. 2013). Diffuse flow can occur when the empty spaces in the karst matrix are not well-connected, leading to slower water flow movement and longer periods of water storage (Fiorillo 2009). Diffuse flow in Karstolution is modeled via a Weibull distribution, which represents different transit time distributions (Almalki and Nadarajah 2014). The amount of diffuse flow each month leaving the epikarst and the resulting flow into Karst Store 1 (KS1) is a user-defined flux (k_diffuse) (Treble et al. 2019).

As a simple case study to test whether a lag may be introduced into the system, the model configuration was subjectively modified. The input data is the same as with the original model configurations presented in Section 4.4.2. and the parameters are forced with the same climatological means as the original configuration. However, the flux out of the Epikarst (F4) when the Epikarst water storage exceeds threshold ‘Epicap’ and the flux representing the diffuse flow are decreased by a factor of 10 ($F4_{modified} = 0.02$, $k\_diffuse_{modified} = 0.001$). The size of Karst Store 2 is increased from 100 mm to 180 mm, the threshold of Karst Store 1 (Ovicap) is increased to from 20 mm to 90 mm and the initial level in karst store is increased from 10 mm to

80 mm. These increase in values were chosen arbitrarily to reflect potential changes in the karst hydrology at TM Cave.

4.5. Results and Discussion

4.5.1. Cave Monitoring Results

In this section, the ongoing cave monitoring efforts in TM Cave are discussed and the averaged values of the data are summarized in Table 4.2 and the data are presented in Appendix B. Altogether, the 59 cave drip water samples collected during these field campaigns have an average $\delta_{18}O$ value of -8.05‰ with a standard deviation of 0.56‰. The average Ca^{2+} concentration of data from 2013, 2015, and 2017 for sites further in the cave (closest to the TM-17 collection site; i.e., > drip water site 5D) is 37.9 ppm (see Figure 4.2). Multiple temperature measurements were collected, and the average temperatures recorded were T= 21.8°C and 100% relative humidity measured from the HOBO data loggers. The annual average of the balcony drip rate was 224 counts per hour (~3.7 counts/minute). The data show clear seasonal variability, such that, there is a rapid increase in counts coincident with the rainy season (boreal summer), followed by exponential decay (Figure B.1). The average cave air pCO_2 values in January-March averaged to be 613 ± 29 ppm, indicating the cave air is well-ventilated. Lastly, the hydro-geochemical measurements from further back in the cave were pH =8.295 (1σ = 0.1), alkalinity=192 ppm (1σ =44.6 ppm), water temperature=22.1°C (1σ=0.6°C), air temperature=21.5°C (1σ=0.9°C), relative humidity= 94.2% (1σ =1.7%), and pCO_2=613.3 ppm (1σ=28.9 ppm).

Table 4.2. Summary table of averaged cave monitoring parameters from TM Cave over the period 2011-2017. *Note that monitoring values are not continuous over the seven-year period and the mean values for temperature (T), relative humidity (RH), CO_2 data are collected from the back half of the cave closest to TM-17 stalagmite collection.

Dates monitored	**2011-2017***
Cave temperature (T/RH Probe)	20.8 ± 1°C
TM HOBO temperature (Dec 2010-Dec 2011)	21.98 ± 0.39°C
TM HOBO temperature (Jan 2013-Apr 2013)	21.76 ± 0.06°C
Balcony drip rate (2015-2016)	3.7 counts /min
pCO_2 (Jan-Mar)	613 ± 29 ppm
Relative humidity	>90%
Mean drip water δD (n=59)	-53.9 ± 4.8‰
Mean drip water $\delta_{18}O$ (n=59)	-8.05 ± 0.56‰
GNIP precipitation $\delta_{18}O$ (OIPC)	-7.09‰
IsoGSM precipitation $\delta_{18}O$ (1979-2009)	-9.56 ± 1.00‰
Glass plate (modern) calcite $\delta_{18}O$	8.68 ± 1.17‰
TM 17 top (modern-ish) calcite $\delta_{18}O$	-8.45‰

4.5.2. Modeled Calcite $\delta_{18}O$ Values

The input time series (precipitation and evapotranspiration) and the fluxes to and from the Epikarst (F1, F3, and F4); fluxes to and from Karst Store 1 (F3, F7, and F5) and Karst Store 2 (F4, F6 and F7) and the water volumes in each reservoir are plotted alongside the five different pseudoproxy $\delta_{18}O$ series: Stal1 to Stal5 in Figure 4.3. The five pseudoproxy series exhibit relatively large differences due to the differences in water pathways through which the drip water feeding each stalagmite travels. The precipitation and evapotranspiration time series exhibit a clear seasonal cycle that influences the variations in F1, which flows from the soil store to the epikarst over time (Figure 4.1). Flow out of Karst Store 1 and Karst Store 2 by F4 and F7, respectfully, also exhibit some seasonal variations in flow, though vary according to changes in water storage, the specific volume thresholds (e.g., Ovicap and Epicap), and the overflow routing. Conversely, flows from the Epikarst (F3) and Karst Store 2 (F6) are highly attenuated.

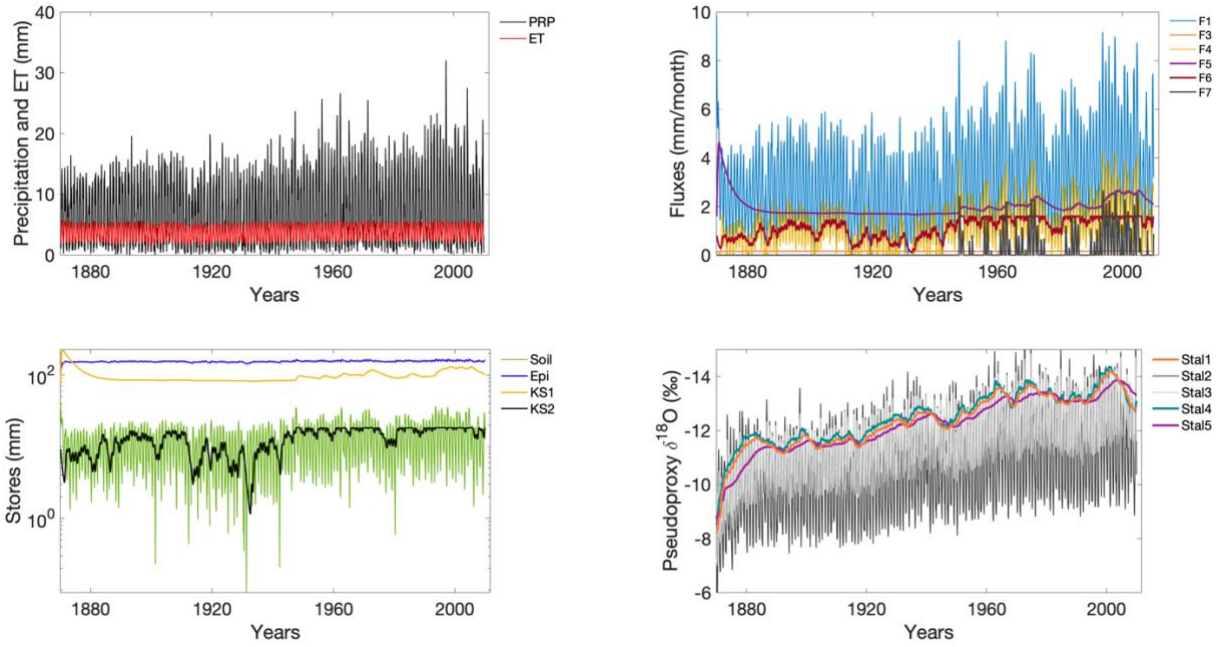

Figure 4.3. Karstolution model inputs and outputs. (a) Input series (precipitation and evapotranspiration (ET), (b) the fluxes in mm/month, (c) various water reservoirs, (d) pseudoproxy time series. Figure adapted from (Baker et al. 2013).

The Stal2 and Stal3 time series both exhibit a clear seasonal trend, since the drip water $\delta_{18}O$ is only affected by the recent rainfall and mixing from Karst Store 1 (Figure 4.3, light and dark grey lines). As a result, these time series maintain the seasonal cycle from the precipitation data and exhibits the highest variability (Figure 4.4). However, the other three pseudoproxy series (Stal1, Stal4, and Stal5) are characterized by lower-frequency variability that is consistent with being fed by drip water from the main water reservoirs (Epikarst, Karst Stores 1 and 2). For comparison, Stal5, which is fed by drip water that is derived from Karst Store 1, has the lowest variability among the other pseudoproxy series (Figure 4.4). This is expected due to the amount of mixing from the epikarst and any overflow routing from Karst Store 2 that feed into large reservoir capacity of Karst Store 1 (Figure 4.1). These results support previous findings that the same climate input time series can produce a range of possible stalagmite $\delta_{18}O$ time series that

reflect difference water pathways and degrees of possible mixing that may have occurred (Baker et al. 2013).

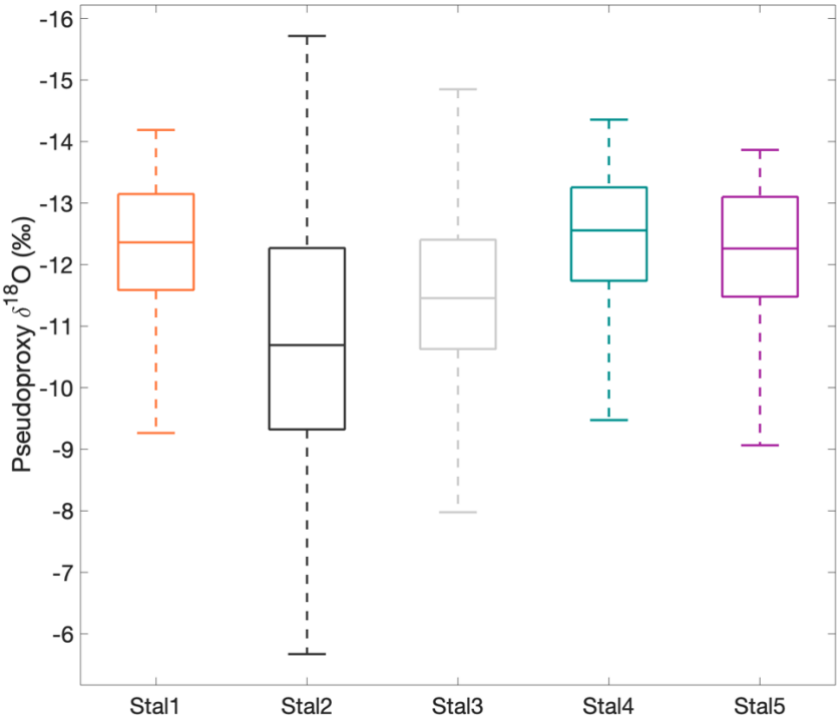

Figure 4.4. Box plots of variability in each pseudoproxy stalagmite $\delta_{18}O$ time series.

Similar to work by Baker et al. (2013), several pseudoproxy series (e.g., Stal1, Stal4, and Stal5) contain low-frequency, decadal-scale variability that are revealed in spectral analyses (Figure 4.5). More specifically, Stal1, Stal4, and Stal5 exhibit ~37-year variability, whereas, Stal2 and Stal3 exhibit interannual variability (2-3 years). The spectral analysis of the IsoGSM precipitation $\delta_{18}O$ data does not show this multidecadal variability, but does exhibit 14-years, 6-year, and 2-3-year periodicities (Figure 4.5). It is possible that the losses of high-frequency annual-scale variability for Stal1, Stal4, and Stal5 are due to mixing in the epikarst and Karst Store 1 (Figures 4.1, 4.4). For Stal5, in particular, any high-frequency variability present in the time series may be driven by recharge events during which precipitation is much greater than

evapotranspiration in the soil store (Baker et al. 2013) but is later smoothed due to mixing with the high storage volume of Karst Store 1.

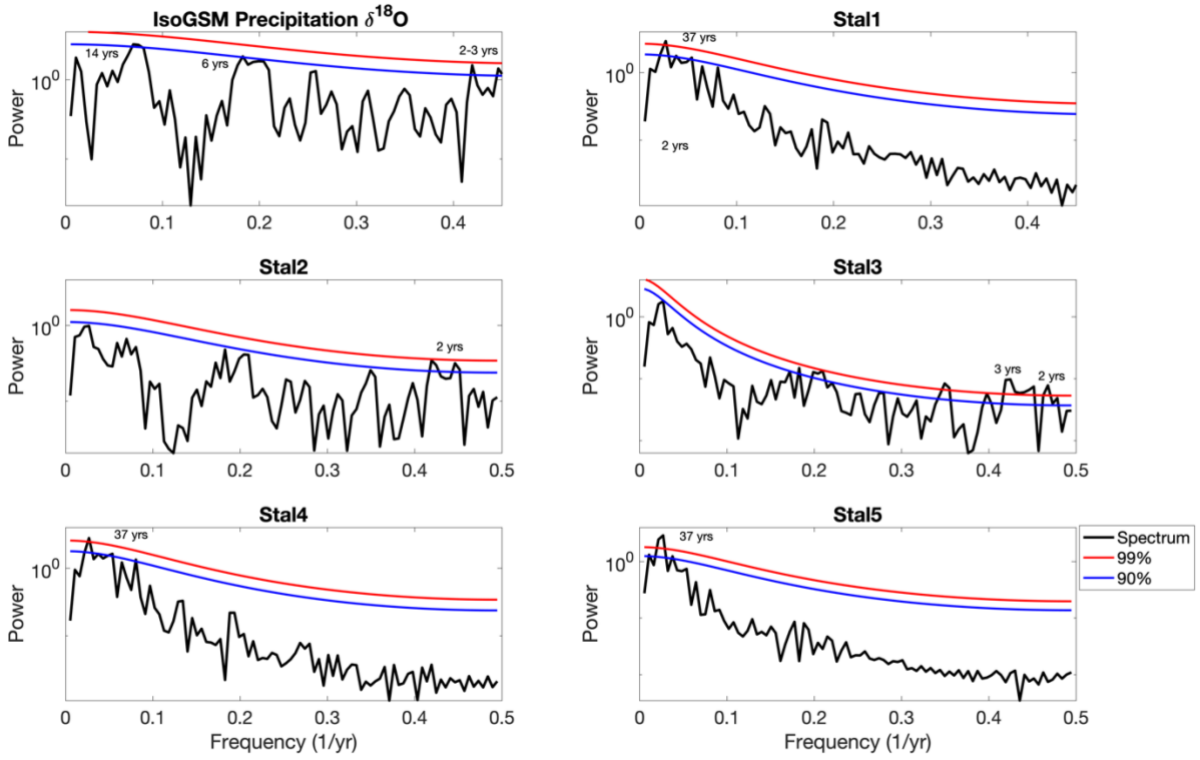

Figure 4.5. Comparison of spectral analyses of each pseudoproxy stalagmite $\delta_{18}O$ series and the IsoGSM precipitation $\delta_{18}O$ input data. The spectral power was performed by REDFIT (Schulz and Mudelsee 2002). The black line indicates the power spectrum. The blue and red dashed lines represent the 99% and 95% confidence limits, respectively, relative to the red-noise spectrum.

However, for Stal2 and Stal3, the high frequency variability is maintained since the recharge for these stalagmites are dominated by mixing of rainfall above the cave (, which maintains the seasonal rainfall $\delta_{18}O$ signatures) and Karst Store 1. By understanding how karst hydrology and mixing may impact variations of $\delta_{18}O$ observed in stalagmites, a karst modeling approach like Karstolution can aid in determining whether high frequency variability is driven by internal cave processes (e.g., isotopic fractionation) or a climate signal due to high recharge events (Frappier et al. 2007; Baker et al. 2013).

Since Stal2 and Stal3 reflect high-frequency variability similar to that of the input $\delta_{18}O$ data, the remainder of the analyses will focus on Stal1, Stal4, and Stal5, which are likely more representative of how karst hydrology may impact stalagmite $\delta_{18}O$ variability at TM Cave. Under isotopic equilibrium conditions, variations in speleothem $\delta_{18}O$ are influenced by drip water $\delta_{18}O$ and temperature (Kim and O'Neil 1997; Wackerbarth et al. 2010). Therefore, when modeled stalagmite $\delta_{18}O$ values are similar to that of the observed $\delta_{18}O$ values, it is common to assume the speleothem grew in near or at isotopic equilibrium conditions (Mickler et al. 2006; Bradley et al. 2010). Karstolution considers disequilibrium effects (e.g., disturbance of isotope equilibrium between $CaCO_3$, HCO_3, and H_2O), which includes in-cave disequilibrium isotope and evaporative fractionation. However, kinetic fractionation (e.g., the change of the isotope fractionation factor in relation to precipitation rate) (Dietzel et al. 2009) is not accounted for Karstolution.

Kinetic fractionation can be calculated as the difference between the Karstolution modeled values and observed $\delta_{18}O$ values. While modern observed stalagmite $\delta_{18}O$ values are not available at TM Cave, the simulated Karstolution output are compared with output from applying the equilibrium stable isotope fractionation factor of Kim and O'Neil (1997) (Figure 4.6). By comparing the two outputs, it is possible to quantify the impact of cave non-equilibrium processes, given that Karstolution accounts for in-cave evaporative and disequilibrium isotope fractionation, in addition to, the equilibrium fractionation effected generated by Kim and O'Neil (1997). Generally speaking, the modeled drip water $\delta_{18}O$ output converted to calcite assuming equilibrium oxygen isotope fractionation and the Karstolution output with the ISOLUTION model enabled share good agreement (Figure 4.6). The average off-set between the time series calculated using the Kim and O'Neil (1997) equation and Stal1, Stal4, and Stal5 time series are

0.53‰, 0.39‰, and 0.55‰, respectively. Previous cave monitoring data also show that modern calcite $\delta_{18}O$ values from glass plates placed in TM Cave are within the range of the predicted equilibrium values (Kim and O'Neil 1997) (Appendix A). The small variations between the Karstolution output and the calculated equilibrium fractionation output may be attributed to disequilibrium isotope fractionation and will be further assessed and discussed in the next section.

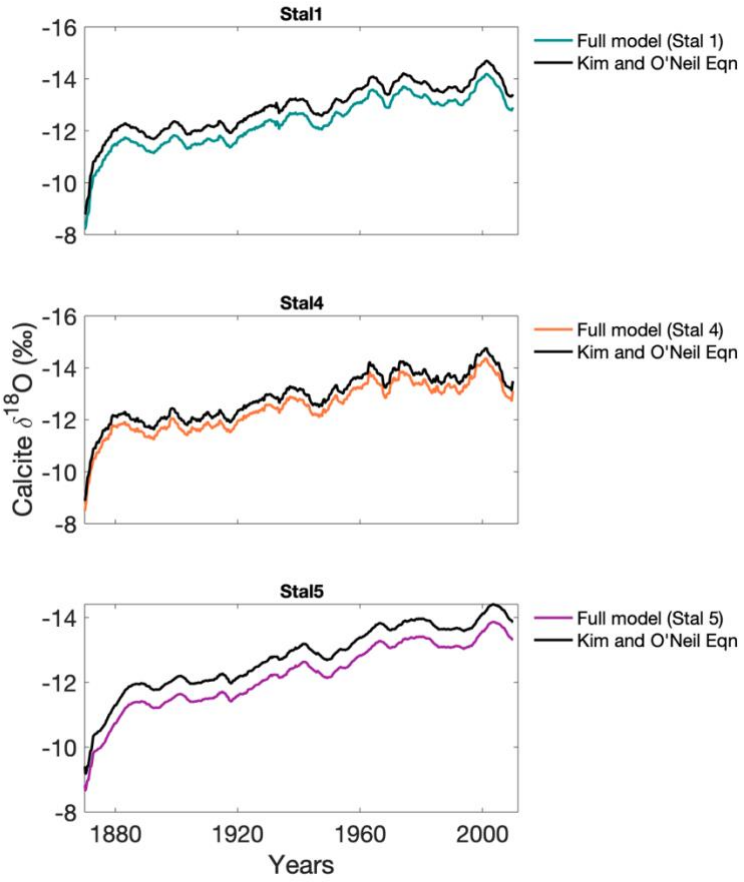

Figure 4.6. Comparison of modeled stalagmite $\delta_{18}O$ from Karstolution (black line) and modeled drip water $\delta_{18}O$ output converted to calcite assuming equilibrium oxygen isotope fractionation using the Kim and O'Neil (1997) equation (grey lines). Figure adapted from Treble et al. (2019).

4.5.3. Sensitivity Analyses

Sensitivity tests were conducted for pseudoproxy Stal1, Stal4, and Stal5 times series to evaluate which cave parameters may drive stalagmite variability at TM Cave and to quantify the impact of in-cave equilibrium fractionation. The "reference" case in these tests refer to the cave configurations and input data presented in Table 4.1 and Section 4.4.2, whereas constant perturbations were made to the different cave parameters: cave temperature, drip interval, relative humidity, and changes in pCO_2 between the cave air and drip water.

Pseudoproxy Stal1 time series exhibits a sensitivity to cave temperature, suggesting a temperature dependence of isotope fractionation under equilibrium conditions (Mühlinghaus et al. 2009) (Figure 4.7a). The averaged absolute differences between the reference time series and the perturbed parameters time series are ~0.40‰. More negative $\delta^{18}O$ signatures for warmer cave temperatures (e.g., T=24°C) (Figure 4.7a, green line) is consistent with the temperature-dependent fractionation of ^{18}O between calcite and water, such that, as temperature increase, $\delta^{18}O$ of $CaCO_3$ decreases (~-0.23‰/°C) (Kim and O'Neil 1997). As for potential isotopic impacts of disequilibrium processes, Stal1 does not appear to be sensitive to changes in drip interval when relative humidity is held constant at 95% (the same relative humidity as the reference case) (Figure 4.7b). However, a longer drip interval combined with lower relative humidity (50%) shows a minor increase in $\delta^{18}O$ (Figure 4.7b, green line). Additionally, Stal1 exhibits a sensitivity to combined changes in relative humidity and cave ventilation (i.e., droplet evaporation) (Figure 4.7c). When relative humidity is held constant at >95%, negligible isotopic effects are observed despite changes in ventilation (Figure 4.7c; blue, green, and dashed lines). Conversely, combined effects of a lower relative humidity and increased ventilation generate large isotopic differences and also short hiatuses in the time series (Figure 4.7c, red line).

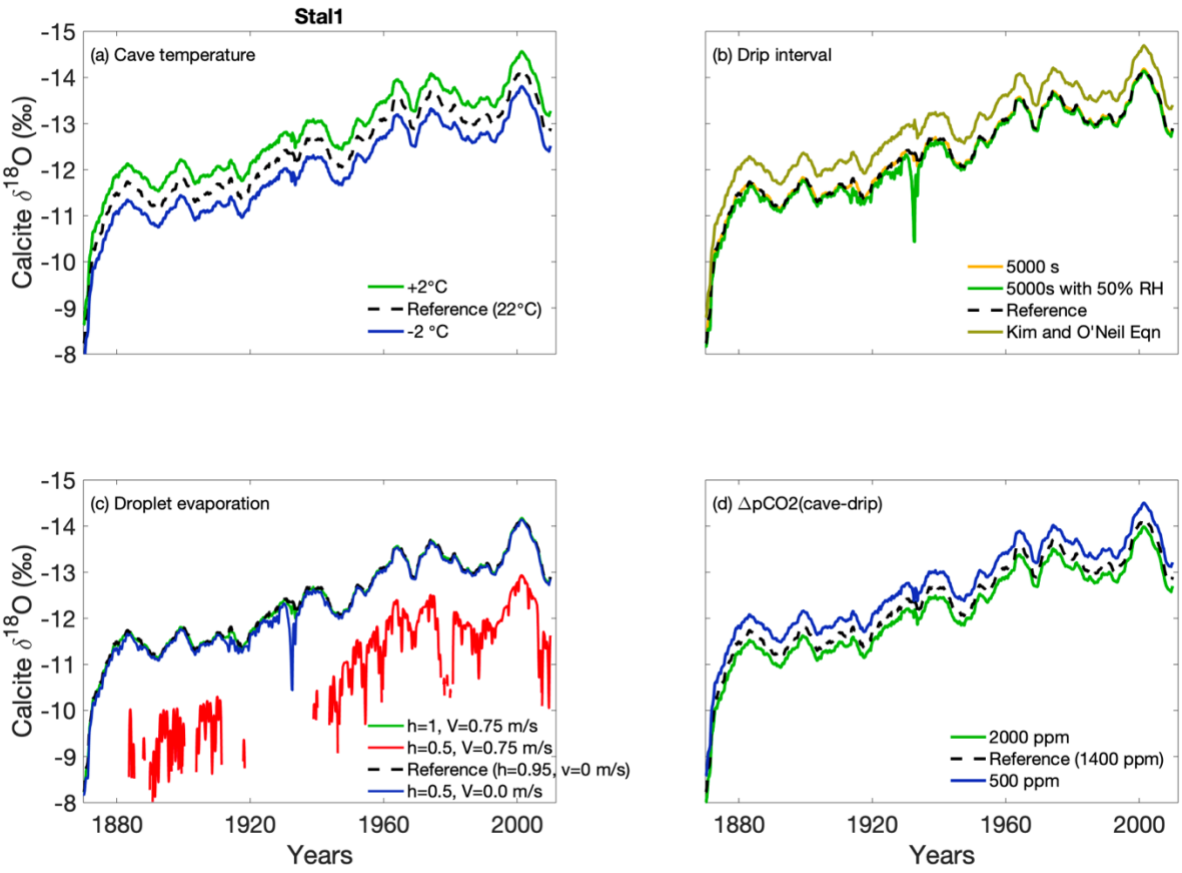

Figure 4.7. Sensitivity analysis for cave parameters at TM Cave for pseudoproxy Stal1. (a) cave temperature. (b) drip interval with modified relative humidity (RH) value. (c) relative humidity (h) and cave ventilation (v). (d) cave air minus drip water pCO_2. The reference case in each panel uses the monthly values from the original configuration. The perturbations have a constant offset across all months. The predicted equilibrium calcite $\delta_{18}O$ from Figure 4.6 is shown in 4.7b for comparison (labeled as "Kim and O'Neil Eqn"). Figure adapted from Treble et al. (2019).

Lastly, Stal1 demonstrates a slight sensitivity to changes in the cave air and drip water *p*CO2 gradient (Figure 4.7d). A large pressure gradient (e.g., 2000 ppm) results in more positive $\delta_{18}O$ values and an absolute difference of ~0.21‰ (Figure 4.7d, green line). However, a smaller pressure gradient (e.g., 200 ppm), which implies reduced supersaturation of the cave drip water with respect to calcite due to an increase in cave air pCO_2, results in lower $\delta_{18}O$ values (absolute difference: 0.33‰) (Deininger et al. 2019) (Figure 4.7d, blue line). These results are consistent

with the concept that large pCO_2 gradients between the drip and cave atmosphere may favor rapid degassing, which can result in an enrichment in ^{18}O due to isotopic disequilibrium in calcite (Hendy 1971).

Pseudoproxy Stal4 time series also exhibits a sensitivity to cave temperature (Figure 4.8a) and the absolute differences between the reference time series and the perturbed time series are ~0.37‰. Stal4 does not exhibit a sensitivity to changes in drip interval, even with a change in relative humidity (Figure 4.8b, green line), unlike Stal1. The largest change in the modeled calcite $\delta^{18}O$, in response to effects of droplet evaporation, occurs when the relative humidity is 50% and the ventilation is increased (Figure 4c, red line). However, there are no changes when relative humidity is >95% and ventilation is constant or increases (Figure 4c, blue, green, and dashed lines). Finally, Stal4 exhibits minimal isotopic effects of changes in the cave air and drip water pCO_2 gradient (Figure 4.8d). The isotopic differences between the reference and the perturbed time series are 0.24‰ and 0.14‰ for the small and large *p*CO2 gradients, respectively.

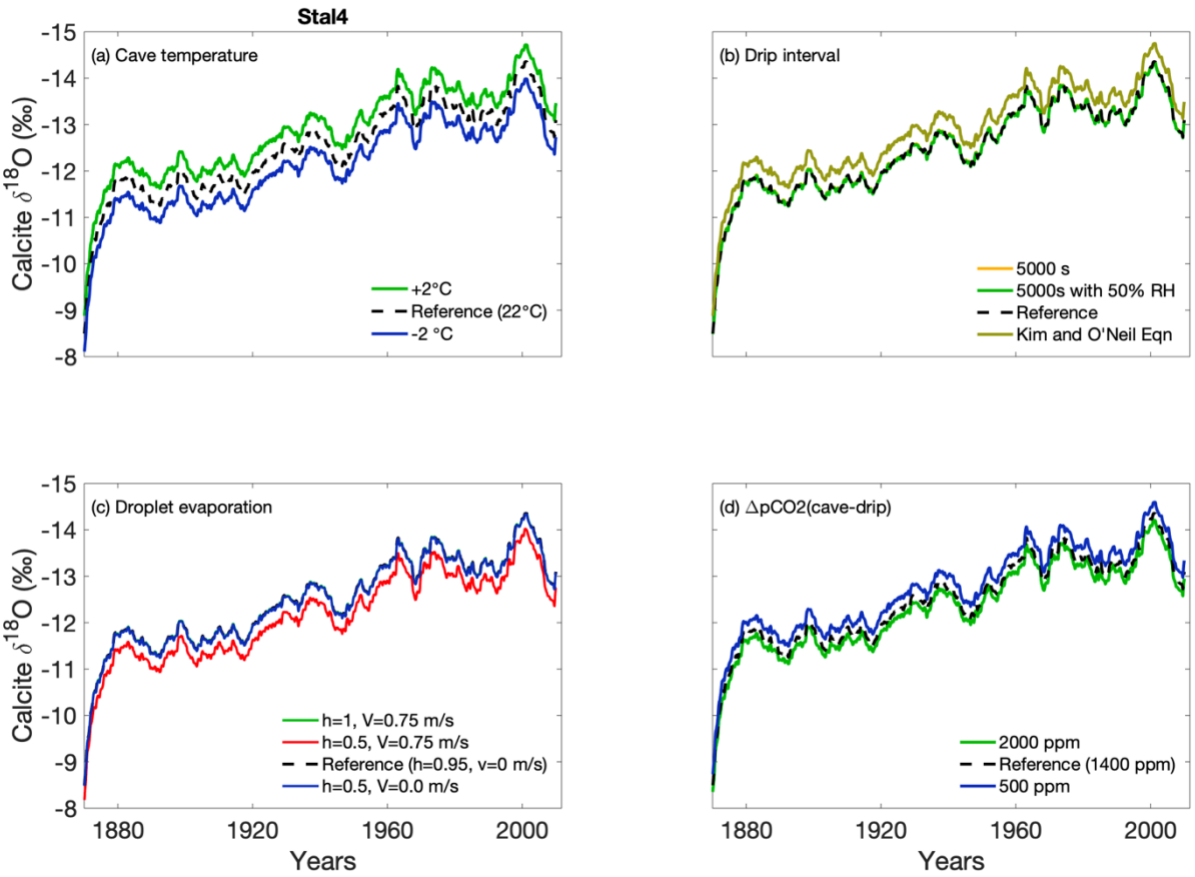

Figure 4.8. Sensitivity analysis for cave parameters at TM Cave for pseudoproxy Stal4. (a) cave temperature. (b) drip interval with modified relative humidity (RH) value. (c) relative humidity (h) and cave ventilation (v). (d) cave air minus drip water pCO_2. The reference case in each panel uses the monthly values from the original configuration. The perturbations have a constant offset across all months. In addition, the predicted equilibrium calcite $\delta_{18}O$ from Figure 4.6 is shown in 4.8b for comparison (labeled as "Kim and O'Neil Eqn"). Figure adapted from Treble et al. (2019).

Pseudoproxy Stal5 responds similarly to the four varied cave parameters as pseudoproxy Stal1 (Figure 4.9). In addition to a sensitivity to temperature (absolute difference: 0.40‰) (Figure 4.9a), Stal5 also only exhibits minor impacts of changes in drip interval (Figure 4.9b), though a longer drip interval combined with lower relative humidity (50%) does shows a minor increase in $\delta_{18}O$ (Figure 4.9b, green line). Stal5 exhibits negligible isotopic effects when relative humidity is high, regardless of any changes in ventilation (Figure 4.9c; blue, green, and dashed

lines), similar to the results for Stal1. However, the combined effects of lower relative humidity and increased ventilation led to Stal5 to stop growing (i.e., growth rate = 0 mm/month) (Figure 4.9c, red line). Pseudoproxy Stal5 also demonstrates a small sensitivity to changes in the cave air and drip water pCO_2 gradient (Figure 4.9d). The larger pressure gradient results in more positive $\delta_{18}O$ values (absolute difference: ~0.21‰), whereas the smaller pressure gradient results in lower $\delta_{18}O$ values (absolute difference: ~0.34‰) (Deininger et al. 2019) (Figure 4.9d, blue line).

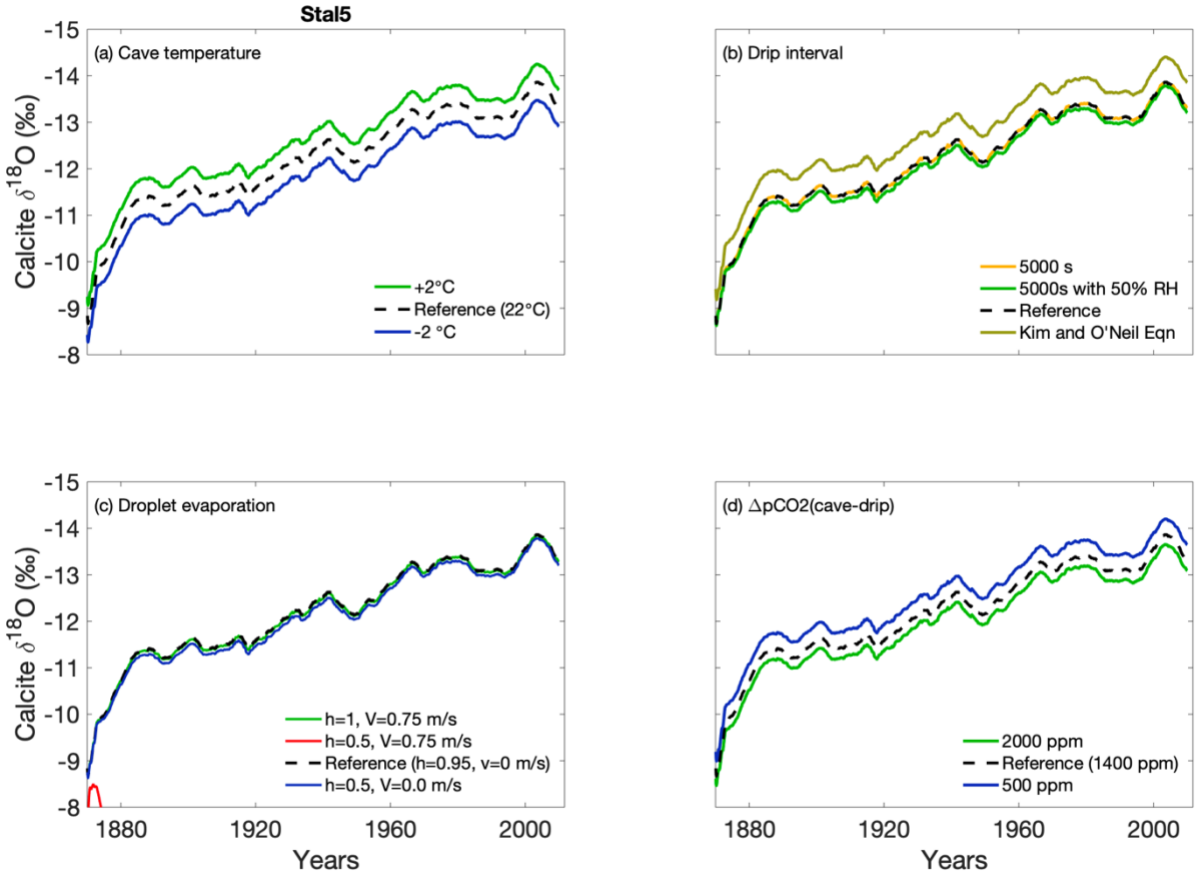

Figure 4.9. Sensitivity analysis for cave parameters at TM Cave for pseudoproxy Stal5. (a) cave temperature. (b) drip interval with modified relative humidity (RH) value. (c) relative humidity (h) and cave ventilation (v). (d) cave air minus drip water pCO_2. The reference case in each panel uses the monthly values from the original configuration. The reference case in each panel uses the monthly values from the original configuration. The perturbations have a constant offset across all months. In addition, the predicted equilibrium calcite $\delta_{18}O$ from Figure 4.6 is shown in 4.9b for comparison (labeled as "Kim and O'Neil Eqn"). Figure adapted from Treble et al. (2019).

4.5.4. Discussion for the Sensitivity Analyses

The cave-parameter sensitivity analyses revealed sensitivities of TM cave stalagmite $\delta^{18}O$ to cave temperature and changes in the cave air and drip water pCO_2 gradient. Generally speaking, all three time series showed little to no responses to any changes in drip interval with a constant relative humidity greater than 95%, unlike the results presented in (Treble et al. 2019). Longer drip intervals may increase the degree of disequilibrium effects and result in increased $\delta^{18}O$ values of speleothem calcite (Mühlinghaus et al. 2009; Deininger et al. 2012). However, given the high relative humidity (95%) assigned in the model, evaporation processes may not be taking place (i.e., evaporation effects may be neglected), regardless of the drip interval (Deininger et al. 2012), thus mostly unaffecting the calcite $\delta^{18}O$ values.

The effects of droplet evaporation were much greater for Stal1 and Stal5 than Stal4 (Figures 4.7c, 4.9c). Stal1 and Stal5 experienced periods of 0 mm/month growth rates (i.e., growth hiatuses) when the relative humidity was 50% and the ventilation increased to 0.75 m/s. These results are puzzling, since increased ventilation is typically assumed to increase calcite deposition, thus calcite growth rates (Deininger et al. 2012; Deininger and Scholz 2019). For example, sudden changes in ventilation, which implies more mixing with the low pCO_2 outside air and increased the ratio between drip water pCO_2 and cave air, can result in high calcite deposition rates (Baldini et al. 2008). Additionally, increased evaporation rates (in response to lower relative humidity and increased ventilation) may have significant effects on calcite $\delta^{18}O$, since H_2O is evaporated from the solution layer, and also result in higher calcite precipitation rates (Deininger et al. 2012). However, these evaporation effects may be ignored when relative humidity is greater than 85% and ventilation is less than 0.2 m/s (Dreybrodt and Deininger

2014), which supports the negligible differences in the other time series when relative humidity is >95% and/or ventilation is 0 m/s (Figures 4.7-4.9).

These results further highlight how different stalagmites from the same cave site may experience different variations in calcite $\delta_{18}O$. While it may be expected that in-cave processes, such as relative humidity and ventilation, should impact calcite $\delta_{18}O$ in a similar manner, it is evident from the results that Stal1 and Stal5 exhibit much higher sensitivities, whereas Stal4 shows only limited disequilibrium effects from droplet evaporation. A possible explanation may be that the user-prescribed model configurations lead to instability in Karstolution, thus preventing a continuous time series to be generated for Stal1 and Stal5. For example, the parameters chosen may not lead to ideal conditions for continuous calcite precipitation under certain cave environments. Thus, the combined effects of the different fluxes in and out of Karst Store 1 and Karst 2 (, which do not directly impact Stal4) and the perturbed cave parameters may cause disruptions in the drip water solution available for calcite precipitation. Nonetheless, these hypotheses are speculative and call for additional analyses and longer cave monitoring data to further identify how changes in karst hydrology and the different pathways and mixing at TM Cave may influence stalagmite $\delta_{18}O$.

4.5.5 Modeled $\delta_{18}O$ Values with New Configurations

The modified Karstolution configuration yielded similar results for Stal2 and Stal3, which preserves similar high-frequency variability that reflects the seasonal variability of the precipitation input data (Figure 4.10). Changes in Stal4 and Stal5 time series are negligible, while Stal1 time series is varied the most. The fluxes out of Karst Store 2 (F6) and epikarst (F4) no longer exhibit high-frequency seasonal variability but are instead characterized by low-

frequency variability (Figure 4.10). Additionally, the flux out of Karst Store 2 if the volume threshold has surpassed (F7) exhibits a continuous rate of 0 mm/month, confirming that the increased volume storage in Karst Store 2 does not permit overflow routing. Subsequently, the greatest change among the stores between the original and modified configuration is reflected in Karst Store 2 (Figure 4.10). The high-frequency variability is smoothed throughout and the variability over time is reduced. Furthermore, the volume of Karst Store 1 has subsequently decreased since there is no longer overflow routing through F7 and the rate of diffuse flow has decreased as well.

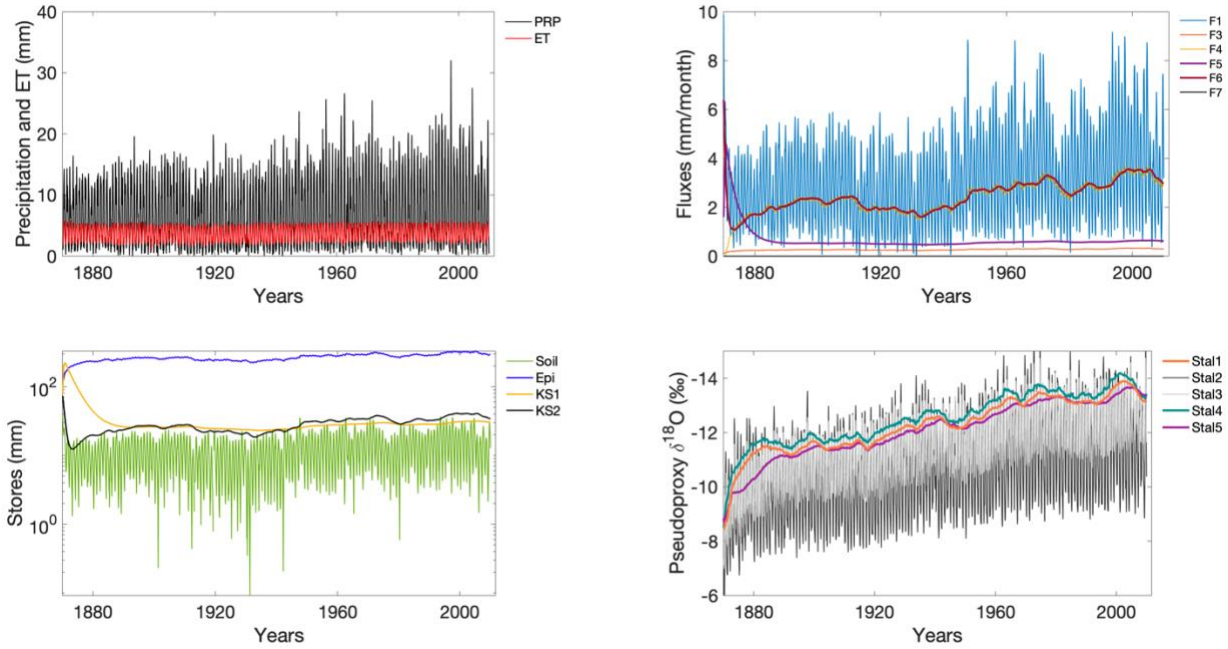

Figure 4.10. Karstolution model inputs and outputs with the modified configuration. Refer to text for new parameter values. (a) Input series (precipitation and evapotranspiration (ET), (b) the fluxes in mm/month, (c) various water reservoirs, (d) pseudoproxy time series. Figure adapted from Baker et al. (2013).

Given the modified configurations, the new pseudoproxy time series for Stal1 demonstrates a one-year lag from the Stal1 time series in the original configuration. Although a one-year lag may be insignificant given that stalagmite sampling resolutions are ~5 years, this

result demonstrates that changes in stalagmite $\delta^{18}O$ variability may be altered depending on the fluxes in and out of the stores, the volumes, and the overall water balance of the karst system. Additionally, these results will likely vary from site to site. For example, a study site with a thicker overlying limestone (such as TM Cave) would experience a potentially longer transit time and groundwater mixing than a different site with less than 100 m overlying the cave (Lachniet 2009). Notwithstanding this simplistic case study, Baker et al. (2013) showed that nonstationarity in pseudoproxy stalagmite $\delta^{18}O$ variability may occur since the nonlinear changes respond to changes in water balance that impact the karst aquifer storage. Further work is needed to identify how the degree of changes of parameters in the model may tweak the pseudoproxy time series.

4.6. Conclusions

Proxy system modeling can be used to identify and quantify uncertainties associated with interpretations of speleothem $\delta^{18}O$ and other climate proxies. The objectives of this chapter were to investigate how karst hydrology impacts cave drip water $\delta^{18}O$ and how in-cave parameters may impact drip water $\delta^{18}O$ prior to calcite precipitation. The results show that non-climatic hydrological processes should be considered to evaluate the controls on speleothem $\delta^{18}O$. These processes can include drip-water hydrology (e.g., different flow pathways and flow rates), surface and sub-surface climatology (e.g., soil characteristics, evapotranspiration) and in-cave processes that may affect the signals preserved in speleothem $\delta^{18}O$ (Bradley et al. 2010; Wackerbarth et al. 2010; Dreybrodt and Scholz 2011). Assessing the uncertainties in the interactions between climatic and non-climatic processes on speleothem $\delta^{18}O$ can further sharpen and constrain our signal interpretations (Evans et al. 2013).

This chapter focused on using an integrated stalagmite $\delta^{18}O$ PSM that accounts for both in-cave isotope fractionation and karst hydrological processes. We confirm the use of Karstolution by applying the site-specific climate information for TM Cave in northern Laos. At TM Cave, the preliminary results suggest that modeled stalagmite $\delta^{18}O$ variability is driven by the climatic input, the karst system, and in-cave processes, though this may vary within cave stalagmites. The degree of isotope equilibrium introduced strongly depends on the input parameters (Mühlinghaus et al. 2009; Deininger et al. 2012) and the dependence of $\delta^{18}O$ values on cave specific parameters were quantified through sensitivity tests. The cave-parameter sensitivity analyses showed that Stal4 demonstrates sensitivity to cave temperature, but minimal isotopic effects of changes in evaporation and cave air and drip water pCO_2 gradient, whereas Stal1 and Stal5 are not only sensitive to temperature changes and the cave air and drip water pCO_2 gradient, but also potentially more influenced by evaporation processes.

Additionally, Stal1, Stal4, and Stal5 did not exhibit significant high-frequency variability, likely due to hydrological mixing driven by various storage properties and changes in water balance. Continued monitoring data and further research are needed to further investigate how processes governing drip water $\delta^{18}O$ not only impact different cave sites, but sampling sites within the same cave (Moerman et al. 2014). Finally, the simple case study to simulate a one-year lag was forced via subjectively-modified parameters, suggesting that a seasonal or yearly lag may be introduced into the proxy system through changes in the water reservoir size and water inflows and outflows. Additional work is required to further identify the relative importance of each parameter and how this may vary at different sites.

This work has important implications for paleoclimate studies, because it supports how stalagmite $\delta^{18}O$ may be directly impacted by hydrological variability and in-cave processes that

should be considered when interpreting decadal-centennial scale changes in stalagmite $\delta^{18}O$ records. More importantly, these results have direct implications for any additional stalagmite $\delta^{18}O$ record from TM Cave. The sensitivity results support the importance of having pCO_2 measurements year-round since the pseudoproxy stalagmite series did exhibit minor sensitivities to changes in the pCO_2 gradient between the cave air and drip water pCO_2. Additionally, it may be valuable to also consider seasonal change in ventilation and relative humidity given the sensitivity results, However, the current monitoring data do show that relative humidity remains >95% year-round and pCO_2 measurements from January-March indicate the cave is well-ventilated. Thus, it is possible that the configurations in this initial analysis may not fully represent the cave environment and karst hydrology at TM Cave. Nonetheless, this work provides the foundation for additional proxy system modeling studies from TM Cave and the Southeast Asian region and calls for additional work to progress and refine these conclusions.

Chapter 5

5 Conclusions

5.1. Summary of Work

The overarching goal of my dissertation was to analyze changes in Southeast Asian hydroclimate on interannual to centennial timescales during the Common Era. In order to achieve this goal, I created a new, high-resolution stalagmite proxy record that spans roughly 1,900 years, analyzed modern changes in precipitation variability in response to atmosphere-ocean teleconnections, and investigated how non-climatic factors can influence climate signals recorded in stalagmites to provide better insights on changes in local to regional hydroclimate.

In Chapter 2, I presented the first high-resolution stalagmite record from northern Laos that spans most of the Common Era. Centennial-scale changes in local water balance were observed in the stalagmite $\delta^{13}C$ values. The timing of the driest period in the $\delta^{13}C$ record (late 14th and early 15th centuries) aligned with that of large 'megadroughts' (e.g., Angkor Droughts and Strange Parallels drought) also recorded in nearby tree-ring records. On the other hand, multidecadal to centennial changes in stalagmite $\delta^{18}O$ were linked to changes in monsoon intensity and exhibited an inverse relationship with solar variability from 1200 CE onwards. Using solar-forced climate model simulations from the Community Earth System Model-Last Millennium Ensemble (CESM-LME), I showed that centennial-scale $\delta^{18}O$ variability over the past millennium may be linked with solar-forced changes in upstream rainout over the tropical Indian Ocean. Large-scale circulation changes initiated by solar-forced warming of Atlantic sea surface temperatures may have led to modified moisture $\delta^{18}O$ values transported to our study site without necessarily influencing the amount of rainfall that fell at our study site. The novel method comparing solar-forced climate model simulations with proxy data and the proposed

hypothesis provide additional avenues to further investigate mechanisms controlling stalagmite $\delta_{18}O$ and provide more insights on the influence of both internal climate variability and external forcings on AM variability.

In Chapter 3, I investigated interannual precipitation patterns across East China and Southeast Asia. Through empirical orthogonal function (EOF) analysis, tripole and dipole rainfall patterns were observed across the broader Asian monsoon region. In-phase rainfall patterns between Southeast Asia and South China associated with the tripole EOF pattern were linked to the delayed precipitation response to the El Niño-Southern Oscillation (ENSO). However, out-of-phase rainfall patterns between Southeast Asia and South China in the dipole precipitation mode were associated with a simultaneous remote influence of the summer North Atlantic Oscillation (SNAO). These results suggest that observed in-phase and out-of-phase variations in precipitation between MSEA and South China can be used to gauge the relative importance of local Pacific and remote Atlantic influences on AM rainfall. Therefore, this study has implications to better understand both future changes in rainfall patterns in response to shifts in the climate system and also past changes in tripole/dipole precipitation patterns on interannual to centennial timescales.

In Chapter 4, I used a new proxy system model, Karstolution, to identify how variations in karst hydrology and in-cave processes may impact recorded stalagmite $\delta_{18}O$ values. I conducted a case study for our main study site, Tham Doun Mai Cave (TM Cave) in northern Laos, using the available cave monitoring data. The results showed that several of the pseudoproxy time series lost high-frequency variability due to the various hydrological pathways and mixing assigned in the model. Sensitivity analyses further revealed that both karst hydrology and in-cave processes and properties may have an influence on stalagmite $\delta_{18}O$ at TM Cave,

though the quantitative disequilibrium effects could vary from sample site to sample site. In addition, modifications to the user-defined configurations in Karstolution forced a one-year lag for one of the pseudoproxies, which suggests that a seasonal to annual lag may be introduced when the reservoir sizes are increased, and water inflows and outflows are slowed. However, further research will be required to systematically change the parameters that are realistic to study site.

Overall, the objectives in my dissertations were addressed through my three main chapters. I identified how Southeast Asian hydroclimate varied over the last two millennia through a new stalagmite $\delta_{18}O$ and $\delta_{13}C$ record. The dominant mechanisms that characterize interannual MSEA precipitation were investigated using a 30-year precipitation dataset and EOF analysis. This work identified both in-phase and out-of-phase couplings of modern-day MSEA and EASM precipitation through tripole and dipole modes and linked to phases of ENSO and NAO, respectively. These findings have implications for paleoclimate studies that focus on changes in past monsoon variability, specifically spatial rainfall patterns, across East China and MSEA. Lastly, my final chapter addressed the impact of karst hydrology and water pathways that may influence stalagmite $\delta_{18}O$ time series. In-cave disequilibrium isotope fractionation were identified to play an important role on changes in stalagmite $\delta_{18}O$, particularly, cave temperature and ventilation changes. Comprehensive cave monitoring efforts that include seasonal recordings of temperature, *p*CO2, drip rate and relative humidity are essential in modeling the stalagmite $\delta_{18}O$ proxy system and continued work is needed to improve the processes implemented in proxy models.

My dissertation research provides additional information regarding changes in past monsoon intensity, local water balance, karst hydrology, and modern rainfall patterns that focus

on the Southeast Asian region. This research builds upon the limited number of paleoclimate records from Laos and the surrounding countries, while contributing to modern rainfall studies that are focused mostly in East China and including Southeast Asia into these analyses. Finally, my work expands on the ongoing proxy system modeling studies to better interpret paleoclimate records and improve our projections of future climate change.

5.2. Future Research Avenues and Questions

5.2.1. Additional Paleoclimate Records and Linkage to Solar Forcing

A new hypothesis was proposed in Chapter 2 that links changes in monsoon intensity to solar-forced changes in the tropical Atlantic Ocean sea surface temperatures, which led to changes in overturning circulation in the atmosphere and ultimately impacted precipitation over the tropical Indian Ocean. There are multiple directions branching off from this research. First avenue would be to test this hypothesis with other stalagmite records from the broader Asian Monsoon region using not only the same Community Earth System Model Last Millennium Ensemble (CESM) solar-only forcing runs (Otto-Bliesner et al. 2016), but also new isotope-enabled climate runs in the CESM (iCESM), which allows for more direct comparisons between stalagmite $\delta_{18}O$ proxy data and modeled isotopes (Zhu et al. 2017). It is possible that the future results may not be entirely straight forward given stalagmite $\delta_{18}O$ controls on both local to regional spatial scales at different cave sites. For example, testing this hypothesis with a cave site in northern China that is influenced by the East Asian Monsoon, as opposed to the Southeast Asian Monsoon, may not yield similar findings, since moisture source regions and transports vary from site to site. In addition to testing this hypothesis for different study sites, additional analyses would need to be done to investigate the periodicity of this proposed monsoon-solar

relationship. The findings in Chapter 2 found the relationship holds true after 1200 CE and on centennial timescales. It would be worthwhile to test whether this hypothesis holds true for new stalagmite records, including a new 2,700-year stalagmite $\delta_{18}O$ record from Thailand (Tan et al. 2019), on decadal to multicentennial timescales.

Another area of future research work includes investigating the response of tropical Atlantic sea surface temperatures (SSTs) and the Asian monsoon. This was beyond the scope of Chapter 2 but is important for future climate projections to better understand how ocean-atmosphere teleconnections in response to changes in solar variability may impact Asian monsoonal rainfall. One method would be to investigate Atlantic SSTs – Asian monsoon links by comparing Asian Monsoon $\delta_{18}O$ records with paleoclimate records from the tropical Atlantic and/or stalagmite records from the South American monsoon region (Novello et al. 2012, 2016). While the South American monsoon records do exhibit a similar monsoon-solar forcing relationship found, the TM-17 stalagmite record presented in Chapter 2 shows no significant correlation with the Brazil speleothem data, which would need to be further investigated in the future.

5.2.2. Modern Precipitation Patterns

I used high-resolution satellite precipitation data to examine spatial precipitation patterns across East China and Southeast Asia over the last several decades. However, in order to uncover whether these relationships hold on interdecadal or longer timescales, longer precipitation datasets spanning at least the last hundred years and beyond would be required (i.e., Global Precipitation Climatology Centre (GPCC) (Schneider et al. 2014). Longer observational precipitation datasets would enable further analyses on decadal shifts in precipitation patterns

similar to previous work that found a climatic shift in the dipole and tripole patterns following the late 1970s (Gong and Ho 2002; Ding et al. 2008) In addition to longer observational datasets, future work would benefit from using modeled precipitation data, such as from the Community Earth System Model – Large Ensemble (CESM-LENS) (Kay et al. 2015) to investigate changes in rainfall patterns on multidecadal to centennial timescales. Targeted atmosphere global climate model (AGCM) experiments could also provide additional evidence for the potential mechanisms concluded in Chapter 3. For example, forcing an AGCM with an El Niño-like pattern of SST anomalies would bring further clarity to the potential causal relationship between tropical Pacific forcing and the spatial precipitation patterns discussed in Chapter 3.

Investigations of these modern interannual precipitation patterns across the broader Asian Monsoon region can be directly applicable and helpful when interpreting past records of Asian monsoon precipitation. By using longer precipitation datasets and/or numerical experiments, it would be possible to further test the hypotheses and proposed mechanisms presented in Chapter 3 with paleoclimate records. For example, spatial hydroclimate patterns identified through syntheses of high-resolution paleoclimate records across East China and Southeast Asia could show distinct dipole or tripole pattern and may be attributed to the mechanisms presented in Chapter 3. This work would help improve our collective understanding of regional precipitation variability on annual to multidecadal timescales across the Asian monsoon region.

5.2.3. Modeling Multidecadal Lags Using Proxy System Models

The new, high-resolution stalagmite record presented in Chapter 2 investigated changes in hydroclimate over Southeast Asia spanning the last two millennia. While this record was compared with regional stalagmite records and provides additional insights into changes in

upstream rainout and local hydroclimate in Laos, it is also necessary to compare with local and regional tree ring records, particularly in the context of proxy system modeling. Tree rings are beneficial climate recorders of past climate due to the high temporal resolution and precisely dating methods (Hughes 2002). Many hydroclimate reconstructions using tree ring width and cellulose oxygen isotope (cellulose $\delta^{18}O$) from cypress trees in Vietnam (*Fokienia hodhinsii*) have provided evidence for widespread multi-decadal droughts in Southeast Asia (Buckley et al. 2010). Cellulose $\delta^{18}O$ is primarily controlled by two factors: $\delta^{18}O$ of the source water (e.g., precipitation) and relative humidity (Robertson et al. 2001). Therefore, studies have reconstructed past precipitation and/or relative humidity using cellulose $\delta^{18}O$ even without the presence of visible annual rings (Anchukaitis et al. 2008; Anchukaitis and Evans 2010).

A preliminary comparison between the published TM-17 record and an unpublished tree ring record from Bidoup Nui Ba National Park (BDNP) in southern Vietnam has shown that the tree ring and stalagmite records align if the TM-17 time series is shifted ~30 years younger (i.e., the TM-17 age model is shifted by ~30 years). The "Strange Parallels" drought from 1756-1768 are captured in both records (highlighted in the TM-17 $\delta^{18}O$ record interpreted as weaker monsoon intensity). However, the ~30 years is outside the 1σ error (~20 years) of the estimated TM-17 age model uncertainty. Therefore, future work entails investigating to what extent karst hydrology and/or in-cave processes may lead to this observed decadal-scale lag between the TM-17 $\delta^{18}O$ record and the BDNP tree ring record. It is possible that since the overburden in the area of the cave where the stalagmite was collected is quite thick (likely > 200 m), the decadal-scale lag may be due to transporting and mixing in part explain this offset. In addition, in-cave processes and parameters, such as drip interval, cave air pCO_2, and/or mixing effects may also play a role part in the 30-year lag between the two records. In Chapter 4, I produced a 1-year lag

by subjectively altering some of the model parameters, though more work is needed to systematically alter the model parameters to produce a longer lag time. More additional cave monitoring data are also needed to further constrain the monthly seasonal variations of the in-cave properties as well.

5.2.4 Integrating Global Climate Models with Proxy System Models

As previously described in Chapter 4, PSMs help to disentangle the uncertainties that still remain when interpreting proxy data. The purpose of these PSMs is to accurately portray the multivariate and nonlinear processes in proxy systems but avoid the unconstrained parameters in full complexity models (Evans et al. 2013). Coupling PSMs to isotope-enabled climate system models or global climate models can enable users to validate model simulations by making a more direct comparison between simulated data using GCM environmental variables (e.g., temperature, precipitation, SSTs) and actual proxy observations (Dee et al. 2015). Comparisons of GCM outputs with observations would also test hypotheses regarding the source of uncertainty between flow routes and hydrological pathways (Baker et al. 2013). Future links of GCMs with PSMs can further our understanding of uncertainties caused by climate variability or hydrological variations in the karst system. In addition, replications of speleothem series from different cave sites would be a powerful tool in identifying discrepancies between climate signals and non-climate noise (Truebe et al. 2010; Baker et al. 2013).

It is important to note that there are inherent caveats with PSMs that will need to be addressed in further studies. For example, PSMs are first-order models that are simplifications of complex systems, which ignore potentially important processes, such as certain pathways not indicated in the model (Bradley et al. 2010; Dee et al. 2015). Forward models are only as

comprehensive as the observations they are based on. Because high-resolution observational records are limited in Laos and the broader Asian monsoon region, PSMs complexity must be altered to avoid assumptions on parameters that cannot be explained via observations. One possible solution would be to create more detailed proxy networks to further constrain PSMs and improve our knowledge on proxies (Dee et al., 2015; Evans et al., 2013). Using a combination of PSMs, such as Karstolution, with global circulation models and large climate models can help better analyze long-term model performance and realistic estimates of variability of $\delta_{18}O$ from the ground surface down to the stalagmites**.** Lastly, working with PSMs provide additional opportunities to facilitate collaborations between climate scientists, modelers, and statisticians to improve the current PSMs and incorporate climate system models (Evans et al. 2013).

References

Adler RF, Huffman GJ, Chang A, et al (2003) The Version-2 Global Precipitation Climatology Project (GPCP) Monthly Precipitation Analysis (1979–Present). J Hydrometeorol 4:1147–1167. https://doi.org/10.1175/1525-7541(2003)004<1147:TVGPCP>2.0.CO;2

Almalki SJ, Nadarajah S (2014) Modifications of the Weibull distribution: A review. Reliab. Eng. Syst. Saf. 124:32–55

Anchukaitis KJ, Evans MN (2010) Tropical cloud forest climate variability and the demise of the Monteverde golden toad. Proc Natl Acad Sci 107:5036–5040. https://doi.org/10.1073/pnas.0908572107

Anchukaitis KJ, Evans MN, Wheelwright NT, Schrag DP (2008) Stable isotope chronology and climate signal calibration in neotropical montane cloud forest trees. J Geophys Res 113:G03030. https://doi.org/10.1029/2007JG000613

Ashouri H, Hsu K-L, Sorooshian S, et al (2015) PERSIANN-CDR: Daily Precipitation Climate Data Record from Multisatellite Observations for Hydrological and Climate Studies. Bull Am Meteorol Soc 96:69–83. https://doi.org/10.1175/BAMS-D-13-00068.1

Asian Development Bank. (2009) The economics of climate change in Southeast Asia : a regional review. Asian Development Bank

Attolini MR, Cecchini S, Galli M, Nanni T (1990) On the persistence of the 22 y solar cycle. Sol Phys 125:389–398. https://doi.org/10.1007/bf00158414

Ayalon A, Bar-Matthews M, Sass E (1998) Rainfall-recharge relationships within a karstic terrain in the Eastern Mediterranean semi-arid region, Israel: δ18O and δD characteristics. J Hydrol 207:18–31. https://doi.org/10.1016/S0022-1694(98)00119-X

Bajo P, Borsato A, Drysdale R, et al (2017) Stalagmite carbon isotopes and dead carbon proportion (DCP) in a near-closed-system situation: An interplay between sulphuric and carbonic acid dissolution. Geochim Cosmochim Acta 210:208–227. https://doi.org/10.1016/J.GCA.2017.04.038

Baker A, Asrat A, Fairchild IJ, et al (2010) Decadal-scale rainfall variability in Ethiopia recorded in an annually laminated, Holocene-age, stalagmite. The Holocene 20:827–836. https://doi.org/10.1177/0959683610365934

Baker A, Bradley C (2010) Modern stalagmite δ18O: Instrumental calibration and forward modelling. Glob Planet Change 71:201–206. https://doi.org/10.1016/j.gloplacha.2009.05.002

Baker A, Bradley C, Phipps SJ (2013) Hydrological modeling of stalagmite $\delta^{18}O$ response to glacial-interglacial transitions. Geophys Res Lett 40:3207–3212. https://doi.org/10.1002/grl.50555

Baker A, Genty D, Fairchild IJ (2000) Hydrological characterisation of stalagmite dripwaters at Grotte de Villars, Dordogne, by the analysis of inorganic species and luminescent organic matter. Hydrol Earth Syst Sci 4:439–449. https://doi.org/10.5194/hess-4-439-2000

Baker A, Ito E, Smart PL, McEwan RF (1997) Elevated and variable values of 13C in speleothems in a British cave system. Chem Geol 136:263–270. https://doi.org/10.1016/S0009-2541(96)00129-5

Baker AJ, Mattey DP, Baldini JUL (2014) Reconstructing modern stalagmite growth from cave monitoring, local meteorology, and experimental measurements of dripwater films. Earth Planet Sci Lett 392:239–249. https://doi.org/10.1016/j.epsl.2014.02.036

Baker AJ, Sodemann H, Baldini JUL, et al (2015) Seasonality of westerly moisture transport in

the East Asian summer monsoon and its implications for interpreting precipitation δ18O. J Geophys Res 120:5850–5862. https://doi.org/10.1002/2014JD022919
Baldini JUL, McDermott F, Baldini LM, et al (2012) Identifying short-term and seasonal trends in cave drip water trace element concentrations based on a daily-scale automatically collected drip water dataset. Chem Geol 330–331:1–16. https://doi.org/10.1016/j.chemgeo.2012.08.009
Baldini JUL, McDermott F, Hoffmann DL, et al (2008) Very high-frequency and seasonal cave atmosphere PCO2 variability: Implications for stalagmite growth and oxygen isotope-based paleoclimate records. Earth Planet Sci Lett 272:118–129. https://doi.org/10.1016/j.epsl.2008.04.031
Bao-Qiang T, Ke F (2012) Relationship between the Late Spring NAO and Summer Extreme Precipitation Frequency in the Middle and Lower Reaches of the Yangtze River. Atmos Ocean Sci Lett 5:455–460. https://doi.org/10.1080/16742834.2012.11447038
Bard E, Raisbeck G, Yiou F, Jouzel J (2000) Solar irradiance during the last 1200 years based on cosmogenic nuclides. Tellus B Chem Phys Meteorol 52:985–992. https://doi.org/10.3402/tellusb.v52i3.17080
Beck JW, Richards DA, Edwards RL, et al (2001) Extremely large variations of atmospheric 14C concentration during the last glacial period. Science (80-) 292:2453–2458. https://doi.org/10.1126/science.1056649
Beck JW, Zhou W, Li C, et al (2018) A 550,000-year record of East Asian monsoon rainfall from10Be in loess. Science (80-) 360:877–881. https://doi.org/10.1126/science.aam5825
Berkelhammer M, Sinha A, Mudelsee M, et al (2010) Persistent multidecadal power of the Indian Summer Monsoon. Earth Planet Sci Lett 290:166–172. https://doi.org/10.1016/j.epsl.2009.12.017
Bird BW, Abbott MB, Vuille M, et al (2011) A 2,300-year-long annually resolved record of the South American summer monsoon from the Peruvian Andes. Proc Natl Acad Sci U S A 108:8583–8. https://doi.org/10.1073/pnas.1003719108
Bradley C, Baker A, Jex CN, Leng MJ (2010) Hydrological uncertainties in the modelling of cave drip-water δ18O and the implications for stalagmite palaeoclimate reconstructions. Quat Sci Rev 29:2201–2214. https://doi.org/10.1016/j.quascirev.2010.05.017
Breitenbach SFM, Rehfeld K, Goswami B, et al (2012) Climate of the Past COnstructing Proxy Records from Age models (COPRA). Clim Past 8:1765–1779. https://doi.org/10.5194/cp-8-1765-2012
Buckley BM, Anchukaitis KJ, Penny D, et al (2010) Climate as a contributing factor in the demise of Angkor, Cambodia. Proc Natl Acad Sci U S A 107:6748–52. https://doi.org/10.1073/pnas.0910827107
Buckley BM, Duangsathaporn K, Palakit K, et al (2007a) Analyses of growth rings of Pinus merkusii from Lao P.D.R. For Ecol Manage 253:120–127. https://doi.org/10.1016/j.foreco.2007.07.018
Buckley BM, Fletcher R, - Yu Simon Wang S, et al (2014) Monsoon extremes and society over the past millennium on mainland Southeast Asia. Quat Sci Rev 95:1–19. https://doi.org/10.1016/j.quascirev.2014.04.022
Buckley BM, Palakit K, Duangsathaporn K, et al (2007b) Decadal scale droughts over northwestern Thailand over the past 448 years: links to the tropical Pacific and Indian Ocean sectors. Clim Dyn 29:63–71. https://doi.org/10.1007/s00382-007-0225-1
Burgers G, Stephenson DB (1999) The “normality” of El Niño. Geophys Res Lett 26:1027–

1030. https://doi.org/10.1029/1999GL900161
Caesar L, Rahmstorf S, Robinson A, et al (2018) Observed fingerprint of a weakening Atlantic Ocean overturning circulation. Nature 556:191–196. https://doi.org/10.1038/s41586-018-0006-5
Cai Y, Fung IY, Edwards RL, et al (2015) Variability of stalagmite-inferred Indian monsoon precipitation over the past 252,000 y. Proc Natl Acad Sci U S A 112:2954–2959. https://doi.org/10.1073/pnas.1424035112
Chadwick R, Boutle I, Martin G (2013) Spatial Patterns of Precipitation Change in CMIP5: Why the Rich Do Not Get Richer in the Tropics. J Clim 26:3803–3822. https://doi.org/10.1175/JCLI-D-12-00543.1
Chang C-P, Wang Z, McBride J, et al (2005) Annual Cycle of Southeast Asia—Maritime Continent Rainfall and the Asymmetric Monsoon Transition. J Clim 18:287–301. https://doi.org/10.1175/JCLI-3257.1
Chawchai S, Chabangborn A, Fritz S, et al (2015) Hydroclimatic shifts in northeast Thailand during the last two millennia – the record of Lake Pa Kho. Quat Sci Rev 111:62–71. https://doi.org/10.1016/j.quascirev.2015.01.007
Chen F, Chen J, Huang W, et al (2019a) Westerlies Asia and monsoonal Asia: Spatiotemporal differences in climate change and possible mechanisms on decadal to sub-orbital timescales. Earth-Science Rev 192:337–354. https://doi.org/10.1016/J.EARSCIREV.2019.03.005
Chen J, Chen F, Feng S, et al (2015) Hydroclimatic changes in China and surroundings during the Medieval Climate Anomaly and Little Ice Age: Spatial patterns and possible mechanisms. Quat Sci Rev 107:98–111. https://doi.org/10.1016/j.quascirev.2014.10.012
Chen J, Rao Z, Liu J, et al (2016) On the timing of the East Asian summer monsoon maximum during the Holocene—Does the speleothem oxygen isotope record reflect monsoon rainfall variability? Sci China Earth Sci 59:2328–2338. https://doi.org/10.1007/s11430-015-5500-5
Chen M, Yu J-Y, Wang X, Jiang W (2019b) The Changing Impact Mechanisms of a Diverse El Niño on the Western Pacific Subtropical High. Geophys Res Lett 46:953–962. https://doi.org/10.1029/2018GL081131
Cheng H, Edwards RL, Broecker WS, et al (2009) Ice age terminations. Science 326:248–52. https://doi.org/10.1126/science.1177840
Cheng H, Edwards RL, Sinha A, et al (2016) The Asian monsoon over the past 640,000 years and ice age terminations. Nature 534:640–646. https://doi.org/10.1038/nature18591
Cheng H, Lawrence Edwards R, Shen C-C, et al (2013) Improvements in 230Th dating, 230Th and 234U half-life values, and U–Th isotopic measurements by multi-collector inductively coupled plasma mass spectrometry. Earth Planet Sci Lett 371–372:82–91. https://doi.org/10.1016/j.epsl.2013.04.006
Cheng H, Sinha A, Wang X, et al (2012a) The Global Paleomonsoon as seen through speleothem records from Asia and the Americas. Clim Dyn 39:1045–1062. https://doi.org/10.1007/s00382-012-1363-7
Cheng H, Zhang PZ, Spötl C, et al (2012b) The climatic cyclicity in semiarid-arid central Asia over the past 500,000 years. Geophys Res Lett 39. https://doi.org/10.1029/2011GL050202
Chiang JCH, Fung IY, Wu C-H, et al (2015) Role of seasonal transitions and westerly jets in East Asian paleoclimate. Quat Sci Rev 108:111–129. https://doi.org/10.1016/J.QUASCIREV.2014.11.009
Christensen JH, Kumar KK, Aldrian E, et al (2013) Climate phenomena and their relevance for future regional climate change. In: Stocker TF (ed) Climate Change 2013: the Physical

Science Basis, Contribution of Working Group I to the Fifth Assessment Report of the Intergovernmental Panel on Climate Change. Cambridge University Press, Cambridge, UK, New York, USA, pp 1217–1308
Clemens S, Prell W, Murray D, et al (1991) Forcing mechanisms of the Indian Ocean monsoon. Nature 353:720–725. https://doi.org/10.1038/353720a0
Cobb KM, Charles CD, Cheng H, Edwards RL (2003) El Niño/Southern Oscillation and tropical Pacific climate during the last millennium. Nature 424:271–6. https://doi.org/10.1038/nature01779
Comas-Bru L, Harrison SP, Werner M, et al (2019) Evaluating model outputs using integrated global speleothem records of climate change since the last glacial. Clim Past 15:1557–1579. https://doi.org/10.5194/cp-15-1557-2019
Conroy JL, Overpeck JT (2011) Regionalization of Present-Day Precipitation in the Greater Monsoon Region of Asia *. J Clim 24:4073–4095. https://doi.org/10.1175/2011JCLI4033.1
Conroy JL, Overpeck JT, Cole JE, et al (2008) Holocene changes in eastern tropical Pacific climate inferred from a Galápagos lake sediment record. Quat Sci Rev 27:1166–1180. https://doi.org/10.1016/j.quascirev.2008.02.015
Conroy JL, Overpeck JT, Cole JE (2010) El Niño/Southern Oscillation and changes in the zonal gradient of tropical Pacific sea surface temperature over the last 1.2 ka The zonal gradient of tropical Pacific SST over the last 1.2 ka
Cook ER, Anchukaitis KJ, Buckley BM, et al (2010) Asian Monsoon Failure and Megadrought During the Last Millennium. Science 328:486–489
Cuthbert MO, Baker A, Jex CN, et al (2014) Drip water isotopes in semi-arid karst: Implications for speleothem paleoclimatology. Earth Planet Sci Lett 395:194–204. https://doi.org/10.1016/j.epsl.2014.03.034
Dansgaard W (1964) Stable isotopes in precipitation. Tellus 16:436–468. https://doi.org/10.1111/j.2153-3490.1964.tb00181.x
Dansgaard W, Johnsen SJ, Clausen HB, et al (1993) Evidence for general instability of past climate from a 250-kyr ice-core record. Nature 364:218–220. https://doi.org/10.1038/364218a0
Day JA, Fung I, Risi C, et al (2015) Coupling of South and East Asian Monsoon Precipitation in July–August. J Clim 28:4330–4356. https://doi.org/10.1175/JCLI-D-14-00393.1
Dayem KE, Molnar P, Battisti DS, Roe GH (2010) Lessons learned from oxygen isotopes in modern precipitation applied to interpretation of speleothem records of paleoclimate from eastern Asia. Earth Planet Sci Lett 295:219–230. https://doi.org/10.1016/j.epsl.2010.04.003
Dee S, Emile-Geay J, Evans MN, et al (2015) PRYSM: An open-source framework for PRoxY System Modeling, with applications to oxygen-isotope systems. J Adv Model Earth Syst 7:1220–1247. https://doi.org/10.1002/2015MS000447
Dee SG, Parsons LA, Loope GR, et al (2017) Improved spectral comparisons of paleoclimate models and observations via proxy system modeling: Implications for multi-decadal variability. Earth Planet Sci Lett 476:34–46. https://doi.org/10.1016/J.EPSL.2017.07.036
Dee SG, Steiger NJ, Emile-Geay J, Hakim GJ (2016) On the utility of proxy system models for estimating climate states over the common era. J Adv Model Earth Syst 8:1164–1179. https://doi.org/10.1002/2016MS000677
Deininger M, Fohlmeister J, Scholz D, Mangini A (2012) Isotope disequilibrium effects: The influence of evaporation and ventilation effects on the carbon and oxygen isotope composition of speleothems - A model approach. Geochim Cosmochim Acta 96:57–79.

https://doi.org/10.1016/j.gca.2012.08.013
Deininger M, Scholz D (2019) ISOLUTION 1.0: an ISOtope evoLUTION model describing the stable oxygen (δ18O) and carbon (δ13C) isotope values of speleothems. Int J Speleol 48:21–32. https://doi.org/10.5038/1827-806X.48.1.2219
Delaygue G, Bard E (2011) An Antarctic view of Beryllium-10 and solar activity for the past millennium. Clim Dyn 36:2201–2218. https://doi.org/10.1007/s00382-010-0795-1
Demény A, Németh P, Czuppon G, et al (2016) Formation of amorphous calcium carbonate in caves and its implications for speleothem research. Sci Rep 6:39602. https://doi.org/10.1038/srep39602
Dietzel M, Tang J, Leis A, Köhler SJ (2009) Oxygen isotopic fractionation during inorganic calcite precipitation - Effects of temperature, precipitation rate and pH. Chem Geol 268:107–115. https://doi.org/10.1016/j.chemgeo.2009.07.015
Ding Y, Chan JCL (2005) The East Asian summer monsoon: An overview. Meteorol. Atmos. Phys. 89:117–142
Ding Y, Wang Z, Sun Y (2008) Inter-decadal variation of the summer precipitation in East China and its association with decreasing Asian summer monsoon. Part I: Observed evidences. Int J Climatol 28:1139–1161. https://doi.org/10.1002/joc.1615
Domínguez-Villar D, Baker A, Fairchild IJ, Edwards RL (2012) A method to anchor floating chronologies in annually laminated speleothems with U–Th dates. Quat Geochronol 14:57–66. https://doi.org/10.1016/J.QUAGEO.2012.04.019
Dorale JA, Edwards RL, Ito E, Gonzalez LA (1998) Climate and Vegetation History of the Midcontinent from 75 to 2 ka: A Speleothem Record from Crevice Cave, Missouri, USA. Science (80-) 282:1871–1874. https://doi.org/10.1126/science.282.5395.1871
Dreybrodt J, Laumanns M (2013) The Unknown North of Laos. (Part 5 - 2012-2013: Karst and Caves of the Provinces Luang Nam Tha, Luang Prabang and Houaphan). Berlin
Dreybrodt J, Laumanns M, Steiner H (2013) Ten years of exploration and over 100km of caves surveyed in Northern Laos. In: UIS Congress Brno. pp 68–70
Dreybrodt W, Deininger M (2014) The impact of evaporation to the isotope composition of DIC in calcite precipitating water films in equilibrium and kinetic fractionation models. Geochim Cosmochim Acta 125:433–439. https://doi.org/10.1016/j.gca.2013.10.004
Dreybrodt W, Scholz D (2011) Climatic dependence of stable carbon and oxygen isotope signals recorded in speleothems: From soil water to speleothem calcite. Geochim Cosmochim Acta 75:734–752. https://doi.org/10.1016/j.gca.2010.11.002
Drysdale R, Zanchetta G, Hellstrom J, et al (2006) Late Holocene drought responsible for the collapse of Old World civilizations is recorded in an Italian cave flowstone. Geology 34:101–104. https://doi.org/10.1130/G22103.1
Du Y, Xie S-P, Huang G, et al (2009) Role of Air–Sea Interaction in the Long Persistence of El Niño–Induced North Indian Ocean Warming*. J Clim 22:2023–2038. https://doi.org/10.1175/2008JCLI2590.1
Duan W, Ruan J, Luo W, et al (2016) The transfer of seasonal isotopic variability between precipitation and drip water at eight caves in the monsoon regions of China medium-variability drips, with constant and relatively low d 18 O d values in the. Geochim Cosmochim Acta 183:250–266. https://doi.org/10.1016/j.gca.2016.03.037
Endo H, Kitoh A (2014) Thermodynamic and dynamic effects on regional monsoon rainfall changes in a warmer climate. Geophys Res Lett 41:1704–1711. https://doi.org/10.1002/2013GL059158

Evans MN, Tolwinski-Ward SE, Thompson DM, Anchukaitis KJ (2013) Applications of proxy system modeling in high resolution paleoclimatology. Quat Sci Rev 76:16–28. https://doi.org/10.1016/j.quascirev.2013.05.024
Fairchild I, Baker A (2012) Speleothem Science: From Process to Past Environments. Oxford
Fairchild IJ, Borsato A, Tooth AF, et al (2000) Controls on trace element (Sr-Mg) compositions of carbonate cave waters: Implications for speleothem climatic records. Chem Geol 166:255–269. https://doi.org/10.1016/S0009-2541(99)00216-8
Fairchild IJ, Smith CL, Baker A, et al (2006a) Modification and preservation of environmental signals in speleothems. Earth-Science Rev 75:105–153. https://doi.org/10.1016/j.earscirev.2005.08.003
Fairchild IJ, Tuckwell GW, Baker A, Tooth AF (2006b) Modelling of dripwater hydrology and hydrogeochemistry in a weakly karstified aquifer (Bath, UK): Implications for climate change studies. J Hydrol 321:213–231. https://doi.org/10.1016/j.jhydrol.2005.08.002
Feng J, Chen W, Tam C-Y, Zhou W (2011) Different impacts of El Niño and El Niño Modoki on China rainfall in the decaying phases. Int J Climatol 31:2091–2101. https://doi.org/10.1002/joc.2217
Feng J, Wang L, Chen W, et al (2014) How Does the East Asian Summer Monsoon Behave in the Decaying Phase of El Niño during Different PDO Phases? J Clim 27:2682–2698. https://doi.org/10.1175/JCLI-D-13-00015.1
Fiorillo F (2009) Spring hydrographs as indicators of droughts in a karst environment. J Hydrol 373:290–301. https://doi.org/10.1016/j.jhydrol.2009.04.034
Fleitmann D, Burns SJ, Mudelsee M, et al (2003) Holocene forcing of the Indian monsoon recorded in a stalagmite from Southern Oman. Science (80-) 300:1737–1739. https://doi.org/10.1126/science.1083130
Fleitmann D, Matter A, Burns SJ, et al (2004) Geology and quaternary climate history of socotra. Fauna Arab 20:27–44
Folland CK, Knight J, Linderholm HW, et al (2009) The Summer North Atlantic Oscillation: Past, Present, and Future. J Clim 22:1082–1103. https://doi.org/10.1175/2008JCLI2459.1
Frappier AB, Sahagian D, Carpenter SJ, et al (2007) Stalagmite stable isotope record of recent tropical cyclone events. Geology 35:111. https://doi.org/10.1130/G23145A.1
Frisia S (2015) Microstratigraphic logging of calcite fabrics in speleothems as tool for palaeoclimate studies. Int J Speleol 1:1–16. https://doi.org/10.5038/1827-806X.44.1.1
Frisia S, Borsato A, Fairchild IJ, McDermott F (2000) Calcite Fabrics, Growth Mechanisms, and Environments of Formation in Speleothems from the Italian Alps and Southwestern Ireland. J Sediment Res 70:1183–1196. https://doi.org/10.1306/022900701183
Frisia S, Fairchild IJ, Fohlmeister J, et al (2011) Carbon mass-balance modelling and carbon isotope exchange processes in dynamic caves. Geochim Cosmochim Acta 75:380–400. https://doi.org/10.1016/j.gca.2010.10.021
Genty D, Baker A, Massault M, et al (2001) Dead carbon in stalagmites: carbonate bedrock paleodissolution vs. ageing of soil organic matter. Implications for 13C variations in speleothems. Geochim Cosmochim Acta 65:3443–3457. https://doi.org/10.1016/S0016-7037(01)00697-4
Genty D, Blamart D, Ouahdi R, Gilmour M (2003) Precise dating of Dansgaard-Oeschger climate oscillations in western Europe from stalagmite data. Feb 20:6925–833
Gong D-Y, Ho C-H (2002) Shift in the summer rainfall over the Yangtze River valley in the late 1970s. Geophys Res Lett 29:78-1-78–4. https://doi.org/10.1029/2001GL014523

Gray LJ, Beer J, Geller M, et al (2010) Solar influences on climate. Rev Geophys 48:RG4001. https://doi.org/10.1029/2009RG000282
Griffiths ML, Drysdale RN, Gagan MK, et al (2009) Increasing Australian-Indonesian monsoon rainfall linked to early Holocene sea-level rise. Nat Geosci 2:636–639. https://doi.org/10.1038/ngeo605
Griffiths ML, Drysdale RN, Gagan MK, et al (2010) Evidence for Holocene changes in Australian-Indonesian monsoon rainfall from stalagmite trace element and stable isotope ratios. Earth Planet Sci Lett 292:27–38. https://doi.org/10.1016/j.epsl.2010.01.002
Griffiths ML, Fohlmeister J, Drysdale RN, et al (2012) Hydrological control of the dead carbon fraction in a Holocene tropical speleothem. Quat Geochronol 14:81–93. https://doi.org/10.1016/j.quageo.2012.04.001
Griffiths ML, Kimbrough AK, Gagan MK, et al (2016) Western Pacific hydroclimate linked to global climate variability over the past two millennia. Nat Commun 7:11719. https://doi.org/10.1038/ncomms11719
Grinsted A, Moore JC, Jevrejeva S (2004) Nonlinear Processes in Geophysics Application of the cross wavelet transform and wavelet coherence to geophysical time series. Nonlinear Process Geophys 11:561–566
Gu W, Li C, Li W, et al (2009) Interdecadal unstationary relationship between NAO and east China's summer precipitation patterns. Geophys Res Lett 36:L13702. https://doi.org/10.1029/2009GL038843
Hammer Ø, Harper DAT, Ryan PD (2001) PAST: Paleontological statistics software package for education and data analysis. 9pp. 4:9
Han J, Zhang R (2009) The dipole mode of the summer rainfall over East China during 1958–2001. Adv Atmos Sci 26:727–735. https://doi.org/10.1007/s00376-009-9014-6
Hartmann A, Baker A (2017) Modelling karst vadose zone hydrology and its relevance for paleoclimate reconstruction. Earth-Science Rev. 172:178–192
Haslett J, Parnell A (2008) A simple monotone process with application to radiocarbon-dated depth chronologies. J R Stat Soc Ser C (Applied Stat 57:399–418. https://doi.org/10.1111/j.1467-9876.2008.00623.x
He C, Lin A, Gu D, et al (2017) Interannual variability of Eastern China Summer Rainfall: the origins of the meridional triple and dipole modes. Clim Dyn 48:683–696. https://doi.org/10.1007/s00382-016-3103-x
He C, Zhou T, Wu B (2015) The key oceanic regions responsible for the interannual variability of the western North Pacific subtropical high and associated mechanisms. J Meteorol Res 29:562–575. https://doi.org/10.1007/s13351-015-5037-3
Held IM, Soden BJ (2006) Robust Responses of the Hydrological Cycle to Global Warming. J Clim 19:5686–5699. https://doi.org/10.1175/JCLI3990.1
Hendy C. (1971) The isotopic geochemistry of speleothems—I. The calculation of the effects of different modes of formation on the isotopic composition of speleothems and their applicability as palaeoclimatic indicators. Geochim Cosmochim Acta 35:801–824. https://doi.org/10.1016/0016-7037(71)90127-X
Hendy CH, Wilson AT (1968) Palaeoclimatic Data from Speleothems. Nature 219:48–51. https://doi.org/10.1038/219048a0
Hsu H-H, Lin S-M, Hsu H-H, Lin S-M (2007) Asymmetry of the Tripole Rainfall Pattern during the East Asian Summer. J Clim 20:4443–4458. https://doi.org/10.1175/JCLI4246.1
Hsu H-H, Liu X (2003) Relationship between the Tibetan Plateau heating and East Asian

summer monsoon rainfall. Geophys Res Lett 30:n/a-n/a. https://doi.org/10.1029/2003GL017909
Hu C, Henderson GM, Huang J, et al (2008) Quantification of Holocene Asian monsoon rainfall from spatially separated cave records. Earth Planet Sci Lett 266:221–232. https://doi.org/10.1016/J.EPSL.2007.10.015
Hu J, Emile-Geay J, Partin J (2017) Correlation-based interpretations of paleoclimate data – where statistics meet past climates. Earth Planet Sci Lett 459:362–371. https://doi.org/10.1016/J.EPSL.2016.11.048
Hu J, Emile-Geay J, Tabor C, et al (2019) Deciphering Oxygen Isotope Records From Chinese Speleothems With an Isotope-Enabled Climate Model. Paleoceanogr Paleoclimatology 2019PA003741. https://doi.org/10.1029/2019PA003741
Hua Q, Cook D, Fohlmeister J, et al (2017) Radiocarbon dating of a speleothem record of paleoclimate for Angkor, Cambodia. Radiocarbon 59:1873–1890. https://doi.org/10.1017/RDC.2017.115
Huang B, Thorne PW, Banzon VF, et al (2017) Extended Reconstructed Sea Surface Temperature, Version 5 (ERSSTv5): Upgrades, Validations, and Intercomparisons. J Clim 30:8179–8205. https://doi.org/10.1175/JCLI-D-16-0836.1
Huang R, Chen J, Wang L, Lin Z (2012) Characteristics, processes, and causes of the spatio-temporal variabilities of the East Asian monsoon system. Adv Atmos Sci 29:910–942. https://doi.org/10.1007/s00376-012-2015-x
Huang R, Liu Y, Feng T (2013) Interdecadal change of summer precipitation over Eastern China around the late-1990s and associated circulation anomalies, internal dynamical causes. Chinese Sci Bull 58:1339–1349. https://doi.org/10.1007/s11434-012-5545-9
Huang X, Pancost RD, Xue J, et al (2018) Response of carbon cycle to drier conditions in the mid-Holocene in central China. Nat Commun 9:. https://doi.org/10.1038/s41467-018-03804-w
Hughes MK (2002) Dendrochronology in climatology – the state of the art. Dendrochronologia 20:95–116. https://doi.org/10.1078/1125-7865-00011
Hurrell JW (1995) Decadal Trends in the North Atlantic Oscillation: Regional Temperatures and Precipitation. Science 269:676 LP – 679. https://doi.org/10.1126/science.269.5224.676
IPCC (2013) Climate Change 2013: The Physical Science Basis. Contribution of Working Group I to the Fifth Assessment Report of the Intergovernmental Panel on Climate Change. In: Stocker, T.F., D. Qin, G.-K. Plattner, M. Tignor, S.K. Allen, J. Boschung, A. Nauels, Y. Xia VB, Midgley and PM (eds). Cambridge University Press, Cambridge, United Kingdom and New York, NY, USA, pp 1–30
IPCC (2007) IPCC, Intergoverbnment Panel on climate Change Impacts, Adaptation and Vulnerability. Cambridge University Press,
Jin D, Hameed SN, Huo L, et al (2016) Recent Changes in ENSO Teleconnection over the Western Pacific Impacts the Eastern China Precipitation Dipole. J Clim 29:7587–7598. https://doi.org/10.1175/JCLI-D-16-0235.1
Johnson KR, Hu C, Belshaw NS, Henderson GM (2006) Seasonal trace-element and stable-isotope variations in a Chinese speleothem: The potential for high-resolution paleomonsoon reconstruction. Earth Planet Sci Lett 244:394–407. https://doi.org/10.1016/j.epsl.2006.01.064
Kalnay E, Kanamitsu M, Kistler R, et al (1996) The NCEP/NCAR 40-Year Reanalysis Project. Bull Am Meteorol Soc 77:437–471. https://doi.org/10.1175/1520-

0477(1996)077<0437:TNYRP>2.0.CO;2
Kathayat G, Cheng H, Sinha A, et al (2016) Indian monsoon variability on millennial-orbital timescales. Sci Rep 6:. https://doi.org/10.1038/srep24374
Kaufmann G (2003a) Stalagmite growth and palaeo-climate: The numerical perspective. Earth Planet Sci Lett 214:251–266. https://doi.org/10.1016/S0012-821X(03)00369-8
Kaufmann G (2003b) Stalagmite growth and palaeo-climate: the numerical perspective. Earth Planet Sci Lett 214:251–266. https://doi.org/10.1016/S0012-821X(03)00369-8
Kay JE, Deser C, Phillips A, et al (2015) The community earth system model (CESM) large ensemble project : A community resource for studying climate change in the presence of internal climate variability. Bull Am Meteorol Soc 96:1333–1349. https://doi.org/10.1175/BAMS-D-13-00255.1
Kim S-T, O'Neil JR (1997) Equilibrium and nonequilibrium oxygen isotope effects in synthetic carbonates. Geochim Cosmochim Acta 61:3461–3475. https://doi.org/10.1016/S0016-7037(97)00169-5
Kitoh A (2017) The Asian Monsoon and its Future Change in Climate Models: A Review. J Meteorol Soc Japan Ser II 95:7–33. https://doi.org/10.2151/jmsj.2017-002
Klein SA, Soden BJ, Lau N-C (1999) Remote Sea Surface Temperature Variations during ENSO: Evidence for a Tropical Atmospheric Bridge. J Clim 12:917–932. https://doi.org/10.1175/1520-0442(1999)012<0917:RSSTVD>2.0.CO;2
Knapp KR (2008) Scientific data stewardship of international satellite cloud climatology project B1 global geostationary observations. J Appl Remote Sens 2:023548. https://doi.org/10.1117/1.3043461
Konecky BL, Russell JM, Rodysill JR, et al (2013) Intensification of southwestern Indonesian rainfall over the past millennium. Geophys Res Lett 40:386–391. https://doi.org/10.1029/2012GL054331
Kong W, Swenson LM, Chiang JCH, et al (2017) Seasonal Transitions and the Westerly Jet in the Holocene East Asian Summer Monsoon. J Clim 30:3343–3365. https://doi.org/10.1175/JCLI-D-16-0087.1
Lachniet MS (2020) Illuminating the Meaning of Asian Monsoon Cave Speleothem Records. Paleoceanogr Paleoclimatology 35:. https://doi.org/10.1029/2019PA003841
Lachniet MS (2009) Climatic and environmental controls on speleothem oxygen-isotope values. Quat Sci Rev 28:412–432. https://doi.org/10.1016/j.quascirev.2008.10.021
Lau K-M, Yang S (1997) Climatology and Interannual Variability of the Southeast Asian Summer Monsoon. Adv Atmos Sci 14:141–162
Lau N-C, Nath MJ (2000) Impact of ENSO on the Variability of the Asian–Australian Monsoons as Simulated in GCM Experiments. J Clim 13:4287–4309. https://doi.org/10.1175/1520-0442(2000)013<4287:IOEOTV>2.0.CO;2
Lau N-C, Nath MJ, Lau N-C, Nath MJ (2003) Atmosphere–Ocean Variations in the Indo-Pacific Sector during ENSO Episodes. J Clim 16:3–20. https://doi.org/10.1175/1520-0442(2003)016<0003:AOVITI>2.0.CO;2
LeGrande AN, Schmidt GA (2009) Sources of Holocene variability of oxygen isotopes in paleoclimate archives. Clim Past 5:441–455. https://doi.org/10.5194/cp-5-441-2009
Linderholm HW, Ou T, Jeong J-H, et al (2011) Interannual teleconnections between the summer North Atlantic Oscillation and the East Asian summer monsoon. J Geophys Res 116:D13107. https://doi.org/10.1029/2010JD015235
Linderholm HW, Seim A, Ou T, et al (2013) Exploring teleconnections between the summer

NAO (SNAO) and climate in East Asia over the last four centuries – A tree-ring perspective. Dendrochronologia 31:297–310. https://doi.org/10.1016/J.DENDRO.2012.08.004
Liu D, Wang Y, Cheng H, et al (2016) Strong coupling of centennial-scale changes of Asian monsoon and soil processes derived from stalagmite d 18 O and d 13 C records, southern China. Quat Res 85:333–346. https://doi.org/10.1016/j.yqres.2016.02.008
Liu W, Huang B, Thorne PW, et al (2015) Extended Reconstructed Sea Surface Temperature Version 4 (ERSST.v4): Part II. Parametric and Structural Uncertainty Estimations. J Clim 28:931–951. https://doi.org/10.1175/JCLI-D-14-00007.1
Macias-Fauria M, Grinsted A, Holopainen J (2012) Persistence matters: Estimation of the statistical significance of paleoclimatic reconstruction statistics from autocorrelated time series. Dendrochronologia 30:179–187. https://doi.org/10.1016/J.DENDRO.2011.08.003
Maher BA, Thompson R (2012) Oxygen isotopes from Chinese caves: records not of monsoon rainfall but of circulation regime. J Quat Sci 27:615–624. https://doi.org/10.1002/jqs.2553
Mann ME, Zhang Z, Rutherford S, et al (2009) Global Signatures and Dynamical Origins of the Little Ice Age and Medieval Climate Anomaly. Science (80-) 326:1256–1260. https://doi.org/10.1126/science.1177303
Mao J, Sun Z, Wu G (2010) 20–50-day oscillation of summer Yangtze rainfall in response to intraseasonal variations in the subtropical high over the western North Pacific and South China Sea. Clim Dyn 34:747–761. https://doi.org/10.1007/s00382-009-0628-2
Markowska M, Baker A, Treble PC, et al (2015) Unsaturated zone hydrology and cave drip discharge water response: Implications for speleothem paleoclimate record variability. J Hydrol 529:662–675. https://doi.org/10.1016/j.jhydrol.2014.12.044
Mason AJ, Henderson GM (2010) Correction of multi-collector-ICP-MS instrumental biases in high-precision uranium-thorium chronology. Int J Mass Spectrom 295:26–35. https://doi.org/10.1016/j.ijms.2010.06.016
Masumoto Y, Meyers G (1998) Forced Rossby waves in the southern tropical Indian Ocean. J Geophys Res Ocean 103:27589–27602. https://doi.org/10.1029/98JC02546
McGregor H V., Evans MN, Goosse H, et al (2015) Robust global ocean cooling trend for the pre-industrial Common Era. Nat Geosci 8:671–677. https://doi.org/10.1038/ngeo2510
Meehl GA, Arblaster JM, Matthes K, et al (2009) Amplifying the Pacific Climate System Response to a Small 11-Year Solar Cycle Forcing. Science 325:1114–1118. https://doi.org/10.1126/science.1172872
Mekong River Commision (2005) Overview of the Hydrology of the Mekong Basin. Mekong River Commission, Vietniane, Noverber. Vientiane
Mickler PJ, Stern LA, Banner JL (2006) Large kinetic isotope effects in modern speleothems. Bull. Geol. Soc. Am. 118:65–81
Mie Z, Sein M, Ogwang BA, et al (2015) Inter - annual variability of Summer Monsoon Rainfall over Myanmar in relation to IOD and ENSO. J Environ Agric Sci 4:28–36
Mischel SA, Scholz D, Spötl C (2015) δ18O values of cave drip water: a promising proxy for the reconstruction of the North Atlantic Oscillation? Clim Dyn 45:3035–3050. https://doi.org/10.1007/s00382-015-2521-5
Misra V, DiNapoli S (2014) The variability of the Southeast Asian summer monsoon. Int J Climatol 34:893–901. https://doi.org/10.1002/joc.3735
Moerman JW, Cobb KM, Partin JW, et al (2014) Transformation of ENSO-related rainwater to dripwater δ18O variability by vadose water mixing. Geophys Res Lett 41:7907–7915.

https://doi.org/10.1002/2014GL061696
Mohtadi M, Prange M, Steinke S (2016) Palaeoclimatic insights into forcing and response of monsoon rainfall. Nature 533:191–199. https://doi.org/10.1038/nature17450
Moy CM, Seltzer GO, Rodbell DT, Anderson DM (2002) Variability of El Nino/Southern Oscillation activity at millennial timescales during the Holocene epoch. Nature 420:162–165. https://doi.org/10.1038/nature01194
Mühlinghaus C, Scholz D, Mangini A (2007) Modelling stalagmite growth and δ13C as a function of drip interval and temperature. Geochim Cosmochim Acta 71:2780–2790. https://doi.org/10.1016/J.GCA.2007.03.018
Mühlinghaus C, Scholz D, Mangini A (2009) Modelling fractionation of stable isotopes in stalagmites. Geochim Cosmochim Acta 73:7275–7289. https://doi.org/10.1016/j.gca.2009.09.010
Neff U, Burns SJ, Mangini A, et al (2001) Strong coherence between solar variability and the monsoon in Oman between 9 and 6 kyr ago. Nature 411:290–293. https://doi.org/10.1038/35077048
Nigam S, Shen H-S (1993) Structure of Oceanic and Atmospheric Low-Frequency Variability over the Tropical Pacific and Indian Oceans. Part I: COADS Observations. J. Clim. 6:657–676
Novello VF, Cruz FW, Karmann I, et al (2012) Multidecadal climate variability in Brazil's Nordeste during the last 3000 years based on speleothem isotope records. Geophys Res Lett 39:. https://doi.org/10.1029/2012GL053936
Novello VF, Vuille M, Cruz FW, et al (2016) Centennial-scale solar forcing of the South American Monsoon System recorded in stalagmites. Sci Rep 6:24762. https://doi.org/10.1038/srep24762
Oppo DW, Rosenthal Y, Linsley BK (2009) 2,000-year-long temperature and hydrology reconstructions from the Indo-Pacific warm pool. Nature 460:1113–1116. https://doi.org/10.1038/nature08233
Oster JL, Montañez IP, Guilderson TP, et al (2010) Modeling speleothem δ13C variability in a central Sierra Nevada cave using 14C and 87Sr/86Sr. Geochim Cosmochim Acta 74:5228–5242. https://doi.org/10.1016/j.gca.2010.06.030
Otto-Bliesner BL, Brady EC, Fasullo J, et al (2016) Climate Variability and Change since 850 CE: An Ensemble Approach with the Community Earth System Model. Bull Am Meteorol Soc 97:735–754. https://doi.org/10.1175/BAMS-D-14-00233.1
PAGES Hyro2k Consortium (2017) Comparing proxy and model estimates of hydroclimate variability and change over the Common Era. Clim Past 13:1851–1900. https://doi.org/10.5194/cp-13-1851-2017
Paterson D, de Jonge MD, Howard DL, et al (2011) The X-ray Fluorescence Microscopy Beamline at the Australian Synchrotron. Struct Microsc Appl Phys Lett 1234:124103. https://doi.org/10.1063/1.3625343
Pathak A, Ghosh S, Martinez JA, et al (2017) Role of Oceanic and Land Moisture Sources and Transport in the Seasonal and Interannual Variability of Summer Monsoon in India. J Clim 30:1839–1859. https://doi.org/10.1175/JCLI-D-16-0156.1
Pausata FSR, Battisti DS, Nisancioglu KH, Bitz CM (2011) Chinese stalagmite δ18O controlled by changes in the Indian monsoon during a simulated Heinrich event. Nat Geosci 4:474–480. https://doi.org/10.1038/ngeo1169
Peterson LC, Haug GH, Hughen KA, Rohl U (2000) Rapid changes in the hydrologic cycle of

the tropical Atlantic during the last glacial. Science (80-) 290:1947–1951. https://doi.org/10.1126/science.290.5498.1947
Qian C, Yu J-Y, Chen G (2014) Decadal summer drought frequency in China: the increasing influence of the Atlantic Multi-decadal Oscillation. Environ Res Lett 9:124004. https://doi.org/10.1088/1748-9326/9/12/124004
Qiu S, Zhou W (2019) Variation in Summer Rainfall over the Yangtze River Region during Warming and Hiatus Periods. Atmosphere (Basel) 10:173. https://doi.org/10.3390/atmos10040173
Raghavan S V., Hur J, Liong SY (2018) Evaluations of NASA NEX-GDDP data over Southeast Asia: present and future climates. Clim Change 148:503–518. https://doi.org/10.1007/s10584-018-2213-3
Ratna S, Ratnam J, Behera S, et al (2017) Validation of the WRF regional climate model over the subregions of Southeast Asia: climatology and interannual variability. Clim Res 71:263–280. https://doi.org/10.3354/cr01445
Richards DA, Dorale JA (2003) Uranium-series chronology and environmental applications of speleothems. In: Uranium-series Geochemistry. De Gruyter Mouton, pp 407–460
Richey JN, Sachs JP (2016) Precipitation changes in the western tropical Pacific over the past millennium. Geology 44:671–674. https://doi.org/10.1130/G37822.1
Riechelmann DFC, Deininger M, Scholz D, et al (2013) Disequilibrium carbon and oxygen isotope fractionation in recent cave calcite: Comparison of cave precipitates and model data. Geochim Cosmochim Acta 103:232–244. https://doi.org/10.1016/j.gca.2012.11.002
Robertson I, Waterhouse J., Barker A., et al (2001) Oxygen isotope ratios of oak in east England: implications for reconstructing the isotopic composition of precipitation. Earth Planet Sci Lett 191:21–31. https://doi.org/10.1016/S0012-821X(01)00399-5
Robock A (2000) Volcanic eruptions and climate. Rev Geophys 38:191–219. https://doi.org/10.1029/1998RG000054
Ryan CG, Siddons DP, Kirkham R, et al (2010) The New Maia Detector System: Methods For High Definition Trace Element Imaging Of Natural Material. In: AIP Conference Proceedings. American Institute of Physics, pp 9–17
Sachs JP, Sachse D, Smittenberg RH, et al (2009) Southward movement of the Pacific intertropical convergence zone AD 1400–1850. Nat Geosci 2:519–525. https://doi.org/10.1038/ngeo554
Sano M, Xu C, Nakatsuka T (2012) A 300-year Vietnam hydroclimate and ENSO variability record reconstructed from tree ring δ18O. J Geophys Res Atmos 117:. https://doi.org/10.1029/2012JD017749
Schneider U, Becker A, Finger P, et al (2014) GPCC's new land surface precipitation climatology based on quality-controlled in situ data and its role in quantifying the global water cycle. Theor Appl Climatol 115:15–40. https://doi.org/10.1007/s00704-013-0860-x
Scholz D, Hoffmann DL (2011) StalAge – An algorithm designed for construction of speleothem age models. Quat Geochronol 6:369–382. https://doi.org/10.1016/j.quageo.2011.02.002
Schulz M, Mudelsee M (2002) REDFIT: estimating red-noise spectra directly from unevenly spaced paleoclimatic time series. Comput Geosci 28:421–426. https://doi.org/10.1016/S0098-3004(01)00044-9
Shen C-C, Lin K, Duan W, et al (2013) Testing the annual nature of speleothem banding. Sci Rep 3:2633. https://doi.org/10.1038/srep02633
Shrivastava S, Kar SC, Sharma AR (2017) Inter-annual variability of summer monsoon rainfall

over Myanmar. Int J Climatol 37:802–820. https://doi.org/10.1002/joc.4741
Sigl M, McConnell JR, Toohey M, et al (2014) Insights from Antarctica on volcanic forcing during the Common Era. Nat Clim Chang 4:693–697. https://doi.org/10.1038/nclimate2293
Sinha A, Berkelhammer M, Stott L, et al (2011a) The leading mode of Indian Summer Monsoon precipitation variability during the last millennium. Geophys Res Lett 38:. https://doi.org/10.1029/2011GL047713
Sinha A, Cannariato KG, Stott LD, et al (2007) A 900-year (600 to 1500 A.D.) record of the Indian summer monsoon precipitation from the core monsoon zone of India. Geophys Res Lett 34:. https://doi.org/10.1029/2007GL030431
Sinha A, Stott L, Berkelhammer M, et al (2011b) A global context for megadroughts in monsoon Asia during the past millennium. Quat Sci Rev 30:47–62. https://doi.org/10.1016/j.quascirev.2010.10.005
Solanki SK, Usoskin IG, Kromer B, et al (2004) Unusual activity of the Sun during recent decades compared to the previous 11,000 years. Nature 431:1084–1087. https://doi.org/10.1038/nature02995
Solomon S, Qin D, Manning M, et al (2007) Frequently Asked Questions and Selected Technical Summary Boxes Part of the Working Group I contribution to the Fourth Assessment Report of the Intergovernmental Panel on Climate Change The Physical Science Basis
Spötl C, Boch R (2012) Uranium series dating of speleothems. In: Encyclopedia of Caves. Elsevier Inc., pp 838–844
Spötl C, Fairchild IJ, Tooth AF (2005) Cave air control on dripwater geochemistry, Obir Caves (Austria): Implications for speleothem deposition in dynamically ventilated caves. Geochim Cosmochim Acta 69:2451–2468. https://doi.org/10.1016/j.gca.2004.12.009
Steinman BA, Abbott MB, Nelson DB, et al (2013) Isotopic and hydrologic responses of small, closed lakes to climate variability: Comparison of measured and modeled lake level and sediment core oxygen isotope records. Geochim Cosmochim Acta 105:455–471. https://doi.org/10.1016/j.gca.2012.11.026
Stuiver M, Reimer PJ, Bard E, et al (1998) INTCAL98 RADIOCARBON AGE CALIBRATION, 24,000-0 cal BP. 40:1041–1083. https://doi.org/10.1017/S0033822200019123
Sui C-H, Chung P-H, Li T (2007) Interannual and interdecadal variability of the summertime western North Pacific subtropical high. Geophys Res Lett 34:L11701. https://doi.org/10.1029/2006GL029204
Sui Y, Jiang D, Tian Z (2013) Latest update of the climatology and changes in the seasonal distribution of precipitation over China. Theor Appl Climatol 113:599–610. https://doi.org/10.1007/s00704-012-0810-z
Sun B, Wang H (2015) Inter-decadal transition of the leading mode of inter-annual variability of summer rainfall in East China and its associated atmospheric water vapor transport. Clim Dyn 44:2703–2722. https://doi.org/10.1007/s00382-014-2251-0
Sun J, Wang H, Yuan W (2008) Decadal variations of the relationship between the summer North Atlantic Oscillation and middle East Asian air temperature. J Geophys Res 113:D15107. https://doi.org/10.1029/2007JD009626
Sung M-K, Kwon W-T, Baek H-J, et al (2006) A possible impact of the North Atlantic Oscillation on the east Asian summer monsoon precipitation. Geophys Res Lett 33:L21713. https://doi.org/10.1029/2006GL027253
Tan L, Cai Y, Cheng H, et al (2018) High resolution monsoon precipitation changes on

southeastern Tibetan Plateau over the past 2300 years. Quat Sci Rev 195:122–132. https://doi.org/10.1016/J.QUASCIREV.2018.07.021
Tan L, Cai Y, Yi L, et al (2008) Precipitation variations of Longxi, northeast margin of Tibetan Plateau since AD 960 and their relationship with solar activity
Tan L, Shen CC, Löwemark L, et al (2019) Rainfall variations in central Indo-Pacific over the past 2,700 y. Proc Natl Acad Sci U S A 116:17201–17206. https://doi.org/10.1073/pnas.1903167116
Tan M (2014) Circulation effect: response of precipitation d 18 O to the ENSO cycle in monsoon regions of China. Clim Dyn 42:1067–1077. https://doi.org/10.1007/s00382-013-1732-x
Thirumalai K, DiNezio PN, Okumura Y, Deser C (2017) Extreme temperatures in Southeast Asia caused by El Niño and worsened by global warming. Nat Commun 8:15531. https://doi.org/10.1038/ncomms15531
Tierney JE, Oppo DW, Rosenthal Y, et al (2010) Coordinated hydrological regimes in the Indo-Pacific region during the past two millennia. Paleoceanography 25:. https://doi.org/10.1029/2009PA001871
Tooth AF, Fairchild IJ (2003) Soil and karst aquifer hydrological controls on the geochemical evolution of speleothem-forming drip waters, Crag Cave, southwest Ireland. J Hydrol 273:51–68. https://doi.org/10.1016/S0022-1694(02)00349-9
Torrence C, Compo GP, Torrence C, Compo GP (1998) A Practical Guide to Wavelet Analysis. Bull Am Meteorol Soc 79:61–78. https://doi.org/10.1175/1520-0477(1998)079<0061:APGTWA>2.0.CO;2
Treble PC, Bradley C, Wood A, et al (2013) An isotopic and modelling study of flow paths and storage in Quaternary calcarenite, SW Australia: implications for speleothem paleoclimate records. Quat Sci Rev 64:90–103. https://doi.org/10.1016/j.quascirev.2012.12.015
Treble PC, Fairchild IJ, Griffiths A, et al (2015) Impacts of cave air ventilation and in-cave prior calcite precipitation on Golgotha Cave dripwater chemistry, southwest Australia. Quat Sci Rev 127:61–72. https://doi.org/10.1016/j.quascirev.2015.06.001
Treble PC, Mah M, Griffiths A, et al (2019) Separating isotopic impacts of karst and in-cave processes from climate variability using an integrated speleothem isotope-enabled forward model. EarthArXiv. https://doi.org/10.31223/osf.io/j4kn6
Truebe SA, Ault TR, Cole JE (2010) A forward model of cave dripwater δ18O and application to speleothem records. IOP Conf Ser Earth Environ Sci 9:012022. https://doi.org/10.1088/1755-1315/9/1/012022
Tsai C, Behera SK, Waseda T, Yamagata T (2015) Indo-China Monsoon Indices. Sci Rep 5:8107. https://doi.org/10.1038/srep08107
Ueda H, Iwai A, Kuwako K, Hori ME (2006) Impact of anthropogenic forcing on the Asian summer monsoon as simulated by eight GCMs. Geophys Res Lett 33:L06703. https://doi.org/10.1029/2005GL025336
Vieira LEA, Solanki SK, Krivova NA, Usoskin I (2011) Evolution of the solar irradiance during the Holocene. Astron Astrophys 531:A6. https://doi.org/10.1051/0004-6361/201015843
Wackerbarth A, Langebroek PM, Werner M, et al (2012) Climate of the Past Simulated oxygen isotopes in cave drip water and speleothem calcite in European caves. 8:1781–1799. https://doi.org/10.5194/cp-8-1781-2012
Wackerbarth A, Scholz D, Fohlmeister J, Mangini A (2010) Modelling the δ18O value of cave drip water and speleothem calcite. Earth Planet Sci Lett 299:387–397. https://doi.org/10.1016/j.epsl.2010.09.019

Wang B, Clemens SC, Liu P (2003) Contrasting the Indian and East Asian monsoons: implications on geologic timescales. Mar Geol 201:5–21. https://doi.org/10.1016/S0025-3227(03)00196-8
Wang B, LinHo, Wang B, LinHo (2002) Rainy Season of the Asian–Pacific Summer Monsoon*. J Clim 15:386–398. https://doi.org/10.1175/1520-0442(2002)015<0386:RSOTAP>2.0.CO;2
Wang B, Wu R, Fu X, et al (2000) Pacific–East Asian Teleconnection: How Does ENSO Affect East Asian Climate? J Clim 13:1517–1536. https://doi.org/10.1175/1520-0442(2000)013<1517:PEATHD>2.0.CO;2
Wang B, Wu R, Lau K-M, et al (2001a) Interannual Variability of the Asian Summer Monsoon: Contrasts between the Indian and the Western North Pacific–East Asian Monsoons*. J Clim 14:4073–4090. https://doi.org/10.1175/1520-0442(2001)014<4073:IVOTAS>2.0.CO;2
Wang B, Xiang B, Lee J-Y (2013) Subtropical high predictability establishes a promising way for monsoon and tropical storm predictions. Proc Natl Acad Sci U S A 110:2718–22. https://doi.org/10.1073/pnas.1214626110
Wang JK, Johnson KR, Borsato A, et al (2019) Hydroclimatic variability in Southeast Asia over the past two millennia. Earth Planet Sci Lett 525:. https://doi.org/10.1016/j.epsl.2019.115737
Wang L, Chen W, Huang R (2008a) Interdecadal modulation of PDO on the impact of ENSO on the east Asian winter monsoon. Geophys Res Lett 35:L20702. https://doi.org/10.1029/2008GL035287
Wang P, Clemens S, Beaufort L, et al (2005a) Evolution and variability of the Asian monsoon system: state of the art and outstanding issues. Quat Sci Rev 24:595–629. https://doi.org/10.1016/J.QUASCIREV.2004.10.002
Wang X, Wang C, Zhou W, et al (2011) Teleconnected influence of North Atlantic sea surface temperature on the El Niño onset. Clim Dyn 37:663–676. https://doi.org/10.1007/s00382-010-0833-z
Wang X, Wang D, Zhou W, Li C (2012a) Interdecadal modulation of the influence of La Niña events on mei-yu rainfall over the Yangtze River valley. Adv Atmos Sci 29:157–168. https://doi.org/10.1007/s00376-011-1021-8
Wang Y, Cheng H, Edwards RL, et al (2008b) Millennial- and orbital-scale changes in the East Asian monsoon over the past 224,000 years. Nature 451:1090–1093. https://doi.org/10.1038/nature06692
Wang Y, Cheng H, Edwards RL, et al (2005b) The Holocene Asian monsoon: links to solar changes and North Atlantic climate. Science 308:854–7. https://doi.org/10.1126/science.1106296
Wang YJ, Cheng H, Edwards RL, et al (2001b) A high-resolution absolute-dated late Pleistocene Monsoon record from Hulu Cave, China. Science 294:2345–8. https://doi.org/10.1126/science.1064618
Wang Z, Chang C-P, Wang Z, Chang C-P (2012b) A Numerical Study of the Interaction between the Large-Scale Monsoon Circulation and Orographic Precipitation over South and Southeast Asia. J Clim 25:2440–2455. https://doi.org/10.1175/JCLI-D-11-00136.1
Wang Z, Yang S, Lau N-C, et al (2018) Teleconnection between Summer NAO and East China Rainfall Variations: A Bridge Effect of the Tibetan Plateau. J Clim 31:6433–6444. https://doi.org/10.1175/JCLI-D-17-0413.1
Webster PJ, Magaña VO, Palmer TN, et al (1998) Monsoons: Processes, predictability, and the

prospects for prediction. J Geophys Res Ocean 103:14451–14510. https://doi.org/10.1029/97JC02719
Wong CI, Breecker DO (2015) Advancements in the use of speleothems as climate archives. Quat Sci Rev 127:1–18. https://doi.org/10.1016/J.QUASCIREV.2015.07.019
Wu B, Li T, Zhou T, et al (2010) Relative Contributions of the Indian Ocean and Local SST Anomalies to the Maintenance of the Western North Pacific Anomalous Anticyclone during the El Niño Decaying Summer*. J Clim 23:2974–2986. https://doi.org/10.1175/2010JCLI3300.1
Wu B, Zhou T (2008) Oceanic origin of the interannual and interdecadal variability of the summertime western Pacific subtropical high. Geophys Res Lett 35:L13701. https://doi.org/10.1029/2008GL034584
Wu B, Zhou T, Li T, et al (2009) Seasonally Evolving Dominant Interannual Variability Modes of East Asian Climate*. J Clim 22:2992–3005. https://doi.org/10.1175/2008JCLI2710.1
Wu R, Hu Z-Z, Kirtman BP, et al (2003) Evolution of ENSO-Related Rainfall Anomalies in East Asia. J Clim 16:3742–3758. https://doi.org/10.1175/1520-0442(2003)016<3742:EOERAI>2.0.CO;2
Xie S-P, Annamalai H, Schott FA, McCreary JP (2002) Structure and Mechanisms of South Indian Ocean Climate Variability*. J Clim 15:864–878. https://doi.org/10.1175/1520-0442(2002)015<0864:SAMOSI>2.0.CO;2
Xie S-P, Du Y, Huang G, et al (2010) Decadal Shift in El Niño Influences on Indo–Western Pacific and East Asian Climate in the 1970s*. J Clim 23:3352–3368. https://doi.org/10.1175/2010JCLI3429.1
Xie S-P, Hu K, Hafner J, et al (2009) Indian Ocean Capacitor Effect on Indo–Western Pacific Climate during the Summer following El Niño. J Clim 22:730–747. https://doi.org/10.1175/2008JCLI2544.1
Xie S-P, Kosaka Y, Du Y, et al (2016) Indo-western Pacific ocean capacitor and coherent climate anomalies in post-ENSO summer: A review. Adv Atmos Sci 33:411–432. https://doi.org/10.1007/s00376-015-5192-6
Xu C, Sano M, Nakatsuka T (2011) Tree ring cellulose δ18O of Fokienia hodginsii in northern Laos: A promising proxy to reconstruct ENSO? J Geophys Res Atmos 116:. https://doi.org/10.1029/2011JD016694
Yamoah KA, Chabangborn A, Chawchai S, et al (2016a) A 2000-year leaf wax-based hydrogen isotope record from Southeast Asia suggests low frequency ENSO-like teleconnections on a centennial timescale. Quat Sci Rev 148:44–53. https://doi.org/10.1016/j.quascirev.2016.07.002
Yamoah KKA, Chabangborn A, Chawchai S, et al (2016b) Large variability in n-alkane δ13C values in Lake Pa Kho (Thailand) driven by wetland wetness and aquatic productivity. Org Geochem 97:53–60. https://doi.org/10.1016/j.orggeochem.2016.04.008
Yan H, Sun L, Oppo DW, et al (2011) South China Sea hydrological changes and Pacific Walker Circulation variations over the last millennium. Nat Commun 2:293. https://doi.org/10.1038/ncomms1297
Yan H, Wei W, Soon W, et al (2015) Dynamics of the intertropical convergence zone over the western Pacific during the Little Ice Age. Nat Geosci 8:315–320
Yang H (2016) Investigating the Impacts of Climate, Hydrology, and Asian Monsoon Intensity on a 13 kyr Speleothem Record from Laos
Yang H, Johnson KR, Griffiths ML, Yoshimura K (2016) Interannual controls on oxygen isotope

variability in Asian monsoon precipitation and implications for paleoclimate reconstructions. J Geophys Res Atmos 121:8410–8428. https://doi.org/10.1002/2015JD024683
Yang J, Liu Q, Xie S-P, et al (2007) Impact of the Indian Ocean SST basin mode on the Asian summer monsoon. Geophys Res Lett 34:L02708. https://doi.org/10.1029/2006GL028571
Yang S, Lau K-M, Yoo S-H, et al (2004) Upstream Subtropical Signals Preceding the Asian Summer Monsoon Circulation. J Clim 17:4213–4229. https://doi.org/10.1175/JCLI3192.1
Yatagai A, Kamiguchi K, Arakawa O, et al (2012) APHRODITE: Constructing a Long-Term Daily Gridded Precipitation Dataset for Asia Based on a Dense Network of Rain Gauges. Bull Am Meteorol Soc 93:1401–1415. https://doi.org/10.1175/BAMS-D-11-00122.1
Ye H, Lu R (2012) Dominant patterns of summer rainfall anomalies in East China during 1951–2006. Adv Atmos Sci 29:695–704. https://doi.org/10.1007/s00376-012-1153-5
Yoshimura K, Kanamitsu M, Noone D, Oki T (2008) Historical isotope simulation using Reanalysis atmospheric data. J Geophys Res 113:D19108. https://doi.org/10.1029/2008JD010074
Yu B, Zwiers FW (2010) Changes in equatorial atmospheric zonal circulations in recent decades. Geophys Res Lett 37:5701. https://doi.org/10.1029/2009GL042071
Yuan D (2004) Timing, Duration, and Transitions of the Last Interglacial Asian Monsoon. Science 304:575–578. https://doi.org/10.1126/science.1091220
Zhang, Brahim, Li, et al (2019) The Asian Summer Monsoon: Teleconnections and Forcing Mechanisms—A Review from Chinese Speleothem δ18O Records. Quaternary 2:26. https://doi.org/10.3390/quat2030026
Zhang H, Griffiths ML, Chiang JCH, et al (2018a) East Asian hydroclimate modulated by the position of the westerlies during Termination I. Science 362:580–583. https://doi.org/10.1126/science.aat9393
Zhang H, Griffiths ML, Chiang JCH, et al (2018b) East Asian hydroclimate modulated by the position of the westerlies during Termination I. Science (80-) 362:580–583. https://doi.org/10.1126/science.aat9393
Zhang P, Cheng H, Edwards RL, et al (2008) A test of climate, sun, and culture relationships from an 1810-year Chinese cave record. Science 322:940–942. https://doi.org/10.1126/science.1163965
Zhao K, Wang Y, Edwards RL, et al (2016) Contribution of ENSO variability to the East Asian summer monsoon in the late Holocene. Palaeogeogr Palaeoclimatol Palaeoecol 449:510–519. https://doi.org/10.1016/j.palaeo.2016.02.044
Zhao K, Wang Y, Edwards RL, et al (2015) A high-resolved record of the Asian Summer Monsoon from Dongge Cave, China for the past 1200 years. Quat Sci Rev 122:250–257. https://doi.org/10.1016/j.quascirev.2015.05.030
Zhou T, Gong D, Li J, Li B (2009) Detecting and understanding the multi-decadal variability of the East Asian Summer Monsoon – Recent progress and state of affairs. Meteorol Zeitschrift 18:455–467. https://doi.org/10.1127/0941-2948/2009/0396
Zhu J, Liu Z, Brady E, et al (2017) Reduced ENSO variability at the LGM revealed by an isotope-enabled Earth system model. Geophys Res Lett 44:6984–6992. https://doi.org/10.1002/2017GL073406
Zuo J-Q, Wei-Jing L, Ren H-L, Chen L-J (2012) Change of the Relationship Between the Spring NAO and East Asian Summer Monsoon and Its Possible Mechanism. Chinese J Geophys 55:23–34. https://doi.org/10.1002/cjg2.1697

Appendix A

Supporting information for Ch 2: Hydroclimatic variability in Southeast Asia over the last two millennia

Supplementary Text: Cave setting and speleothem sample

Tham Doun Mai cave (TM cave) is a ~3,745 m-long cave located at ca. 352 m above sea level, adjacent to the Nam Ou river in Luang Prabang Province, Laos (20°45'N, 102°39'E). TM cave was extensively surveyed by members of the Northern Lao-European Cave Project in 2012 (Dreybrodt et al. 2013) and has only a single small (1.5 x 2 m) known entrance. The main portions of the cave are separated from a smaller entrance chamber by a short narrow crawl. The cave is formed in a Late Paleozoic limestone karst massif that rises several hundred meters above the river level. The overlying terrain is extremely steep and difficult to access, so has not likely been impacted by anthropogenic factors, such as deforestation. The thickness of bedrock overlying the cave varies from a few meters close to the entrance up to hundreds of meters in the deepest sections.

Cave monitoring conducted at TM cave includes temperature (T), relative humidity (RH), drip rate, and pCO_2 measurements, as well as collection of drip water and modern calcite samples for geochemical analysis. Results indicate that the temperature in TM cave is ~22 °C (close to the expected mean surface temperature) and the RH is >95%. Drip rates measured at two sites using Stalagmate automated drip loggers show strong seasonality, with rapid increases in drip rate at the onset of the summer monsoon season, indicating a piston flow-like hydrologic response to rain events (Tooth and Fairchild 2003). Cave air pCO_2 is ~600 ppm, though we have only made these measurements between January and March, so cannot rule out the possibility of

seasonal changes in cave ventilation. The average $\delta_{18}O$ of drip water samples taken from several locations in the cave between December 2010 and March 2017 is -7.8 ± 0.9 ‰ (n = 67), close to the weighted annual mean precipitation $\delta_{18}O$ of -8.2 ‰ simulated for our site using the IsoGSM isotope enabled climate model (Yoshimura et al. 2008). This suggests a mixing/transit time of at least one year before the drip water reaches the cave. The average $\delta_{18}O$ of modern calcite grown by placing glass plates under active drips for a period of at least one year is -8.7 ± 0.3 (n=40), samples close to the plate center range between -9 and -9.5 ‰, within the range of the predicted equilibrium values (Kim and O'Neil 1997).

Stalagmite TM-17 (Figure. 1) was collected on a steep slope approximately ~200 m from the entrance, ~half way down the 26 m drop from the upper level to the active river passage. TM-17 was no longer an active stalagmite when collected, so no monitoring was possible on this specific drip site, though drip water and modern calcite samples were collected from other nearby sites. The regular and constant morphology of the TM-17 stalagmite in the investigated topmost section suggests a slow and almost constant drip rate (Kaufmann 2003b), likely preventing the possible influence of differential kinetic fractionation on the $\delta_{13}C$ signal as a function of fluctuating drip rates (Mühlinghaus et al. 2009). Petrographic logging of TM-17 following the rationale in Frisia et al. (Frisia et al. 2000) and the methodology described in Frisia et al. (Frisia 2015) show that it is primarily composed of columnar calcite, ranging from compact to porous. While speleothem $\delta_{18}O$ values could reflect occurrence of non-classical crystallization pathways, which include the precipitation of amorphous carbonate or vaterite (Demény et al. 2016), for TM-17 this effect is unlikely because *in situ* precipitation experiments from freshly collected drip water near the TM-17 sampling site yielded exclusively calcite. By considering that crystallization processes and speleothem growth had a negligible effect in driving $\delta_{18}O$

changes and that any kinetic effects were relatively minor and constant, we assume that TM-17 $\delta_{18}O$ variations are primarily driven by change in mean precipitation $\delta_{18}O$ and $\delta_{13}C$ variations are primarily driven by soil and vegetation responses to changing water balance.

Supplementary Text: Spectral and Wavelet Analyses

To detect decadal to centennial cycles in the TM-17 record, we performed a red-noise power spectral analysis (REDFIT) (Schulz and Mudelsee 2002) specifically adapted for unevenly-spaced data (Figure. S3) using the PAST software (Hammer et al. 2001). The results highlight decadal to centennial-scale periodicities (193, 128, 29 and 9 years) in the TM-17 $\delta_{18}O$ record that are significant above a red-noise background of a first-order autoregressive process (Figure A.2). Additional spectra performed from age models generated via Monte-Carlo simulations in the COPRA1.0 model (Breitenbach et al. 2012) also show significant multidecadal-centennial cycles thus confirming the robustness of the TM-17 $\delta_{18}O$ periodicities. Wavelet transform analysis (Torrence et al. 1998) of the $\delta_{18}O$ record also indicates significant multidecadal to centennial-scale variability throughout the record (Figure. S2). These observed periodicities may be associated with those of known solar cycles, such as the sub-harmonics of the de Vries-Suess (~210 years) (Stuiver et al. 1998) and the Hale (~132 years) (Attolini et al. 1990) solar cycles. However, we are cautious in interpreting the results from the spectra to suggest causation and cannot completely rule out the possible influence of internal coupled climate modes such as the ENSO (Zhao et al. 2015) or AMO (Berkelhammer et al. 2010). Power spectral analysis of the $\delta_{13}C$ data reveals periodicities centered at 386, 66-77, 37 years (significant at 95% confidence level) and these periodicities are supported by wavelet transform analysis (Figure. A.2).

Supplementary Methods

Supplementary Methods: Synchrotron radiation X-ray fluorescence

Synchrotron radiation X-ray fluorescence (XRF) microscopy was performed on the XFM beamline at the Australian Synchrotron (Paterson et al. 2011) using the Kirkpatrick-Baez mirror microprobe end-station. A 12 mm-thick polished slab was analyzed with a monochromatic 2 μm beam spot size and energy at 18.5 keV. A 45 x 2 mm map was acquired in the axial part of the stalagmite at 2 μm pixel size resolution on both axis and a dwell time of 1.2 ms/pixel, yielding a detection limit for Sr of ~ 2 ppm. Single element foils Mn, Fe and Pt (Micromatter, Canada) were utilized as references to calibrate the final elemental spectra. The Maia XRF spectral data were analyzed using the GeoPIXE software suite which uses a fundamental parameters approach, with spectral deconvolution and imaging using the dynamic analysis method. Spectra were fitted using X-ray line relative intensities that reflect integration of yields and X-ray self-absorption effects for the calcite matrix and the contrasting efficiency characteristics across the detector array (Ryan et al. 2010).

Supplementary Methods: Age Model

Annual laminae counting was conducted on the Sr synchrotron XRF map clustered at 4 μm resolution by visually identifying the Sr minima using ImageJ. The corrugated nature of the lamination and the presence of blurred areas centered along crystal boundaries prevented the use of automated laminae counting techniques. Two separate continuous counts were made following the areas with sharper definition on the map (Figure 1), whereas in condensed and blurred intervals up to four different counts were made. The final laminae number was calculated with the arithmetic average on successive sections of the map. The total counting error, C,

between replicate counts was 23 years, whereas an error of 54 years was estimated for the presence of fuzzy areas in which the lamination is not completely clear (F). The total laminae counting error (LC) was calculated as: $LC = \sqrt{C^2 + F^2}$ (Domínguez-Villar et al. 2012). The calculated LC error of 58.7 years amounts to ~3% of the total layers counted (1,934).

Due to the fact that TM-17 was not active upon collection and the laminae counting age model is therefore floating, we anchored the laminae counting age model to the U-Th ages using a least-squares fit method (Domínguez-Villar et al. 2012). One U-Th age (TM-17 U3) was excluded during application of this method due to the large uncertainty on the raw age, which indicates a poor analysis. We determined the top age by calculating the linear regression of the relative laminae number versus the U-Th ages by using least squares fitting. The slope of the regression (0.98, with a 95% confidence range of 0.95 and 1.02) is indistinguishable from 1 and confirms the annual nature of the Sr laminae. The errors in the age model were constructed from the individual U-Th 2σ error bars by propagating the calculated LC error of 3% within each section between two adjacent U-Th ages. Based on this method, the average age uncertainty throughout the record is 26 years. In summary, the final TM-17 chronology is constrained by the six uranium-thorium (U-Th) dates coupled with annual laminae in Sr measured using a least-squares fit method to the U-Th dates (Table A.1 and Figure 1).

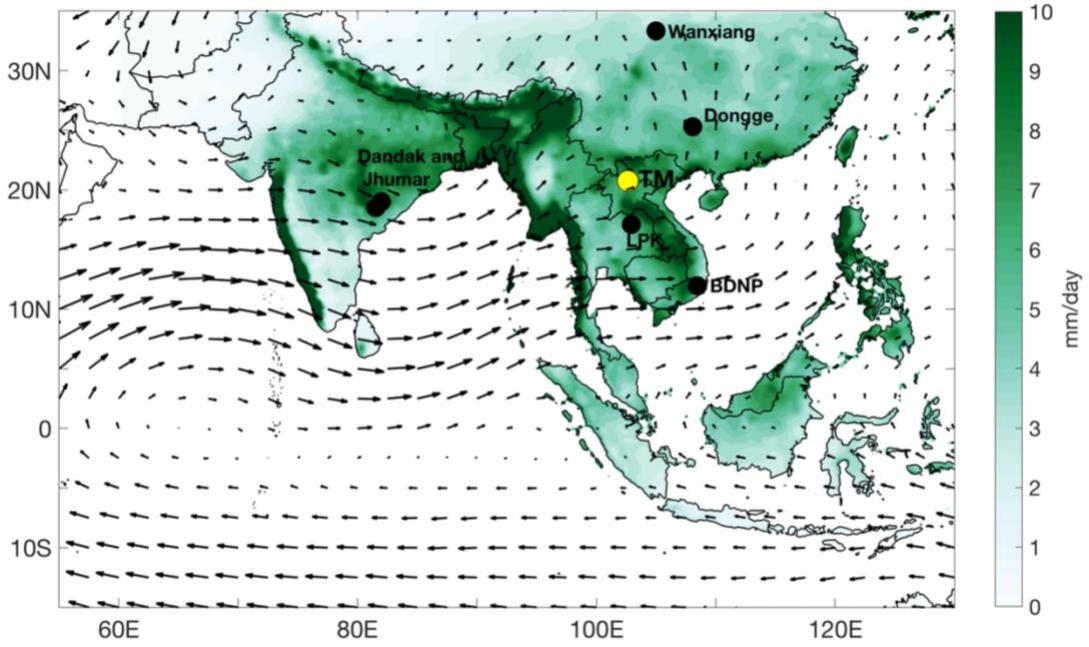

Figure A.1. Summer (JJAS) precipitation and 850 mb winds climatology and location of select paleoclimate records. Mean JJAS precipitation (1951-2007 CE) derived from Asian Precipitation - Highly-Resolved Observational Data Integration Towards Evaluation (APHRODITE) (Yatagai et al. 2012). 850 mb winds are derived from NCEP Reanalysis mean (1951-2007 CE) (Kalnay et al. 1996). The location of Tham Doun Mai Cave, Laos is indicated by the yellow circle. The locations of select regional paleoclimate records marked by black circles. These include Wanxiang Cave, China (Zhang et al. 2008), Dongge Cave, China (Zhao et al. 2015), Dandak and Jhumar Caves, India (Sinha et al. 2007), Bidoup Nui Ba National Park (BDNP) in Southern Vietnam (Buckley et al. 2010), and Lake Pa Kho, Thailand (Chawchai et al. 2015; Yamoah et al. 2016a).

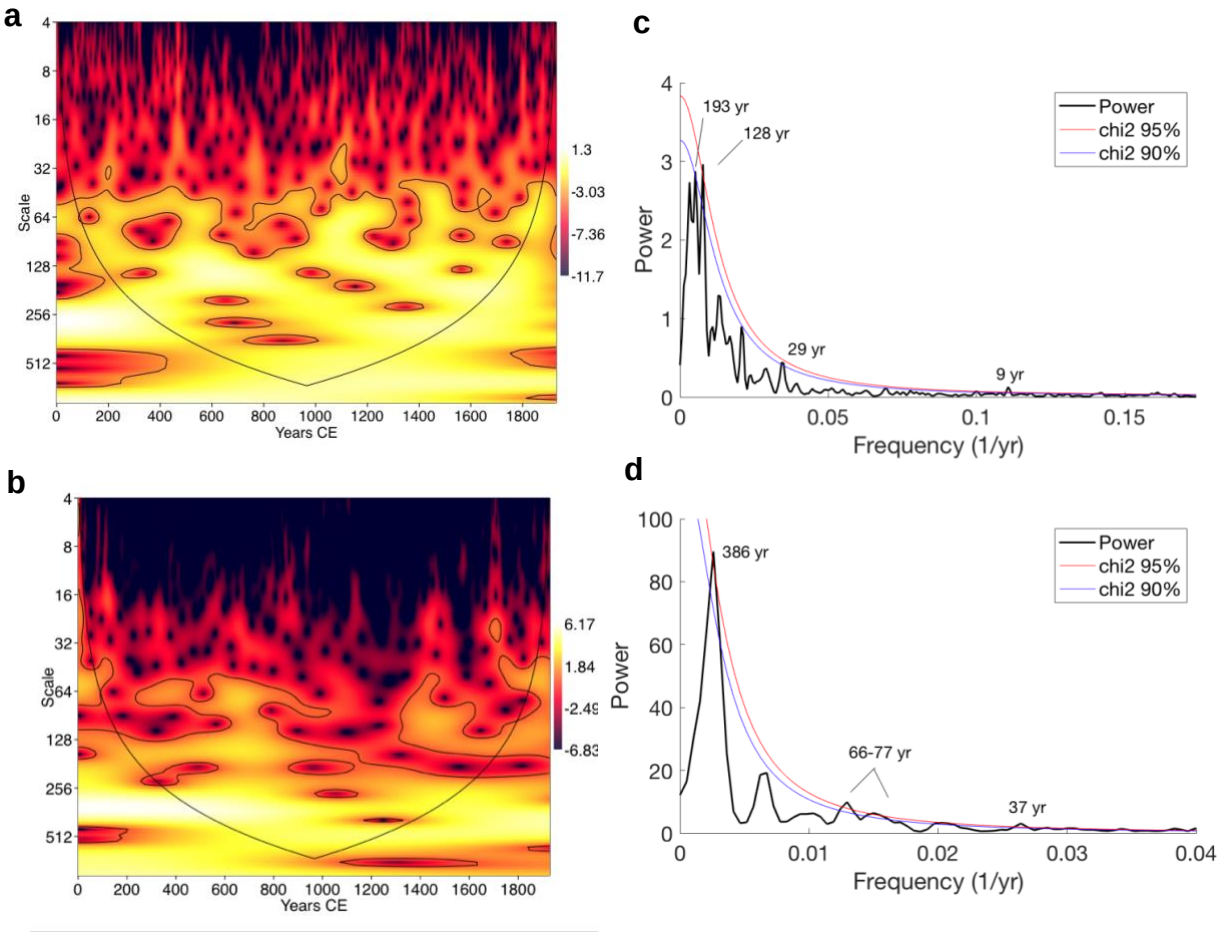

Figure A.2. Morlet wavelet analysis performed using the software PAST (Hammer et al. 2001) and the spectral analysis of TM-17 $\delta_{18}O$ and $\delta_{13}C$ performed with the REDFIT method (Schulz and Mudelsee 2002). (a) $\delta_{18}O$ and (b) $\delta_{13}C$ wavelet transform from colors ranging from deep purple (weak) to bright yellow (strong). The TM-17 data were interpolated to a 2-year timescale using MATLAB interp1 function. Black lines indicate 95% significance level and the cone of influence. (c) $\delta_{18}O$ and (d) $\delta_{13}C$ spectral power performed by REDFIT (Schulz and Mudelsee 2002), which uses the Lomb-Scargle Fourier Transform for unevenly spaced data. The black line indicates the power spectrum. The blue and red lines represent the 95% and 90% confidence limits, respectively, relative to the red-noise spectrum. The utilized parameters were window: welch; oversample: 2; segment: 4.

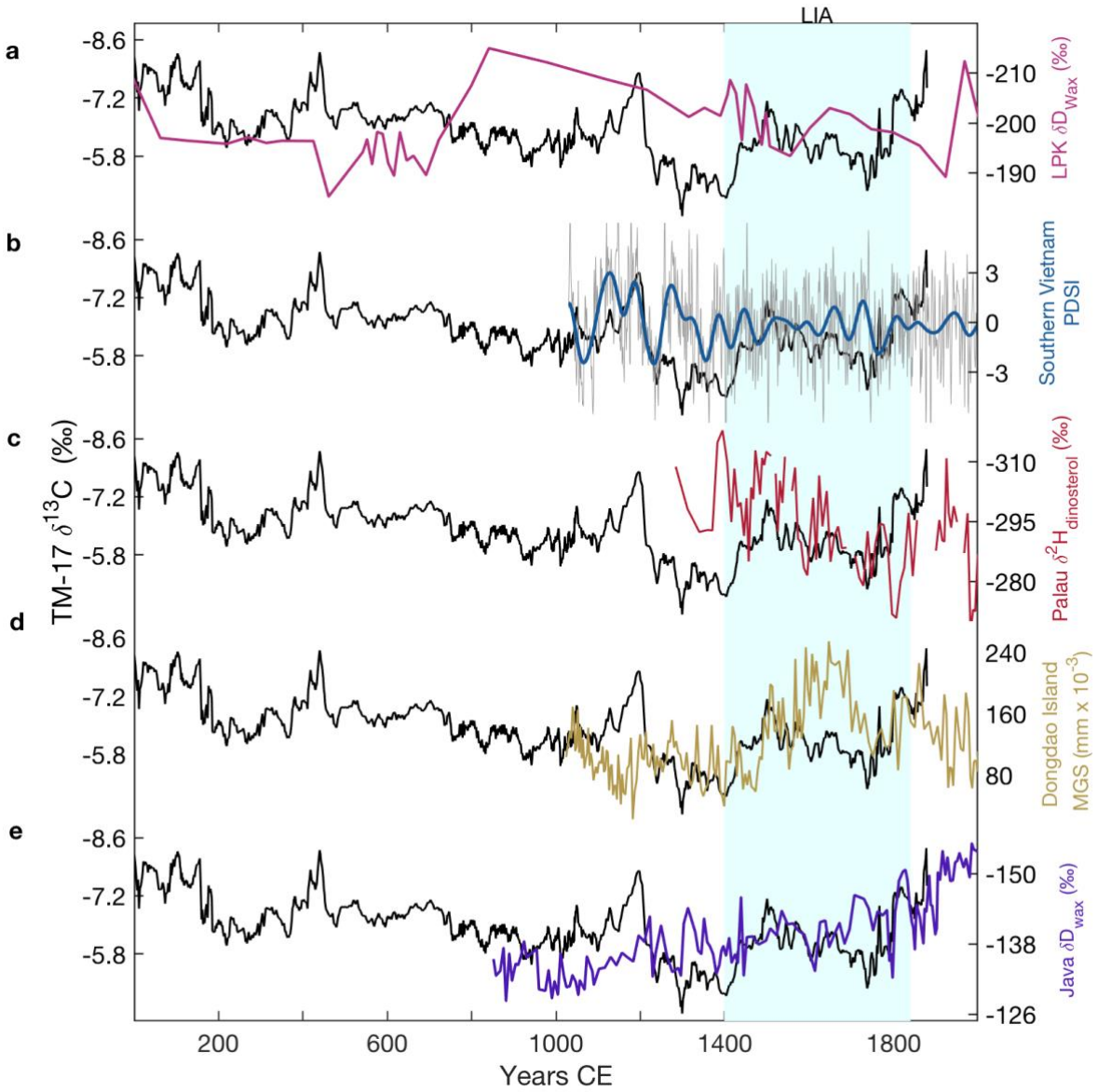

Figure A.3. Comparison of the TM-17 $\delta_{13}C$ record with regional proxy records. The black line in all panels shows the stalagmite TM-17 $\delta_{13}C$ record compared with (a) Leaf wax (δD_{wax}) from Lake Pa Kho (LPK), Thailand (Chawchai et al. 2015; Yamoah et al. 2016a). (b) Tree ring reconstructed Palmer Drought Severity Index (PDSI) from Bidoup Nui Ba National Park (BDNP), Vietnam (Buckley et al. 2010). The grey line represents the raw PDSI and the blue line is the 15-year Butterworth filtered data. (c) Dinosterol δ_2H from Clear Lake, Palau (Richey and Sachs 2016). (d) Mean grain size (MGS) from Cattle Pond, Dongdao Island, South China Sea (Yan et al. 2011). (e) Leaf wax δD from Lake Lading, East Java, western Indonesia ((Konecky et al. 2013). The y-axes in all panels are oriented such that wetter conditions/stronger convection is oriented up. Blue shaded bar corresponds to the timing of the Little Ice Age (LIA; 1400-1850).

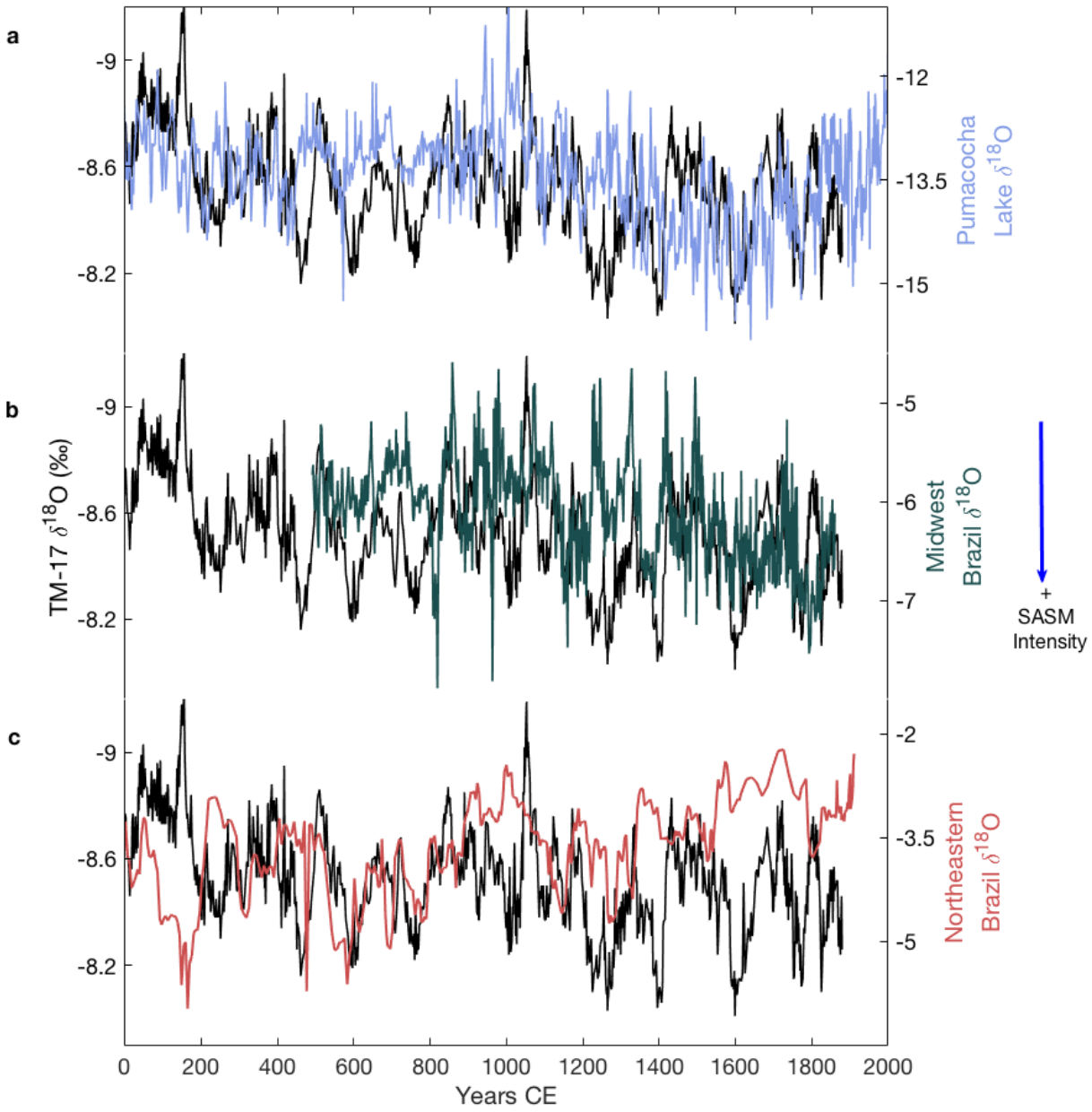

Figure A.4. Comparison of the TM-17 record with South American Monsoon proxy records. The black line in all panels shows the stalagmite TM-17 $\delta_{18}O$ record compared with (a) Pumacocha Lake $\delta_{18}O$ (Bird et al. 2011). (b) Stalagmite $\delta_{18}O$ from Curupira Cave, Brazil (Novello et al. 2016). (c) Stalagmite $\delta_{18}O$ from Diva de Maura Cave, Brazil (Novello et al. 2012). The y-axes in all panels are oriented such that weaker monsoon intensity recorded at TM Cave and stronger South American summer monsoon intensity is down.

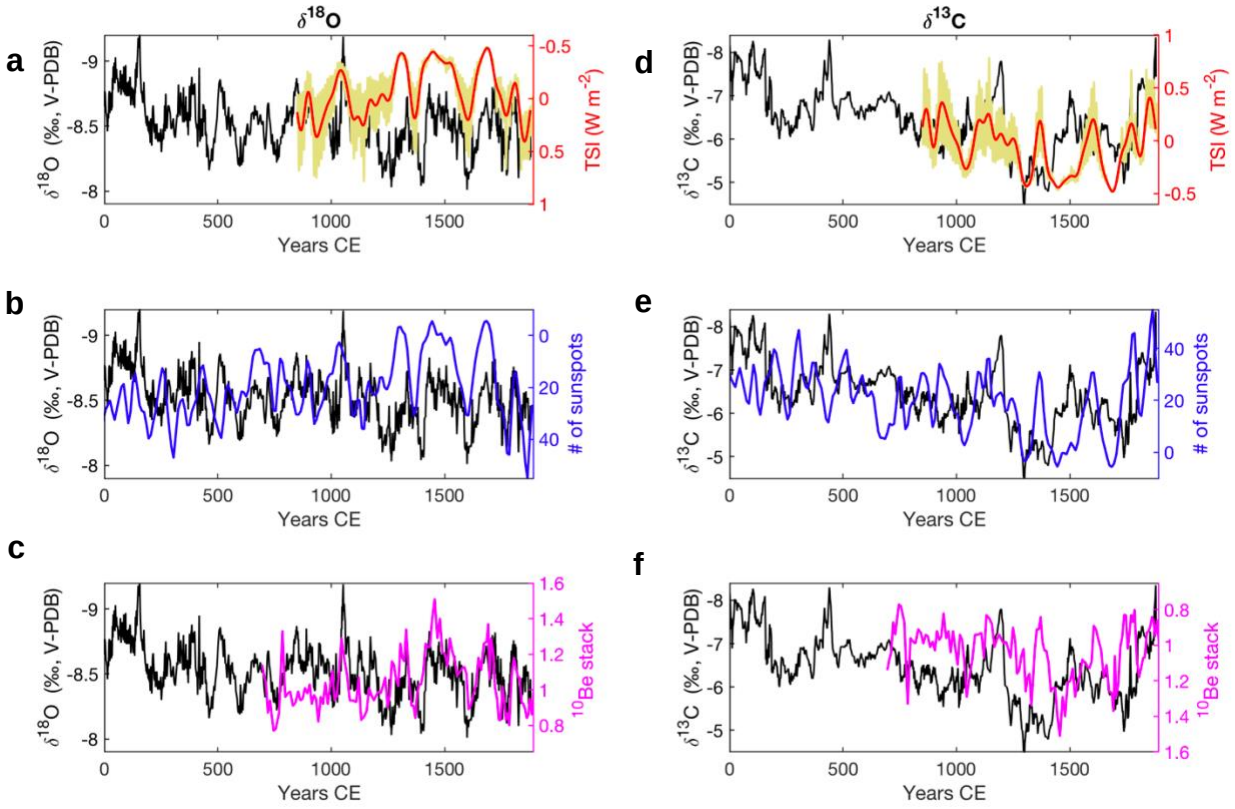

Figure A.5. Comparison of TM-17 $\delta_{18}O$ and solar activity proxies. (a-c) show the $\delta_{18}O$ record and (d-f) show the $\delta_{13}C$ record in black compared with records of (a) raw total solar irradiance reconstruction (Vieira et al. 2011) in yellow and 50-year low pass filtered time series in red, (b) reconstruction of the sunspot number based on $_{14}C$ concentrations (Solanki et al. 2004) in blue and (c) $_{10}Be$ stack derived from Central Antarctica ice cores in pink (Delaygue and Bard 2011). The y-axes in (a-c) are oriented such that weaker monsoon intensity and increased solar activity are down. The y-axes in (d-f) are oriented such that drier conditions and decreased solar activity are down.

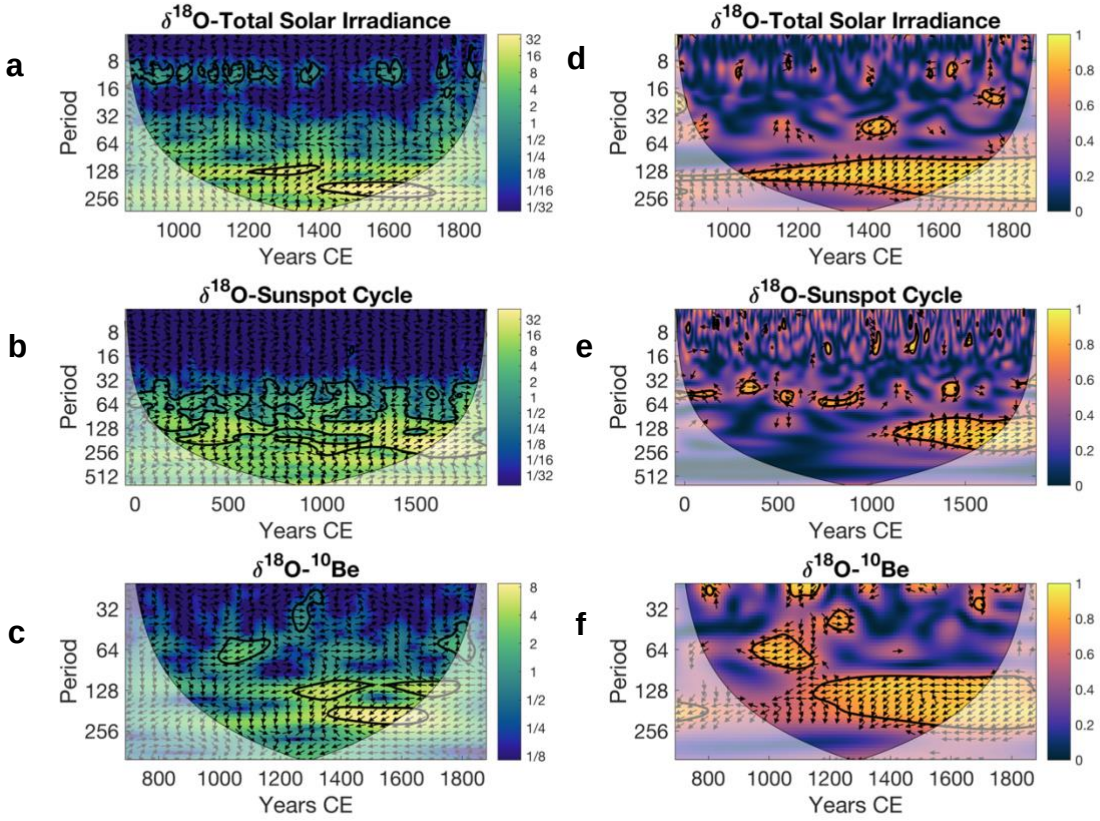

Figure A.6. Cross-wavelet and Wavelet Coherence analyses between TM-17 $\delta_{18}O$ with solar activity proxies. (a,d) Reconstructed Total Solar Irradiance reconstruction (Vieira et al. 2011). (b,e) Reconstruction of the sunspot number based on $_{14}C$ concentrations (Solanki et al. 2004). (e,f) $_{10}Be$ stack derived from Central Antarctica ice cores (Delaygue and Bard 2011). For clarity, (a-c) are the cross-wavelet analyses and (e-f) are the wavelet coherence analyses. The cross-wavelet measures the high common power in time-frequency space and the wavelet coherence measures the linear correlation between two time series at a given frequency (Grinsted et al. 2004). In all of the panels, the black outlines represent significance at 95% confidence interval against a red noise backgrounds using Monte Carlo methods. Right-facing arrows represent relative in-phase between the time series. Arrows are pointing to the left (out of phase) in (c,f) given the inverse relationship between $_{10}Be$ and $\delta_{18}O$, but still reflects decreased solar activity corresponding to increased monsoon intensity. Thin black line and white shading represents the cone of influence. The results show significant cross-wavelet power and high coherency at the multidecadal-centennial timescales in all panels.

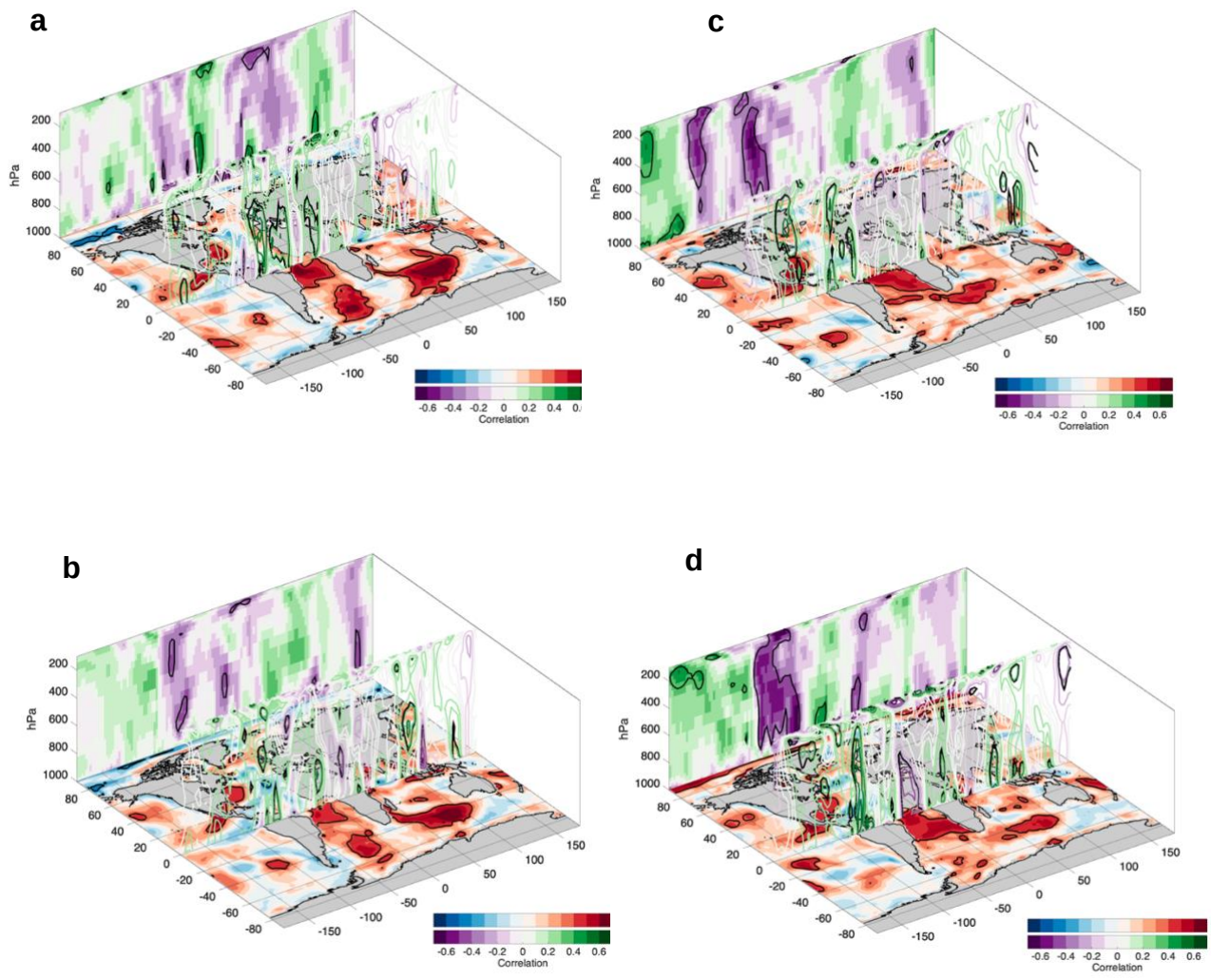

Figure A.7. As described in Figure. 4 except for each individual ensemble member in the CESM LME solar-only forcing. (a) Ensemble member 1 from CESM solar-only run. (b) Ensemble member 2 from solar-only run. (c) Ensemble member 3 from solar-only run. (d) Ensemble member 4 from solar-only run.

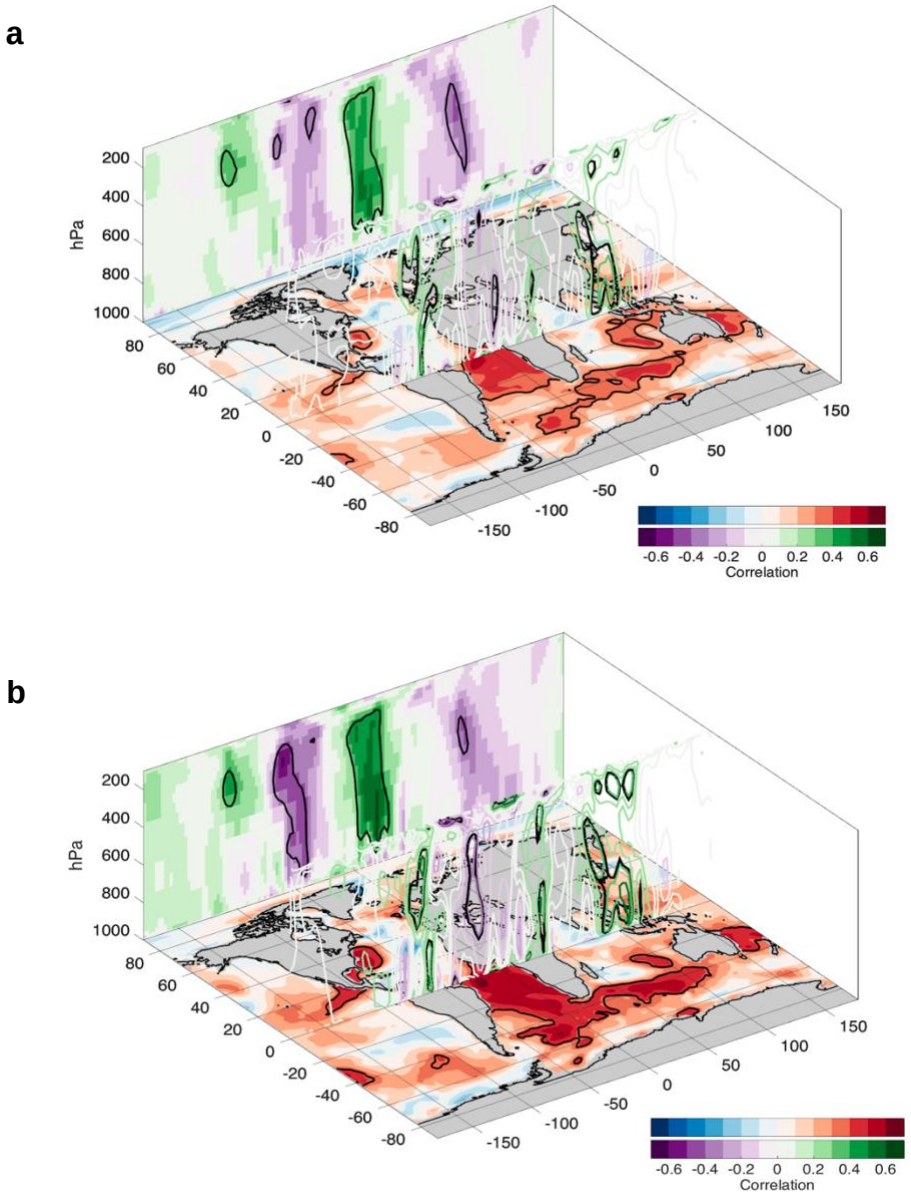

Figure A.8. As described in Figure. 4. (a) Solar-only forcing ensemble mean from 850-1878 CE. (b) Solar-only forcing ensemble mean from 1200-1878 CE.

Table A.1. U-Th concentrations, isotope ratios, and calculated ages for TM-17. Uncertainties are 2σ. Half-lives are those of Cheng et al. (2013). All ages are relative to 1950 CE. Corrected ages assume the initial $^{230}Th/^{232}Th$ atomic ratio of 4.4 ±2.2 x 10^{-6}, in secular equilibrium with the bulk Earth $^{232}Th/^{238}U$ value of 3.8. The activity ratios are indicated by parentheses. TM-17 U3 was excluded from the age model due to a large uncertainty.

Sample I.D	Depth from top (cm)	^{238}U (ppm)	^{232}Th (ppb)	$(^{230}Th/^{232}Th)$	$(^{230}Th/^{238}U)$	$(^{234}U/^{238}U)_{initial}$	Uncorr. age (yrs BP)	Corr. age (yrs BP)
TM-17 U1	0.3	2.22	2.05	16.0 ± 0.4	0.0048 ± 0.0001	1.6849 ± 0.0065	249 ± 7	229 ± 19
TM-17 U27	0.9	1.88	0.92	55.2 ± 1.4	0.0089 ± 0.0002	1.6810 ± 0.0050	511 ± 13	501 ± 16
TM-17 U28	1.3	2.10	0.81	90.9 ± 1.9	0.0116 ± 0.0002	1.6600 ± 0.0052	691 ± 14	682 ± 16
TM-17 U29	1.8	1.95	1.17	84.9 ± 1.2	0.0167 ± 0.0002	1.6660 ± 0.0052	1034 ± 13	1020 ± 18
TM-17 U3	2.7	2.09	0.33	469.3 ± 29.3	0.0245 ± 0.0007	1.6550 ± 0.0053	1563 ± 46	1560 ± 47
TM-17 U30	3.3	2.89	0.27	880.9 ± 26.2	0.0274 ± 0.0002	1.6700 ± 0.0051	1742 ± 13	1739 ± 13
TM-17 U31	3.8	3.12	0.63	460.3 ± 5.4	0.0303 ± 0.0002	1.6700 ± 0.0051	1932 ± 11	1927 ± 12

Uncertainties are 2σ. Half lives are those of Cheng et al., 2013. All ages are relative to 1950. Corrected ages assume the initial $^{230}Th/^{232}Th$ atomic ratio of 4.4 ±2.2 x 10^{-6}, in secular equilibrium with the bulk Earth $^{232}Th/^{238}U$ value of 3.8. The activity ratios are indicated by the round brackets. TM-17 U3 was excluded from the age model due to a large uncertaintity.

Table A.2. Correlation coefficients reported between TM-17 $\delta^{18}O$ and solar activity proxies: Total Solar Irradiance (TSI) (Vieira et al. 2011), sunspot number (Solanki et al. 2004), and ^{10}Be stack (Delaygue and Bard 2011). The Pearson *r* values are shown for both unfiltered (raw) and 50 year low-pass filtered data for two separate time periods: 850-1878 CE and 1200-1878 CE. The bolded coefficients are significant at 95% confidence level or greater. The numbers in the parenthesis represent the p-value calculated using the method of Macias-Fauria et al. (2012)[1].

		850-1878 CE	1200-1878 CE
TSI	Raw	0.16 (0.31)	**0.42 (0.01)**
	50-year lowpass filter	0.21 (0.37)	**0.54 (0.01)**
Sunspot Number	Raw	0.23 (0.27)	**0.48 (0.05)**
	50-year lowpass filter	0.24 (.029)	**0.52 (0.05)**
^{10}Be	Raw	-0.31 (0.12)	**-0.55 (< 0.01)**
	50-year lowpass filter	-0.33 (0.14)	**-0.60 (< 0.01)**

[1] Reported correlation coefficients are Pearson's *r* values, unless otherwise noted. Significance testing was conducted using a combination of 1,000 Monte Carlo iterations and time-series modelling in the frequency domain to consider the effect of serial correlation (Macias-Fauria et al., 2012).

Appendix B

Cave Monitoring Data for Tham Doun Mai Cave

Table B.1. Tham Doun Mai (TM Cave) cave drip water monitoring data from 2010-2017. Data has been filtered to remove samples that show signs of evaporation.

Sample ID	Sample Date	δD (‰ VSMOW)	$\delta_{18}O$ (‰ VSMOW)	Drip rate (per min)	Notes
D2	12/9/10	-52.1	-8.15		multiple slow drips
D3	12/9/10	-50.9	-7.90	4	
D4	12/9/10	-45.8	-7.45		multiple slow drips
D5	12/9/10	-44.8	-7.15	5	near D4 and stal TM6 (pool)
D6	12/9/10	-49.1	-8.15		multiple slow drips
D7	12/9/10	-52.8	-8.16	3	
D8	12/9/10	-53.4	-8.29		
D1 (SAI)	1/3/11	-57.8	-8.6	12	collected by Mr. Sai
D2 (SAI)	1/3/11	-56.8	-8.5		collected by Mr. Sai
D1 (SAI)	2/2/11	-55.8	-8.5	9	collected by Mr. Sai
D2 (SAI)	2/2/11	-59.3	-8.5		collected by Mr. Sai
D1 (SAI)	3/4/11	-54.7	-7.9	7	collected by Mr. Sai
D2 (SAI)	3/4/11	-57.8	-8.3		collected by Mr. Sai
D1 (SAI)	4/2/11	-57.8	-8.4	6	collected by Mr. Sai
D2 (SAI)	4/2/11	-59.7	-8.7		collected by Mr. Sai
D1 (SAI)	5/2/11	-57.0	-8.6	6	collected by Mr. Sai
D2 (SAI)	5/2/11	-58.6	-8.6		collected by Mr. Sai
D1 (SAI)	6/3/11	-54.3	-8.0	8	collected by Mr. Sai
D2 (SAI)	6/3/11	-59.1	-8.8		collected by Mr. Sai
D1 (SAI)	7/2/11	-58.1	-8.6	7	collected by Mr. Sai
D2 (SAI)	7/2/11	-60.1	-8.6		collected by Mr. Sai
D1 (SAI)	8/4/11	-55.7	-8.1	10	collected by Mr. Sai
D2 (SAI)	8/4/11	-56.0	-8.2		collected by Mr. Sai
D1 (SAI)	9/3/11	-57.4	-8.6	12	collected by Mr. Sai
D2 (SAI)	9/3/11	-60.3	-8.5		collected by Mr. Sai
D1 (SAI)	10/2/11	-54.5	-8.2	20	collected by Mr. Sai
D2 (SAI)	10/2/11	-59.5	-8.6		collected by Mr. Sai
D1 (SAI)	11/4/11	-58.3	-8.7	20	collected by Mr. Sai

D2 (SAI)	11/4/11	-59.8	-8.5		collected by Mr. Sai
D1 (SAI)	12/3/11	-57.6	-8.5	15	collected by Mr. Sai
D2 (SAI)	12/3/11	-59.9	-8.6		collected by Mr. Sai
D6-7	1/15/13	-51.6	-7.9		Mix from 2010 sites, isotopes and TM
D1-3a	1/15/13	-42.2	-6.6		Mix from 2010 sites, isotopes only
D1-3b	1/15/13	-54.3	-8.2	2	from near stalagmite, isotopes only (picture?)
D1-3c	1/15/13	-53.1	-8.0	3	from near D1-3b (picture); isotopes and TM
D1-3d	1/15/13	-47.4	-7.3	3	Isotopes and TM; same for mix one D1-3a?)
D10a	1/16/13	-54.8	-8.3	>100	Lg. stal; 3 L Th sample; small for isotopes and TM
D10b	1/16/13	-54.6	-8.0	60	14C/microbe, isotopes & TM. Also on lg. stal. Next to D10c?
TM-DripBottomMix_1	2/27/15	-55.8	-8.1		multiple slow drips
TM-DripBottomMix_2	2/27/15	-43.5	-6.7		multiple slow drips
TM-DI-3	2/26/15	-44.6	-7.5		multiple slow drips
TM-DI-3b	2/26/15	-42.4	-6.1		multiple slow drips
TM-DI-3c	2/26/15	-57.1	-8.0	3	
TM-D6-7a	2/27/15	-48.3	-7.6		multiple slow drips
TM-D6-7b	2/27/15	-57.9	-8.2		multiple slow drips
TM-D10	2/27/15	-54.9	-8.0	60	
TM-D10_fast	2/28/15	-56.5	-8.1		steady stream
TM-D4	2/26/15	-53.8	-8.1	2	
TM-D4b	2/28/15	-47.3	-7.2		multiple slow drips
TM-D1a	2/20/17	-51.0	-7.7		multiple slow drips
TM-D1b	2/20/17	-53.2	-8.1		multiple slow drips
TM-D1-3a	2/20/17	-47.9	-7.2		multiple slow drips
TM-D4a	2/20/17	-54.4	-8.1		multiple slow drips
TM-D4d	2/20/17	-54.9	-8.1	4	single drip - Andrea's hole
TM-D4e	2/20/17	-51.6	-7.9		multiple slow drips
TM-D6-7	2/20/17	-51.4	-7.8		multiple slow drips
TM-D6-7b	2/20/17	-48.7	-7.4		multiple slow drips

TM-D10a	2/20/17	-58.6	-8.6		faster D10 drip - steady stream
TM-D10b	2/20/17	-55.7	-8.3		slower fast drip
		-53.94	**-8.05**		
		4.83	**0.56**		

Table B.2. TM Cave Ca^{2+} monitoring data from 2013, 2015, and 2017. Estimates are based on inductively-coupled mass spectrometry counts per second: normalized to standard (during run) and multiplied by standard concentrations.

Year	**Sample**	**[Ca] ppb**	**[Ca] ppm**
2013	TM-P1-3a	67,240	67.2
2013	TM-P1-3b	46,211	46.2
2013	TM-D1-3c	25,179	25.2
2013	TM-D1-3d	30,763	30.8
2013	TM-D6-7	29,406	29.4
2013	TM-D10a	29,231	29.2
2013	TM-D10b	29,649	29.6
2013	TM-P1-3b-DUP	43,884	43.9
2015	TM-2015-D1-3c	22,987	23
2015	TM-2015-D4-i	29,562	29.6
2015	TM-2015-D4-ii	31,404	31.4
2015	TM-2015-D4b	28,703	28.7
2015	TM-2015-D6-7	30,742	30.7
2015	TM-2015-D10-i	35,557	35.6
2015	TM-2015-D10-ii	30,372	30.4
2015	TM-2015-D10-iii	49,832	49.8
2015	TM-2015-DripBot	29,293	29.3
2015	TM-2015-Steam	32,515	32.5
2017	TM17-1-3a	41,466	41.5
2017	TM17-D4a	60,202	60.2
2017	TM17-D4d	51,407	51.4
2017	TM17-D4e	38,974	39
2017	TM17-D6-7	52,906	52.9
2017	TM17-D10a	47,493	47.5
2017	TM17-D10b	37,658	37.7
2017	TM17-D17	44,088	44.1
2017	TM17-D17-DUPd50	39,004	39

2017	TM17-River	49,318	49.3

Table B.3. TM Cave monitoring data from 2010-2017. Bolded results represent averaged values collected from further back in the cave (Drip sites>D5).

Date (s)	Location	pH	Alk. (ppm)	Water Temp. (°C)	Air Temp (°C)	RH (%)	pCO_2 (ppm)	Notes
12/9/10	D3	8.33	260	20.6				
12/9/10	D7	7.47	280	21.4				
1/15/13	D2				19.92	95	500	close to entrance, just after crawl
1/15/13	D10	8.27	96	22.8	22		580	
2/25/15	D6-D7				20.5	95.4	630	CO2 from Vaisala (new, better probe)
2/25/15	D6-D7						630	CO2 from LiCOR
2/25/15	D3				20.1	93.8		
2/27/15	D10	8.34	156	22.2				
2/27/15	D10	8.37		22				
2/20/17	D1				19.6	92.9		
2/20/17	D10	8.2	179		22	93		Alk. Is average, s.d. 9, n=4
2/20/17	cave stream	8.4	144	21.4				
	average	8.2	185.8	21.7	20.7	94	585	
	sd	0.3	70.9	0.8	1.1	1.1	61.4	
>D5	**average**	**8.295**	**192**	**22.1**	**21.5**	**94.2**	**613.3**	
	sd	**0.1**	**44.6**	**0.6**	**0.9**	**1.7**	**28.9**	

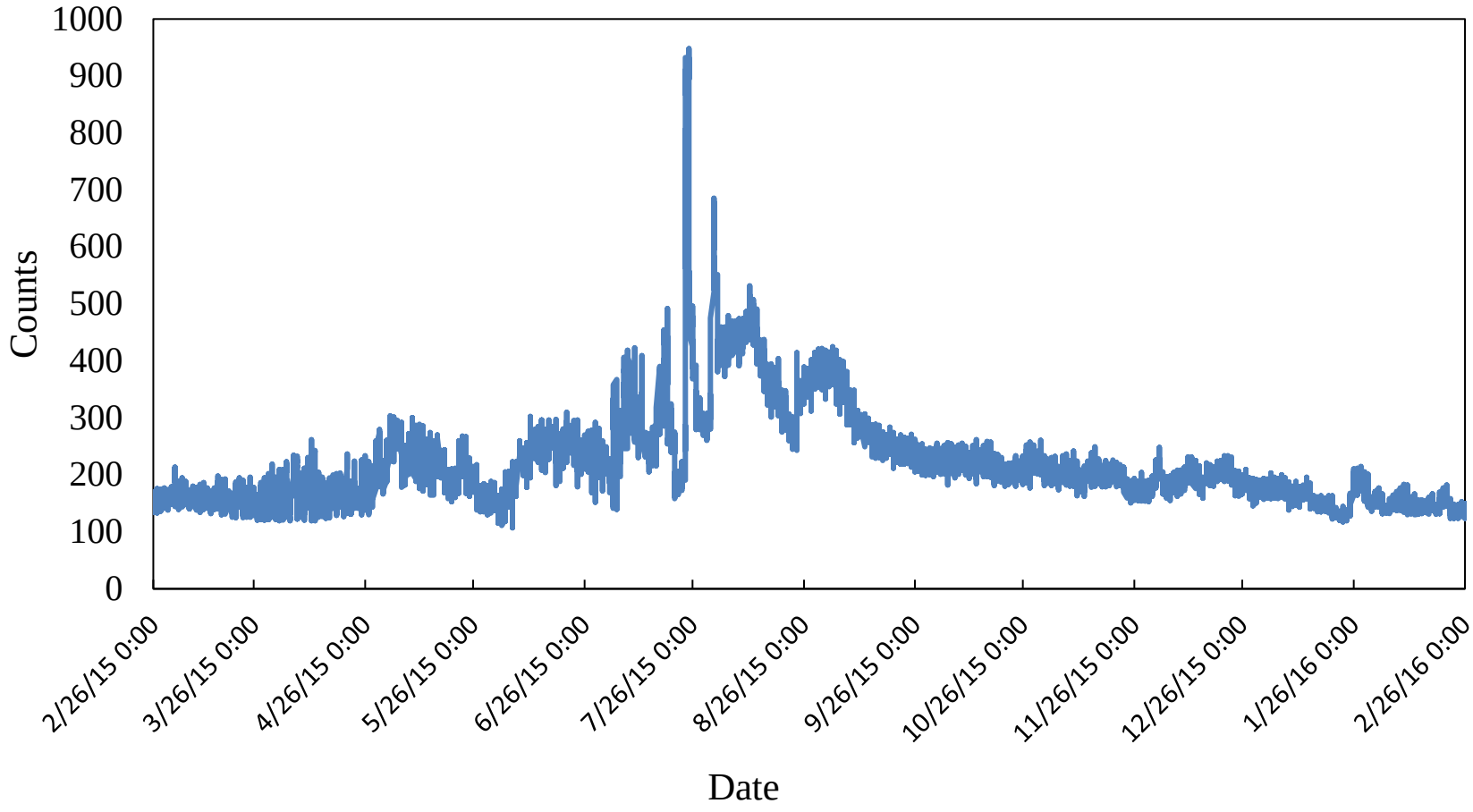

Figure B.1. Drip water counts recorded by a Driptych drip logger placed near the balcony on which Stalagmite TM-17 was collected. Data shown is from /25/2015 to 2/26/2016. The annual average was ~224 counts/hour or ~3.7 counts/minute. Note the clear seasonal variability, in which the rapid increase around July is coincident with rainy season and followed by exponential decay.

Appendix C

Preliminary Stalagmite TM-19 Age Model and Stable Isotope Record

The following material is preliminary work and data that was completed during my tenure as a graduate student. Stalagmite TM-19 was collected in 2013 from Tham Doun Mai Cave in the same field work expedition during which TM-17 was collected. Low-resolution sampling for stable isotope analyses were completed in 2015 (Table C.1) and the U-Th dates were obtained in 2013 and 2015 through collaborations at the University of Oxford, UK (Table C.2). Much of the imprecision in the ages obtained in 2013 were initially attributed to relatively large ^{230}Th blank correction. However, additional analyses conducted in 2015 at the same depths found that these samples appear to have high initial thorium, which can be corrected with a reasonable ^{230}Th/^{232}Th ratio. Through tweaking of the initial Th correction, it was confirmed that it is entirely possible that stalagmite TM-19 was actively growing when collected in 2013. The initial ^{230}Th/^{232}Th ratio required to support this is similar to the initial ratio measured in a modern glass plate calcite from TM Cave. After establishing upper and lower limits of initial ^{230}Th/^{232}Th to ensure the ages laid in proper stratigraphic order, the ages were calculated with more appropriate uncertainties from the initial Th correction. The youngest sample (TM-19_U2-D) is considered “out of range”, since it is indistinguishable from the future based on realistic error limits (Table C.1).

It is important to note that due to the large uncertainty on the initial Th value, the upper 3 ages suggest they are not very useful for constraining the age model. Given these complications with the U-Th age, future work should involve building the TM-19 age model off of layer counting and further constrain the laminae counting age model with the U-series age model.

Similar to stalagmite TM-17, synchrotron images were completed for TM-19 through collaborations with the University of Newcastle, NSW, that show clear Sr annual laminae throughout. Sr laminations are noted to be much clearer compared to TM-17, which points to lower porosity and higher growth rate of TM-19. Preliminary work by Andrea Borsato was completed for the topmost 51 mm. TM-19 exhibits annual cycles in Sr, but in other areas the signal is blurred. Preliminary fast automated laminae counting for the entire section was done but revealed about 450 less years than the revised age model based on the U-Th ages. It is possible there may be a slight mismatch of the depths from top, since two different pieces of the stalagmite were used for the synchrotron scans and the U-Th ages. Some parts of the synchrotron maps have strong high-Sr bands, which may be representative of condensed intervals and/or short hiatuses. Dry periods associated with possible interruptions of the drip rate correspond with anomalously high Sr concentrations. Thus, it is possible that the automated counting is missing several years to decades for every episode and account for the missing laminae numbers in the count. Additional laminae counting through manual visual approaches are necessary to create a more robust laminae counting age model that aligns with the U-Th ages. Finally, micromilled power for radiocarbon analyses to test for the ^{14}C may further constrain the TM-19 age model.

Table C.1. U-Th concentrations, isotope ratios, and calculated ages for TM-19. Uncertainties are 2σ. Half-lives are those of Cheng et al. (2013). All ages are relative to 1950 CE. Corrected ages assume the initial $_{230}Th/_{232}Th$ atomic ratio of 2.5 ±4.7 x 10_{-6}. The activity ratios are indicated by parentheses. TM-19 U2-D age is not resolvable from future.

Stal.	Depth from top (cm)	^{238}U (ppm)	^{232}Th (ppb)	$(^{230}Th/^{232}Th)$	$(^{230}Th/^{238}U)$	$(^{234}U/^{238}U)_{initial}$	Raw Age (yrs BP)	Corr. Age (yrs BP)
TM-19_U2-D	0.75	0.27	4.56	5.5 ± 0.5	0.0299 ± 0.0026		1812 ± 168	
TM-19_U3-D	2.05	0.27	4.82	5.7 ± 0.3	0.0330 ± 0.0018	1.7139 ± 0.0098	2056 ± 120	541 ± 529
TM-19_U4-D	3.2	0.28	3.71	8.0 ± 0.6	0.0350 ± 0.0024	1.7371 ± 0.0103	2153 ± 153	1017 ± 418
TM-19_U5-D	4.45	0.38	0.29	102.9 ± 11.9	0.0261 ± 0.0019	1.9000 ± 0.0100	1448 ± 111	1389 ± 111
TM-19_U6-D	5.5	0.35	0.08	430.1 ± 138.3	0.0308 ± 0.0017	1.8932 ± 0.0099	1728 ± 99	1711 ± 96
TM-19_U1	6.75	0.46	0.75	64.8 ± 4.0	20.6957 ± 0.0009	1.8921 ± 0.0073	1958 ± 54	1832 ± 71

*Uncertainties are 2σ. Half lives are those of Cheng et al., 2013. All ages are relative to 1950. Corrected ages assume the initial $^{230}Th/^{232}Th$ atomic ratio of 2.5 ±4.7 x 10^{-6}.

Table C.2. Summary of TM-19 stable isotope measurements.

Sample Name	Depth(mm)	$\delta_{13}C$ (‰)	$\delta_{18}O$ (‰)
TM19B-1	0	-12.25	-9.18
TM19B-2	0.25	-12.3	-9.14
TM19B-3	0.5	-12.03	-9.45
TM19B-4	0.75	-11.96	-9.33
TM19B-5	1	-11.94	-9.33
TM19B-6	1.25	-11.87	-9.18
TM19B-7	1.5	-11.39	-9.11
TM19B-8	1.75	-11.81	-8.8
TM19B-9	2	-11.86	-8.83
TM19B-10	2.25	-11.7	-9.15
TM19B-11	2.5	-11.22	-9.37
TM19B-12	2.75	-11.09	-9.24
TM19B-13	3	-11.41	-9.35
TM19B-14	3.25	-11.76	-9.48
TM19B-15	3.5	-12.01	-9.51
TM19B-16	3.75	-11.96	-9.41
TM19B-17	4	-12	-9.5
TM19B-18	4.25	-11.98	-9.3
TM19B-19	4.5	-11.67	-9.23
TM19B-20	4.75	-11.64	-8.96

TM19B-21	5	-11.39	-8.97
TM19B-22	5.25	-10.92	-8.87
TM19B-23	5.5	-11.18	-9.25
TM19B-24	5.75	-11.08	-9.23
TM19B-25	6	-11.43	-9.38
TM19B-26	6.25	-11.69	-9.15
TM19B-27	6.5	-11.78	-9.19
TM19B-28	6.75	-11.7	-9.11
TM19B-29	7	-11.55	-9.11
TM19B-30	7.25	-11.48	-9.2
TM19B-31	7.5	-11.38	-9.27
TM19B-32	7.75	-11.79	-9.37
TM19B-33	8	-11.4	-9.31
TM19B-34	8.25	-11.46	-9.06
TM19B-35	8.5	-11.58	-9.24
TM19B-36	8.75	-11.54	-9.22
TM19B-37	9	-11.38	-9.42
TM19B-38	9.25	-11.64	-9.43
TM19B-39	9.5	-11.69	-9.51
TM19B-40	9.75	-11.07	-9.49
TM19B-41	10	-11.15	-9.63
TM19B-42	10.25	-10.75	-9.23
TM19B-43	10.5	-10.76	-9.53
TM19B-44	10.75	-11.22	-9.63
TM19B-45	11	-12.46	-10.07
TM19B-46	11.25	-11.85	-9.79
TM19B-47	11.5	-11.88	-9.7
TM19B-48	11.75	-10.92	-9.43
TM19B-49	12	-10.66	-9.43
TM19B-50	12.25	-10.73	-8.87
TM19B-51	12.5	-11.09	-8.93
TM19B-52	12.75	-11.71	-9.03
TM19B-53	13	-11.32	-9.05
TM19B-54	13.25	-11.52	-9
TM19B-56	13.75	-11.07	-8.86
TM19B-58	14.25	-10.98	-8.97

TM19B-59	14.5	-11.3	-9.44
TM19B-60	14.75	-11.22	-9.28
TM19B-61	15	-11.62	-9.23
TM19B-62	15.25	-11.5	-9.33
TM19B-63	15.5	-11.52	-9.34
TM19B-64	15.75	-10.91	-9.1
TM19B-65	16	-10.61	-9.04
TM19B-66	16.25	-10.94	-9.34
TM19B-67	16.5	-11.71	-9.58
TM19B-68	16.75	-11.95	-9.36
TM19B-69	17	-10.61	-9.16
TM19B-70	17.25	-10.32	-9.05
TM19B-71	17.5	-10.39	-9.15
TM19B-72	17.75	-10.52	-9.25
TM19B-74	18.25	-10.69	-9.55
TM19B-75	18.5	-10.77	-9.23
TM19B-76	18.75	-10.74	-9.25
TM19B-78	19.25	-10.75	-9.41
TM19B-79	19.5	-10.92	-9.59
TM19B-80	19.75	-11.05	-9.64
TM19B-81	20	-11.15	-9.44
TM19B-82	20.25	-11.02	-9.29
TM19B-84	20.75	-10.71	-9.36
TM19B-85	21	-10.84	-9.39
TM19B-86	21.25	-10.93	-9.6
TM19B-87	21.5	-10.66	-9.54
TM19B-88	21.75	-10.29	-9.52
TM19B-89	22	-10.15	-9.36
TM19B-90	22.25	-9.74	-9.02
TM19B-91	22.5	-10.07	-9.08
TM19B-92	22.75	-10.25	-9.27
TM19B-93	23	-10.26	-9.43
TM19B-94	23.25	-10.18	-9.27
TM19B-95	23.5	-10.26	-9.23
TM19B-96	23.75	-10.4	-9.4
TM19B-98	24.25	-10.68	-9.23

TM19B-99	24.5	-11.01	-9.31
TM19B-100	24.75	-10.77	-9.11
TM19B-101	25	-10.8	-8.98
TM19B-102	25.25	-10.8	-8.89
TM19B-103	25.5	-10.91	-9.11
TM19B-104	25.75	-10.62	-9.3
TM19B-105	26	-10.62	-9.4
TM19B-106	26.25	-10.9	-9.23
TM19B-107	26.5	-10.82	-9.05
TM19B-108	26.75	-10.81	-9.11
TM19B-109	27	-11.09	-9.06
TM19B-110	27.25	-11.31	-9.08
TM19B-111	27.5	-11.49	-9.25
TM19B-112	27.75	-11.4	-9.53
TM19B-113	28	-11.19	-9.48
TM19B-114	28.25	-10.74	-9.34
TM19B-115	28.5	-10.45	-9.23
TM19B-116	28.75	-10.21	-9.16
TM19B-117	29	-10.11	-9.24
TM19B-118	29.25	-10.75	-9.51
TM19B-119	29.5	-10.04	-9.35
TM19B-120	29.75	-9.78	-8.96
TM19B-121	30	-9.67	-8.74
TM19B-122	30.25	-9.75	-8.99
TM19B-123	30.5	-10.07	-9.36
TM19B-124	30.75	-10.74	-9.71
TM19B-125	31	-10.92	-9.77
TM19B-126	31.25	-10.6	-9.9
TM19B-127	31.5	-10.7	-9.89
TM19B-128	31.75	-10.65	-9.42
TM19B-129	32	-10.66	-9.06
TM19B-130	32.25	-11.13	-9.24
TM19B-131	32.5	-10.87	-9.18
TM19B-132	32.75	-10.57	-9.21
TM19B-133	33	-10.44	-9.1
TM19B-134	33.25	-10.82	-9.23

TM19B-135	33.5	-11.21	-9.61
TM19B-136	33.75	-10.98	-9.49
TM19B-137	34	-10.81	-9.47
TM19B-138	34.25	-11.09	-9.58
TM19B-139	34.5	-11.23	-9.52
TM19B-140	34.75	-11.67	-9.44
TM19B-141	35	-11.55	-9.59
TM19B-142	35.25	-11.07	-9.21
TM19B-144	35.75	-10.95	-9.21
TM19B-145	36	-10.55	-9.26
TM19B-146	36.25	-10.74	-9.27
TM19B-147	36.5	-10.61	-9.29
TM19B-148	36.75	-10.79	-9.78
TM19B-149	37	-11.37	-10.02
TM19B-150	37.25	-11.01	-9.99
TM19B-151	37.5	-11.19	-10.15
TM19B-152	37.75	-11.1	-9.66
TM19B-153	38	-11.16	-9.52
TM19B-154	38.25	-10.76	-9.3
TM19B-155	38.5	-11.02	-9.49
TM19B-156	38.75	-10.51	-9.28
TM19B-157	39	-10.7	-9.39
TM19B-158	39.25	-11.35	-9.44
TM19B-159	39.5	-10.52	-9.16
TM19B-160	39.75	-9.35	-8.98
TM19B-161	40	-10.15	-9.15
TM19B-162	40.25	-10.9	-9.35
TM19B-163	40.5	-10.56	-9.3
TM19B-164	40.75	-10.13	-9.31
TM19B-165	41	-9.82	-8.88
TM19B-166	41.25	-10.29	-9.05
TM19B-167	41.5	-10.28	-8.9
TM19B-168	41.75	-11.04	-8.93
TM19B-169	42	-10.5	-8.98
TM19B-170	42.25	-10.97	-9.16
TM19B-171	42.5	-11.46	-9.39

TM19B-172	42.75	-11.64	-9.4
TM19B-173	43	-11.17	-8.84
TM19B-174	43.25	-11.52	-9.2
TM19B-175	43.5	-11.44	-9.27
TM19B-176	43.75	-10.68	-8.97
TM19B-177	44	-10.61	-8.69
TM19B-178	44.25	-11.07	-9.08
TM19B-179	44.5	-11.33	-9.2
TM19B-180	44.75	-11.01	-9.28
TM19B-181	45	-11.48	-9.38
TM19B-182	45.25	-12.16	-9.55
TM19B-183	45.5	-12.49	-9.84
TM19B-184	45.75	-12.39	-9.59
TM19B-185	46	-11.39	-9.22
TM19B-186	46.25	-11.85	-9.11
TM19B-187	46.5	-11.74	-9.19
TM19B-188	46.75	-11.69	-9.27
TM19B-189	47	-11.18	-9.26
TM19B-190	47.25	-11.39	-9.43
TM19B-191	47.5	-11.33	-9.22
TM19B-192	47.75	-11.93	-9.55
TM19B-193	48	-12.03	-9.57
TM19B-194	48.25	-11.97	-9.56
TM19B-195	48.5	-11.73	-9.11
TM19B-196	48.75	-11.48	-9.18
TM19B-197	49	-11.68	-9.14
TM19B-198	49.25	-11.37	-9.15
TM19B-199	49.5	-10.97	-9.21
TM19B-200	49.75	-11.84	-9.76
TM19B-201	50	-10.85	-9.23
TM19B-202	50.25	-10.28	-9.13
TM19B-203	50.5	-10.25	-8.93
TM19B-204	50.75	-10.58	-9.21
TM19B-205	51	-10.31	-9.13
TM19B-206	51.25	-10.48	-8.99
TM19B-207	51.5	-10.06	-8.89

TM19B-208	51.75	-10.34	-9.07
TM19B-209	52	-10.17	-9.01
TM19B-210	52.25	-10.14	-9.1
TM19B-211	52.5	-10.04	-9.08
TM19B-212	52.75	-10.27	-9.3
TM19B-213	53	-10.26	-9.23
TM19B-214	53.25	-10.33	-9.38
TM19B-215	53.5	-10.4	-9.45
TM19B-216	53.75	-10.92	-9.86
TM19B-217	54	-10.54	-9.61
TM19B-218	54.25	-10.26	-9.4
TM19B-219	54.5	-10.25	-9.36
TM19B-220	54.75	-10.43	-9.23
TM19B-221	55	-10.1	-8.98
TM19B-222	55.25	-10.31	-9.16
TM19B-223	55.5	-10.08	-9.31
TM19B-224	55.75	-10.01	-9.43
TM19B-225	56	-10.01	-9.34
TM19B-226	56.25	-10.34	-9.53
TM19B-227	56.5	-10.72	-10.09
TM19B-228	56.75	-10.35	-9.31
TM19B-229	57	-10.04	-9.06
TM19B-230	57.25	-10.18	-9.17
TM19B-231	57.5	-10.37	-9.1
TM19B-232	57.75	-10.41	-9.11
TM19B-233	58	-10.06	-8.82
TM19B-234	58.25	-10.01	-8.94
TM19B-235	58.5	-10.03	-9.01
TM19B-236	58.75	-10.08	-8.93
TM19B-237	59	-9.87	-8.85
TM19B-238	59.25	-9.79	-9.14
TM19B-239	59.5	-9.44	-9.1
TM19B-240	59.75	-9.7	-8.87
TM19B-241	60	-9.78	-8.69
TM19B-242	60.25	-10.37	-8.84
TM19B-243	60.5	-10.17	-8.91

TM19B-244	60.75	-10.5	-9.1
TM19B-245	61	-10.74	-9.38
TM19B-246	61.25	-11.17	-9.5
TM19B-247	61.5	-10.84	-9.47
TM19B-248	61.75	-10.98	-9.18
TM19B-249	62	-11.32	-9.58
TM19B-250	62.25	-11.21	-9.3
TM19B-251	62.5	-11.2	-9.5
TM19B-252	62.75	-11.69	-9.54
TM19B-253	63	-11.2	-9.59
TM19B-254	63.25	-11.42	-9.46
TM19B-255	63.5	-11.13	-9.62
TM19B-256	63.75	-11.65	-9.76
TM19B-257	64	-11.37	-9.71
TM19B-258	64.25	-11.45	-9.69
TM19B-259	64.5	-11.53	-9.76
TM19B-260	64.75	-11.37	-9.72
TM19B-261	65	-11.41	-9.78
TM19B-262	65.25	-11.72	-9.83
TM19B-263	65.5	-11.31	-9.54
TM19B-264	65.75	-11.6	-9.65
TM19B-265	66	-11.44	-9.52
TM19B-266	66.25	-11.68	-9.52
TM19B-267	66.5	-11.4	-9.41
TM19B-268	66.75	-11.32	-9.46
TM19B-269	67	-11.53	-9.59
TM19B-270	67.25	-10.9	-9.43
TM19B-271	67.5	-11.22	-9.55
TM19B-272	67.75	-10.7	-9.45
TM19B-273	68	-11.33	-9.65
TM19B-274	68.25	-11.22	-9.56
TM19B-275	68.5	-11.35	-9.73
TM19B-276	68.75	-11.45	-9.71
TM19B-277	69	-11.21	-9.51
TM19B-278	69.25	-11.28	-9.58
TM19B-279	69.5	-11.24	-9.74

TM19B-280	69.75	-11.02	-9.6
TM19B-281	70	-10.8	-9.69
TM19B-282	70.25	-11.56	-9.81
TM19B-283	70.5	-12.11	-9.99
TM19B-284	70.75	-11.34	-9.44
TM19B-285	71	-11.7	-9.64
TM19B-286	71.25	-11.63	-9.71
TM19B-287	71.5	-11.69	-9.66
TM19B-288	71.75	-11.48	-9.46
TM19B-289	72	-11.86	-9.64
TM19B-290	72.25	-11.7	-9.62
TM19B-291	72.5	-11.68	-9.7
TM19B-292	72.75	-11.92	-9.63
TM19B-293	73	-11.72	-9.67
TM19B-294	73.25	-11.81	-9.84
TM19B-295	73.5	-11.45	-9.79
TM19B-296	73.75	-11.45	-9.71
TM19B-297	74	-11.26	-9.71
TM19B-298	74.25	-11.26	-9.71
TM19B-299	74.5	-11	-9.66
TM19B-300	74.75	-11.11	-9.69
TM19B-301	75	-11	-9.66
TM19B-302	75.25	-11.01	-9.76
TM19B-303	75.5	-10.76	-9.75
TM19B-304	75.75	-10.71	-9.69